8-2022

Crack Control and Bond Performance of Alternative Coated Reinforcements in Concrete

Sachin Sreedhara
ssreedh@clemson.edu

CRACK CONTROL AND BOND PERFORMANCE OF ALTERNATIVE COATED REINFORCEMENTS IN CONCRETE

A Dissertation
Presented to
the Graduate School of
Clemson University

In Partial Fulfillment
of the Requirements for the Degree
Doctor of Philosophy
Civil Engineering

---

by
Sachin Sreedhara
August 2022

Accepted by:
Dr. Brandon Ross, Committee Chair
Dr. Amir Poursaee, Committee Co-chair
Dr. Thomas Cousins
Dr. M Z Naser

ABSTRACT

Concrete cracking in structures is a ubiquitous problem which can lead to the deterioration of the structure. Other than affecting the strength aspect of a structure, cracking impacts the serviceability criteria as well. Although cracking phenomenon in any structure is highly inevitable, it has to be minimized in order to maintain a structure's life effectively. Cracking in reinforced concrete structures is related to the bond strength developed between the bar and the concrete. It also depends on an ability of the bar to resist the stresses due to shrinkage to minimize the crack. Another important aspect is the resistance offered by the reinforcement to minimize the residual crack width after withdrawal of high loads beyond or near the yielding capacity. All these parameters were considered and have been studied as a part of this dissertation through experimental testing.

The variables used in the tests are the alternative coated reinforcements like textured epoxy, hot dipped galvanized, and continuously galvanized reinforcements. Variables also included uncoated (black) and conventional epoxy (smooth epoxy) reinforcements which have been used in structure for many decades. Considering all the tests conducted, an overview analysis was done to determine the best performing bar coating for crack control and rebar-concrete bond. The results show that textured epoxy bars were the best performer in 47% of tests. On the other hand, smooth epoxy bars were the worst performer in 47% of tests. Uncoated, hot dipped galvanized, and continuously galvanized bars were typically in-between textured and smooth epoxy bars in their performance.

This dissertation also analytically evaluated the bond mechanics associated with the variable bar coatings considered in the experimental program. Two different models of bar force variation at and around a crack location were considered to calculate the length over which forces transfer between the bar and concrete. The calculated lengths were compared to data from an associated peer study. It is inferred from the results that a small portion of a bar is de-bonded adjacent to the cracks and the forces transfer gradually at locations beyond the debonding. This inference applies to all the bar coatings in the data except the continuously galvanized reinforcement. Conclusions for continuously galvanized reinforcement could not be made because of limited and randomness in the data.

DEDICATION

I would like to dedicate this dissertation to my beloved parents Mr. Sreedhara Hadya Madappa and Ms. Sudha Malali Lingappa, who have been blessing me all these years, my sisters Ms. Sowmya Praveen, Ms. Shruthi Sreedhara, my brother-in-law Mr. Praveen Puttananjaiah, my beloved advisor Dr. Brandon Ross, co-advisor Dr. Amir Poursaee who have been guiding me since the beginning of my graduate studies and to all my dear friends.

ACKNOWLEDGMENTS

This research project is being funded through WisDOT and the USDOT. Neither WisDOT nor the USDOT assume any liability for the contents or the use thereof nor does this presentation reflect official views, policies, standard specifications, or regulations of either department.

The Contributions made to research by numerous individuals and organizations are acknowledged. Matt Mueller, who was a part of WHRP research has contributed a lot through his guidance in the process and in conducting field studies. Dr. Todd Davis and Dr. Taylor Sorensen contributed to the field study where girder end region crack images were collected and measured using image processing. Clemson students Aaron Murphy, Sam Dodd, Khalil Goodman, Pushkar Rathod, Lancelot Reres, Grace Crocker, Bibek Bharadwaj, Brianna Crabtree, Pawan Acharya, Delaney McFarland and Rumi Shresta assisted with either building formwork, casting concrete, or testing specimens. Aaron Murphy also took the lead on static-load long and short beam test programs. Test fixtures were fabricated with the assistance of technicians Scott Black and Danny Metz. Materials for the test specimens were donated by Sherwin-Williams and AZZ. Roughness measurements were made at the National Brick Research Center with the help of Dr. Nathaniel Huygen and Dr. John Sanders.

TABLE OF CONTENTS

Page

Table of Contents (Continued)

Page

Table of Contents (Continued)

Page

LIST OF TABLES

Page

LIST OF FIGURES

Page

List of Figures (Continued)

Page

List of Figures (Continued)

Page

List of Figures (Continued)

Page

List of Figures (Continued)

Page

I. INTRODUCTION

Overview and Motivation

Structures must be designed to safely withstand estimated loads and to function throughout their life cycle. Serviceability (day-to-day performance) and structural capacity (performance during extreme events) are both critical criteria. This dissertation considers both criteria as they relate to coatings on reinforcing bars in concrete.

In reinforced concrete structures, cracking of concrete is one phenomenon that can affect serviceability and ultimate strength. Under service level conditions, cracking may lead to deterioration of a structure over time. This deterioration can also lead to reduced structural capacity. Reinforced concrete bridge decks are a primary example of how cracks can impact service life and strength. In cold regions de-icing salts can use cracks as a pathway to access the reinforcement and affect corrosion. Salt-water in coastal environments can lead to similar issues. Corrosion of the reinforcement deteriorates structural capacity.

One approach to mitigate the impacts of cracking is to "control" the growth and propagation of cracks. Another is to provide coatings on steel reinforcement create a barrier and prevent corrosive materials from accessing the steel and initiating corrosion. In many cases coatings impact crack control and reinforcement-concrete bond as well as providing a barrier. This dissertation is concerned with how coatings (or lack of coating) on the reinforcement impacts crack control and reinforcement-concrete bond.

Multiple series of structural and material tests were conducted, and the variables were the coatings of the reinforcements (Figure 1). By understanding the effect of

coatings on crack control and reinforcement-concrete bond, this research aims to facilitate serviceable, durable, and strong reinforced concrete structures.

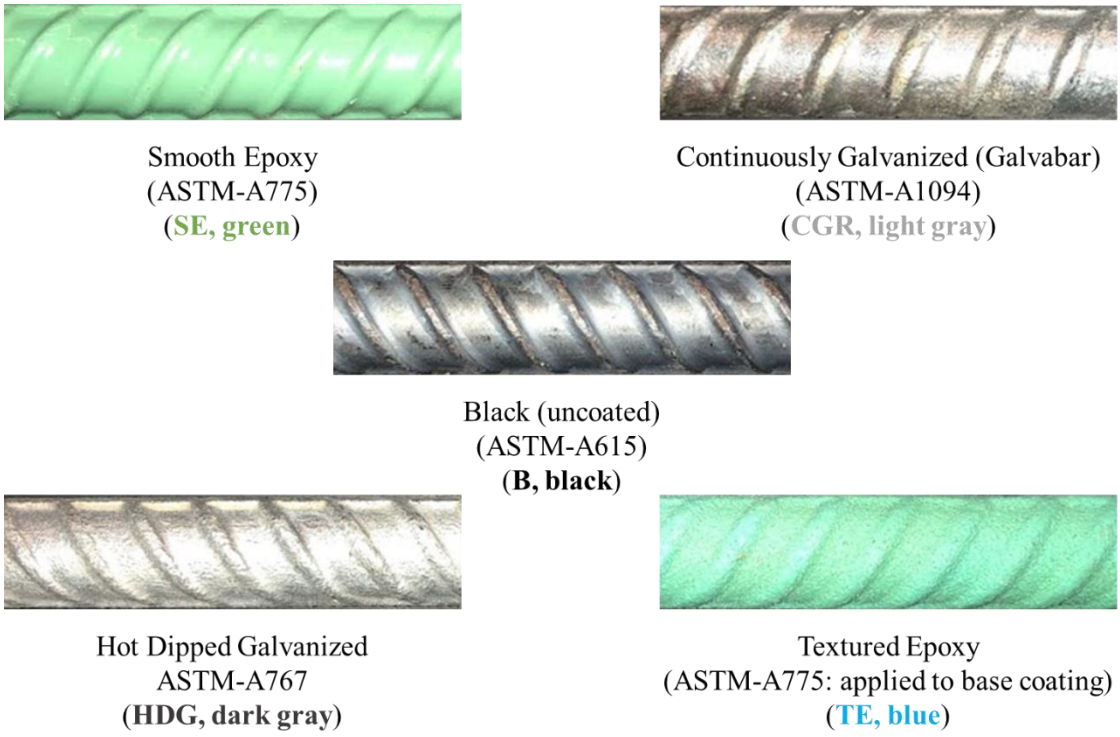

Figure 1. Reinforcement coating variables along with the notations and specifications

Relationship of dissertation to Wisconsin Highway Research Program Project

This dissertation is a part of a larger experimental program reported in Ross et al. WHRP report [1]. Portions of the larger program were also reported by Murphy [2]. While this dissertation research was associated with the larger project, it goes beyond the work that has been previously reported. For example, the project report discussed a series of bond tests at a high level. The current dissertation provides further discussion,

including a comparison with code-based development length provisions. Another example is the additional analysis conducted using beam crack data collected by Murphy. Murphy conducted the tests and documented the procedure and overall results in his thesis. The current dissertation uses the Murphy data to estimate flexural bond lengths for the variable coated reinforcements in concrete.

In addition to the lab testing and analysis, this dissertation also presents a methodology paper on the use of Image Processing in field studies of cracking in concrete structures. The methodology paper is presented in Chapter VIII. The method described in the paper was utilized for lab studies presented throughout this dissertation.

Hence, this dissertation is related to other efforts conducted in the larger project, however, it presents unique contributions made by the dissertation author. Some parts of the WHRP project report originally drafted by the dissertation author are also included in this dissertation.

Overview of experimental program

Laboratory studies were conducted involving all the types of rebar (Figure 1) with a set of specimens of each bar for each test. Bar coatings and test methods are shown in Table 1. Overall, four different types of tests were conducted for this dissertation. The tests were carried out to evaluate the crack control and bond behavior of all the types of rebar under different conditions of loading. Not all the bar types were considered in all of the tests. Variables were selected on a test-by-test basis and reflect the available materials at the time of the test. In hindsight it would have been preferable to have all bar

coatings represented in all test types; unfortunately, this is not how the tests were conducted.

Table 1. Overall laboratory test program showing the type of bar used in each test

Bar Coating	**Test Type**			
	Shrinkage Cracking	**Bond**	**Static load cracking**	**Prism Tension**
Black (B)	X	X	X	X
Smooth Epoxy (SE)	X	X	X	X
Texture Epoxy (TE)	X	X	X	X
Hot-dipped galvanized (HDG)	X			X
Continuously galvanized (CGR)	X	X	X	X
Number of series	**8**	**4**	**3**	**3**
Total number of specimens	**40**	**16**	**12**	**15**

Comparison Index

Many of the results are presented in terms of the "comparison index." To aid the reader in understanding and interpreting results, this section explains the comparison index.

Data for each test were normalized to the average performance of all the specimens in each series to facilitate the comparison between test types, series, and coatings in performance. A factor called Comparison Index was calculated for each specimen in each series to present the results with their performance to the normalized value. This comparison index is equal to the measurement value for a specimen divided by the average measurement for all other specimens in the same series. A value greater than 1.0 indicates poorer than average performance, whereas a value less than 1.0 indicates superior than average performance. An example calculation of comparison index is shown in Table 2. The specimen with the smooth epoxy bar in the example had a

comparison index of 1.20 meaning that the specimen's crack width was 20% larger than the average of all other cracks in the series. It was calculated by dividing the specimen width by the series average, i.e., 0.023 in. / 0.019 in. = 1.20.

Table 2. Example showing comparison index (values are not from a specific test, considered just for this example)

Bar Coating	**Crack Width (in.)**	**Comparison Index (Specimen crack width / series average)**
Black	0.018	0.94
Smooth epoxy	0.023	1.20
Texture epoxy	0.016	0.83
Hot-dipped galvanized	0.019	0.99
Continuously galvanized	0.020	1.04
Series average	0.019	

Research questions addressed in this dissertation

The overall program of which this dissertation was associated, focused on bar coatings and their impact on crack control, specifically for bridge structural elements. This dissertation addresses the same subject matter but includes additional work investigating the topic at a more fundamental mechanics-based level. Digital image analysis was a key tool in the research. This dissertation also includes a manuscript on the use of digital image analysis to study cracks widths in field studies.

The content in this dissertation can be summarized by the following questions:

- What is the relative strength of concrete-reinforcement bond for alternative coated reinforcements? This question is primarily addressed through the experimental program reported in Chapter IV.

- How should textured-epoxy coated bars be considered in code-based requirements for development length? This is also addressed in Chapter IV.
- What is the relative impact of alternative reinforcement coatings on the control of shrinkage cracks? The test program reported in Chapter V addressed this question.
- To what extent (if any) does reinforcement coating impact residual crack width in concrete structures after loads have been removed? This is discussed in Chapter VI.
- Are theories of rebar-concrete bond mechanics applicable to bars with alternative coatings? The question is addressed in Chapter VII.
- What is the process for using image analysis in field studies of cracking concrete structures? A manuscript on this topic is presented in Chapter VIII.

These questions will be revisited in the conclusions part of each chapter after the data and analyses have been presented.

II. BACKGROUND

Cracking in concrete structures

It is widely known that concrete has a relatively low tensile strength and that cracking of concrete structures is a ubiquitous problem. For this reason, numerous studies have been conducted on concrete cracking over the years. There are 3660 research articles identified by Google Scholar [3] related to the “concrete cracking” just for the year 2021. Cracking in concrete bridges was studied collectively by the National Co-operative Highway Research Program (2017) [4] which is available in its Synthesis Report No. 500.

The phenomena, confounding issues, and mitigation of concrete cracking are well demonstrated in bridge decks. Cracking and associated issues result in decks having the shortest service life on any bridge element (Figure 2). Bridge decks receive the load directly by traffic and are exposed to snow and rain, and in some locations de-icing chemicals. Cracks make the intrusion of corrosive agents easier, inducing higher risk of corrosion of steel reinforcement [4]. This limits the service life of concrete bridge decks effectively [5] and the rate of corrosion activity can be mitigated by controlling cracks [6].

Figure 2. Photo of cracking in bridge under the deck (Figures from [7])

Previous research has identified many factors that can affect the occurrence and extent of cracking in concrete bridge decks ([4] and [8-13]):

- Environmental conditions during concrete placement and curing,
- Concrete mix design and material properties,
- Construction practices during placement and curing,
- Reinforcement details,
- Bridge layout (i.e., skew and span),
- Structural stiffness,
- Bearing conditions and restraints,
- Corrosion and chloride content,
- Thermal loads and freeze-thaw cycles, and
- Structural loads.

There are many approaches to mitigate corrosion in bridge decks that have been studied earlier [14-20] like sealing the cracks and laying overlays on deck surface,

injecting the cracks with epoxy resins or any sealants, coating the steel reinforcement and using reinforcement made of corrosion resistant alloys.

Both cracking in bridge decks and corrosion in bridge deck reinforcement can be mitigated by using a coated reinforcement. The impact of alternate coated reinforcements is not considered in this dissertation on the topic of reinforcement corrosion which is expansive and has been the subject of much research on its own. This dissertation focuses only on the impact of coatings on crack control and bond in concrete.

The end region of precast-pretensioned concrete girders is another common location for cracking (Figure 3). The concentrated prestressing forces causes end region cracks due to the induced tensile stresses which are distributed from the point of application of prestressing force in the bottom flange to other parts of the girder cross-section (Figure 4).

End region cracks have been studied for decades and there is a large body of literature discussing causes and mitigation strategies. The topic has recently been the focus of projects from the Wisconsin DOT [21], Florida DOT [22], Alabama DOT [23], and National Cooperative Highway Research Program [24]. Factors associated with end region cracking include:

- Cross-section geometry,
- Magnitude and location of pretension forces,
- Detailing of end region reinforcement, and
- Concrete tensile strength at the time of prestress transfer.

Partial debonding of select strands has been shown to reduce end region tensile stresses and the resulting cracks ([21], [22], and [25]). More aggressive approaches for preventing or reducing end region cracks include the use of ultra-high-performance concrete regions [26] and the use of vertical post-tensioning [27] in the end region. The effect (if any) of alternative reinforcement coatings on end region cracks has not previously been considered.

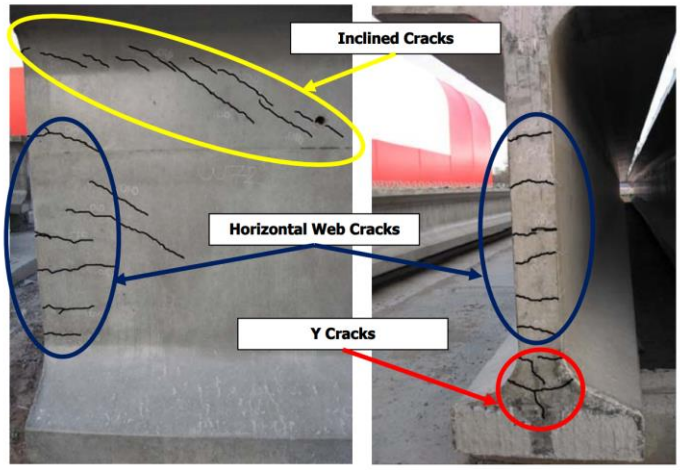

Figure 3. Type of end region cracks (Figure from [21])

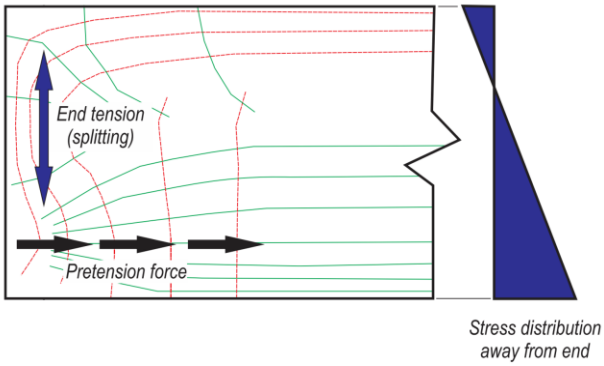

Figure 4. End region cracks form due to tensile stresses (green trajectory lines) which form as the pretension force is distributed from the bottom flange to the rest of the cross-section. (Figure based on [25])

Reinforcing bars and coatings

The first specification for steel reinforcing bars was issued in 1910 [28]. Since then, there have been various advances in reinforcement including coatings that have been innovated to mitigate corrosion. The following paragraphs briefly introduce the bars and coatings that were used in the laboratory tests in this research.

Black (uncoated). All bars in the test program started as uncoated bars that complied with ASTM-A615 [29].

Smooth-epoxy coated. Conventional epoxy-coated bars are labeled as "smooth" in this dissertation to differentiate them from the novel textured-epoxy coated bars that were also used as another variable in the tests. Smooth-epoxy coated bars complied with ASTM-A775 [30]. The epoxy coating is applied over an ASTM-A615 black bar. The epoxy coating acts as a barrier between the bar and corrosive materials to mitigate

corrosion. Smooth epoxy bars have been widely used since 1973 when it was first implemented in a bridge in Philadelphia, PA [31].

The coating process begins with abrasive cleaning to remove rust and mill scale from the bar surface. The bar is then heated in an oven or through induction heating, whereafter a charged epoxy powder is applied using an electrostatic spray nozzle. The heat and the charge adhere the powder to the surface resulting in the epoxy coating. The coated bar is water quenched to cool. After cooling the bar is checked for "holidays," which are small cracks or pinholes that are often too small for visual observation. Holidays are identified by passing a current through the bar and noting any electrical continuity through the coating. The process from cleaning to holiday checking can be automated and can take only a few minutes. ASTM-A775 specifies the permissible level of coating damage and repair methods. Per ASTM-A775, the epoxy coating thickness is between 7 and 12 mils (175 μm and 300 μm) for bar sizes Nos. 3 to 5.

Textured-epoxy coated. Textured-epoxy is a novel coating designed to mitigate corrosion while also having a rough surface that is suitable for the concrete bond. The fabrication involves a two-coating process. The primary coating process is like that described in the previous paragraph for the smooth-epoxy coated bar. The second coating process begins with another powder spray that creates the texture which plays a vital role in improving the bond strength. Currently, there is not an ASTM standard for textured-epoxy coated bars; however, the initial coating used in the textured bars complies with ASTM-A775 [30]. Because of the two-coating process, the total thickness of epoxy on the textured bars used in the current project was approximately 0.67 mm (69

%) thicker than the smooth epoxy coating. While the conventional epoxy bar has a smooth and shiny surface, the textured-epoxy bar has a rough and gritty surface (Figure 1**Error! Reference source not found.**).

Hot-dipped galvanized. Galvanizing is a zinc coating that is chemically bonded to the steel surface to mitigate corrosion. Hot dipping is the most common method to apply galvanizing. Hot-dipped galvanizing, often called "batch galvanizing", involves immersing clean and pre-fluxed steel in a kettle of molten zinc at about 450^{o}C. During the immersion time, while the steel is heated to the temperature of the molten zinc, a metallurgical reaction occurs between the steel and the zinc [32]. Hot-dipped galvanized bars in the project complied with ASTM-A767 [33].

The reaction between steel and molten zinc produces a coating on the steel made up of iron zinc alloy layers that grow from the steel/zinc interface, with a layer of essentially pure zinc at the outer surface. What distinguishes galvanizing from other types of coatings is that the galvanized layer is metallurgically bonded to the steel due to inter-alloying between the steel and the molten zinc. A key feature of hot-dip coatings is that the outer layer that remains on the surface of the product as it is withdrawn from the kettle and is generally about 40-50 μm thick. It is the presence of this "eta layer" that controls much of the behavior of zinc when in contact with wet cement [32].

Continuously galvanized. Continuously galvanized rebar was developed in China in 2011 and introduced to the American market in 2018 under the trade name GalvaBar [34]. The continuous coating is applied using an in-line (thus not batch dipping) process similar to the coating of sheet and pipe products. A blast cleaned and

preheated bar is fed through a molten zinc bath for not more than 1-2 s [35], and the total time at temperature including the preheating stage is not more than 4-5 s. By adding a small amount of aluminum (0.2%) to the zinc bath, a coating typically 50-60 μm thick is produced that is almost entirely pure zinc, with only a very thin layer (approximately 0.1 μm) of a ternary ($Fe_2Al_{5-x}Zn_x$) alloy at the zinc/steel interface. Apart from the economy and speed of production with the continuous galvanizing method, a reported feature of this type of coating is the improved formability of the coated product [32].

Surface Roughness

The surface of the bar impacts the strength of the bar-concrete bond. This has been studied extensively in case of smooth epoxy bars [36-38]. Surface roughness of bars is positively related to the bond strength. This is the very phenomenon that motivated this project to consider textured-epoxy bars.

Bond and crack control

Transfer of forces between concrete and embedded steel bars, i.e., reinforcement-concrete bond, can occur through cohesion, adhesion, and through mechanical interlocking between the bar deformations and concrete. The contributions of these mechanisms are conditional upon the level of force being transferred, surface coating of the rebar, and geometry of bar deformations. Adhesion and cohesion (if present) are primary at small load levels and mechanical interlocking is primary at ultimate load

levels [39]. The interlocking mechanism is described in Figure 5. Equal and opposite bearing forces act normal to the bar deformations. The longitudinal component transfers the force between the bar and concrete, while the radial component leads to tensile stresses in the surrounding concrete. The tensile stresses can lead to splitting cracks depending on the confinement, cover, and spacing of the bars.

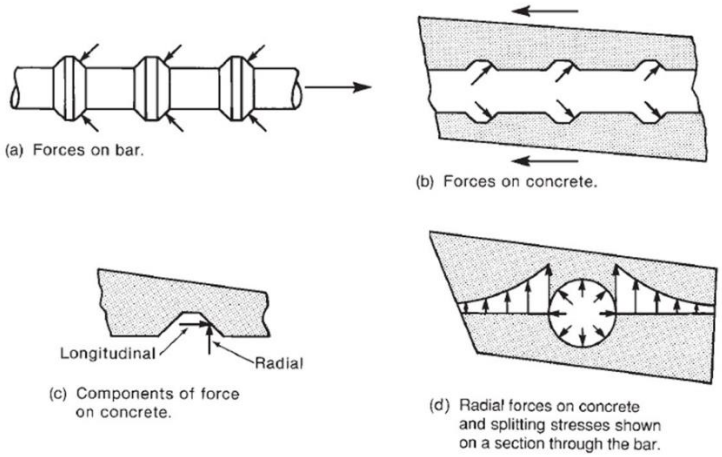

Figure 5. Bond transfer mechanism (Figure from [40])

Multiple parameters impact the transfer of forces between bars and concrete. Darwin and Graham [41] observed that initial (low load) slip resistance and ultimate bond strength increase as the relative rib (deformation) area increases. Relative rib area is the ratio of rib area normal to the bar axis to the product of nominal bar perimeter and rib spacing.

The effect of epoxy coating thickness on deformed bars and bar parameters on bond strength in concrete was studied by Chul Choi et al. [36]. It was concluded that epoxy coating in deformed bars has a greater effect in reducing the bond strength as the

bar size increases. Also, the higher the bearing area due to the rib deformation pattern in bars, the lower the effect of epoxy coating on the reduction of bond strength in concrete.

In case of galvanized bars, due to the presence of pure zinc and formation of zinc oxide and zincates, it retards the setting of concrete and initially reduces the adhesion with the concrete. However, it is determined that adhesion with concrete at the surface can increase over time and improves the bond strength [42 - 44]. The bond strength of hot-dipped galvanized, epoxy-coated, and uncoated bars in 28-day concrete was studied by Kayali and Yeomans [45]. They reported that there is no statistically significant difference in bond strength between uncoated and hot-dipped galvanized bars in 28-day cured concrete. A reduction in bond strength of 25% to 42% was observed in the epoxy-coated bars.

Kim and Andrawes [46, 47] experimentally tested the bond behavior of textured-epoxy coated, smooth-epoxy coated, and uncoated bars. It was observed that textured-epoxy and uncoated bars had higher slip resistance relative to smooth-epoxy coated bars. Additionally, the textured-epoxy-coated bars had greater crack control performance than both the uncoated and epoxy-coated bars. They also presented an approach for simulating the textured-epoxy coating finite element models [37]. The current dissertation adds to the work by Kim and Andrawes by evaluating textured-epoxy bars using different test methods, including shrinkage crack testing. Comparisons of textured-epoxy coating with hot-dipped and continuously galvanized bars is another distinction of the dissertation.

Shrinkage cracking

Shrinkage phenomenon in concrete results from a reduction in its volume during moisture loss. If the concrete is restrained from shrinking, then this phenomenon can lead to stress build up. Cracking occurs when the tensile stress exceeds the tensile capacity of concrete. This can happen even when there is no external load applied (ACI committee 209, 2005) [48]. In case of reinforced concrete members, the presence of rebar adds stiffness to system and controls the amount of shrinkage strain in the concrete [49]. When cracks do form, the rebar acts to control the width of shrinkage cracks.

In a recent study at the University of Illinois [50] researchers measured the strain in textured and smooth epoxy coated bars in lab specimens that mimic concrete bridge decks. The concrete decks were simply supported and spanned 16.5 ft. The effects of shrinkage on the concrete were monitored for 59 days after curing. The change in strain was monitored using strain gauges attached both on the rebar and underside of the concrete. Concrete strain was also monitored by the changes in the speckle dot pattern on a portion of the slab using digital image correlation (DIC). From the strain gauge data, it was observed that larger strains were recorded on the textured epoxy rebar compared to that of the smooth epoxy. This shows that textured epoxy offered more resistance against shrinkage compared to that of smooth epoxy. The DIC data showed that the deformations in the monitored portions of the slabs were on an average 21% smaller for slabs with textured epoxy rebars than slabs with smooth epoxy bars.

III. ROUGHNESS MEASUREMENTS

As textured-epoxy bars can be produced with different levels of surface roughness, it is necessary to measure and document the roughness. Also, it was intended to corelate the measured surface roughness of all the variables involved to the overall crack control and bond performance.

A VHX-7000 Keyence optical microscope was used to measure the surface roughness from samples of each coating type. The VHX-7000 has a depth of field that is 20 times greater than conventional optical microscopes. It can deliver 2D and 3D measurements, roughness, contamination, grain size, and other analyses with one tool. Additionally, observation can be carried out automatically at magnifications from 20× to 6000× without changing the lens.

Measurement parameters considered for the bar specimens include *Sa*, the arithmetical mean height of a surface, and *Ra*, the arithmetical mean height along a line. At the scale of rebar surface roughness, *Ra* and *Sa* are typically reported in micrometers. In common language, *Ra* and *Sa* can be described as the average height of the peaks and valleys relative to the overall average height of the surface. Two locations on each specimen were used for collecting roughness measurements, one on the longitudinal rib and the other between the transverse ribs. Example microscope surface images for textured-epoxy and smooth-epoxy coated bars are shown in Figure 6. The surface at each measurement location was then divided into three strips of approximately the same size. Sa was measured over the area of each strip. The centerline section in each of those strips were measured for Ra (Figure 7). The same procedure was followed for both the

locations in the bar i.e., on the longitudinal rib and between the transverse ribs. Three specimens were measured for each bar coating and there were six measurements of Sa and Ra in each specimen.

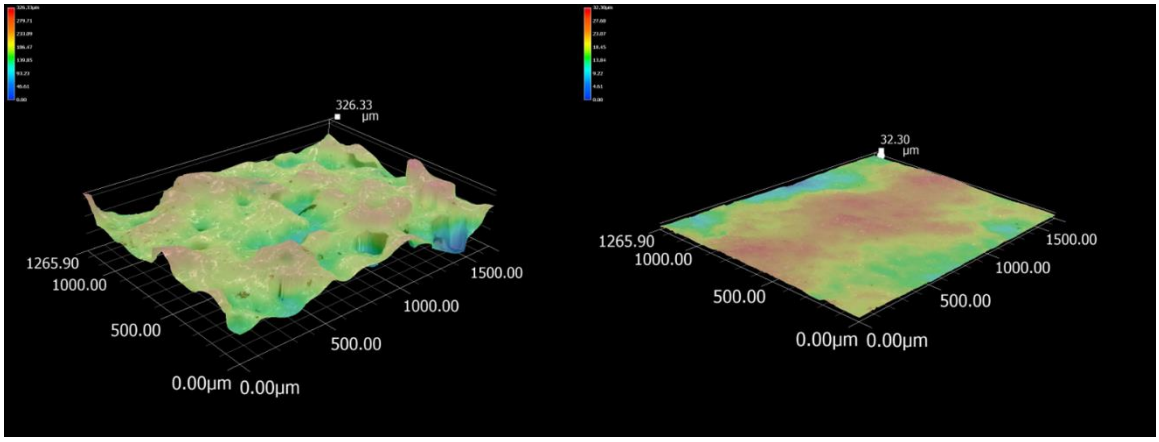

Figure 6. Microscope images of textured epoxy bars (left) and smooth epoxy bars (right) showing surface roughness. Note that the dimension (length) scales are comparable between the images, but the color scales are not.

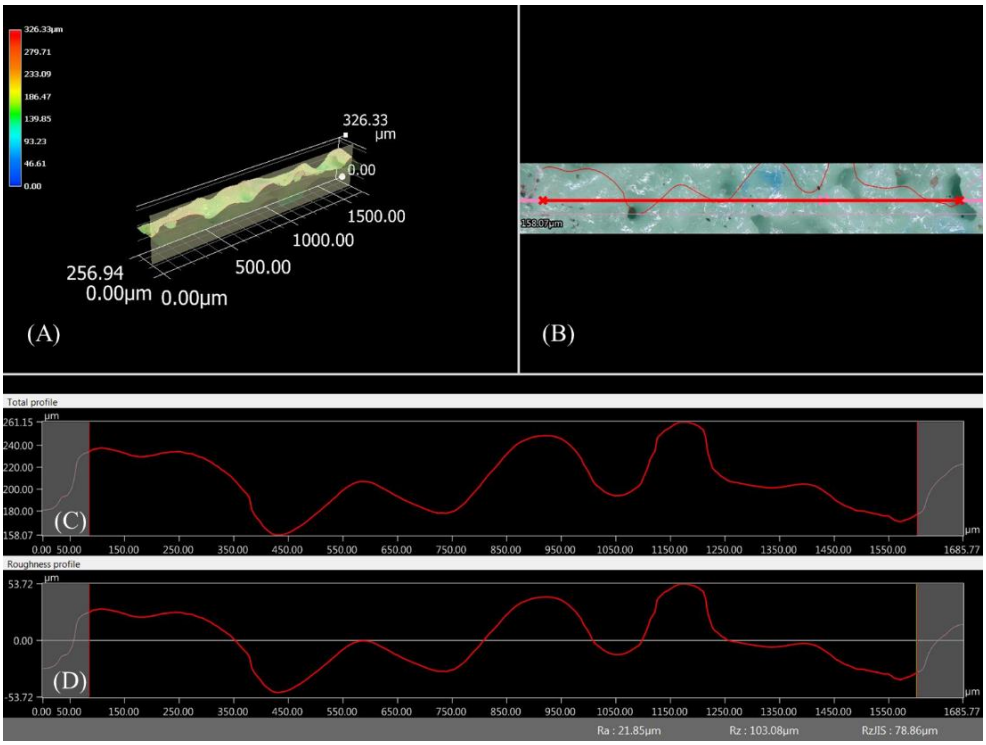

Figure 7. Measurement of Ra. A) The surface roughness of a given strip. B) Line through strip for determining Ra. C) Profile of surface along line. D) Profile surface normalized to the mean profile height. Ra is the average absolute deviation from the mean profile height.

The average of measured values is shown in Figure 8. Values in the figure for a given coating type are the average of measurements taken at two locations on each of three bar samples. The values in the figure were corrected to account for the round surface of the bars, which impacted the microscope roughness measurements. The correction was automated in the software used to run the microscope.

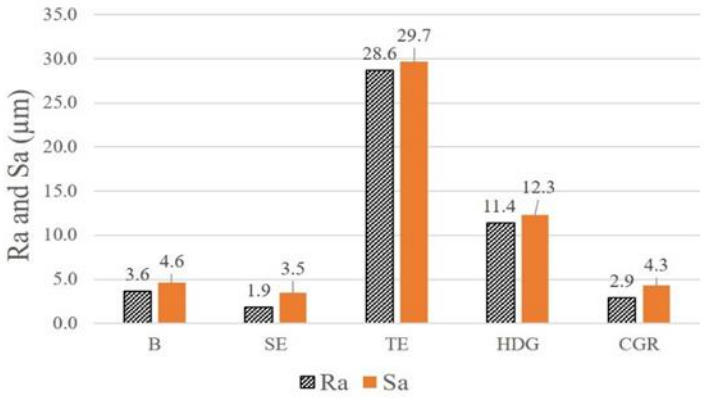

Figure 8. Roughness measurements for each bar coating type

The microscope-measured roughness for the textured-epoxy bars was 28.6 µm and 29.7 µm for Ra and Sa, respectively. The next roughest surface was hot-dipped galvanized. Smooth-epoxy coating produced the smoothest surface with measurements of 1.9 µm and 3.5 µm for Ra and Sa, respectively.

IV. BOND TESTS

Overview

This chapter addresses two research questions:

- *What is the relative strength of concrete-reinforcement bond for alternative coated reinforcements?*
- *How should the implementation of textured-epoxy coated bars be addressed considered in code-based requirements for development length?*

ACI-318 [51] and other codes require epoxy coated bars to have greater development length. At the same time, galvanized bars have the same requirements as uncoated bars. This research experimentally evaluated two new coatings, specifically textured epoxy and continuously galvanized, to determine their bond and development length performance.

Test set-up

The bond tests followed the specifications of ASTM A944 [52]. Figure 9 shows the specimen reinforcement detailing. The clear cover for the test rebar was 2 inches. From the edge of the concrete the test bar is debonded over a "lead length" of 0.5 inches. After the lead length, the bars were bonded over lengths 4 inches or 6 inches. After the bonded length the rest of the test bar was debonded to the opposite end of the specimen. Debonding in the lead length and in the debonded length were achieved by placing a

PVC pipe to surround the bar. Secondary reinforcements were detailed and placed according to ASTM A944.

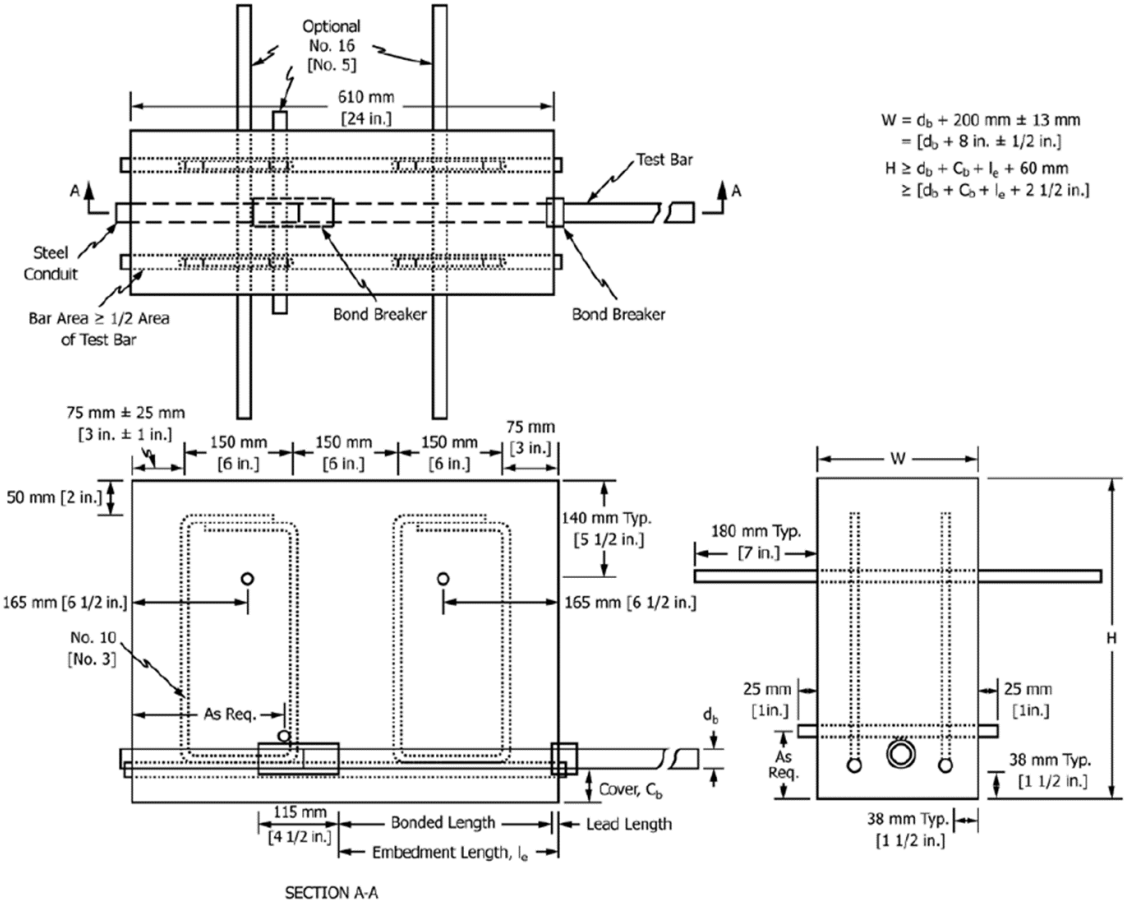

Figure 9. Bond test specimen detailing from ASTM A944[52]. The width, W, for the specimens in the test program was 9 inches and the height, H, was 26 inches. The length parallel to the test bar was 24 inches.

Four series of tests were conducted, and each series included four specimens, for a total of 16 (Table 1). Four sets of wood forms were built and were rotated for each bar type in the subsequent batches. The concrete mix design was based on a South Carolina Department of Transportation (SCDOT standard). The mix design is shown in Table 3.

The same mix design was used for each series. Each of the tested bar coasting types was included in each series so that any variations in the concrete mix would affect all bar types.

All the specimen formworks were inverted, meaning that the test bar was cast at the bottom of the specimens. The concrete was cast in three layers to ensure consolidation of concrete. After each layer was poured, the concrete was consolidated using a vibrator. Concrete cylinders were also cast from each bath of concrete. Formworks were removed after one week and specimens were tested only after the concrete has reached the strength of 4500 psi minimum.

Table 3. Concrete mix design for casting bond test specimens

Concrete mix design	
Material	**Design Quantity**
Cement (Type I/II)	500 lb
Fly Ash	125 lb
Coarse Aggregate	1825 lb
Fine Aggregate	883 lb
Plasticizer	-
Water	35 gal
Air Entrainer	-
Air Content	-
Water/Cement	0.467
Slump	3 in

The test set-up is shown in Figure 10. A steel frame (Figure 11) supported the specimen during testing and consisted of a vertical HSS is welded on top of an I-beam. Two channel sections were welded side by side to the I-beam to support the bearing reaction of the specimen. Channels and rods were used as hold downs to maintain static equilibrium during testing. Each specimen was moved, inverted, and placed on the steel

frame using a hoist. Holes in the HSS allowed the test rebar to pass through and engage a hydraulic jack. For practical purposes with holes in the HSS were oversized (approximately 4 inches diameter) to avoid contact with the test bar during setup. A strand chuck was used at the loading end of the bar to engage the hydraulic jack. The load data was collected using the load cell which was placed between the hydraulic jack and the strand chuck and a pressure gauge from the jack.

Figure 10. Bond test set-up

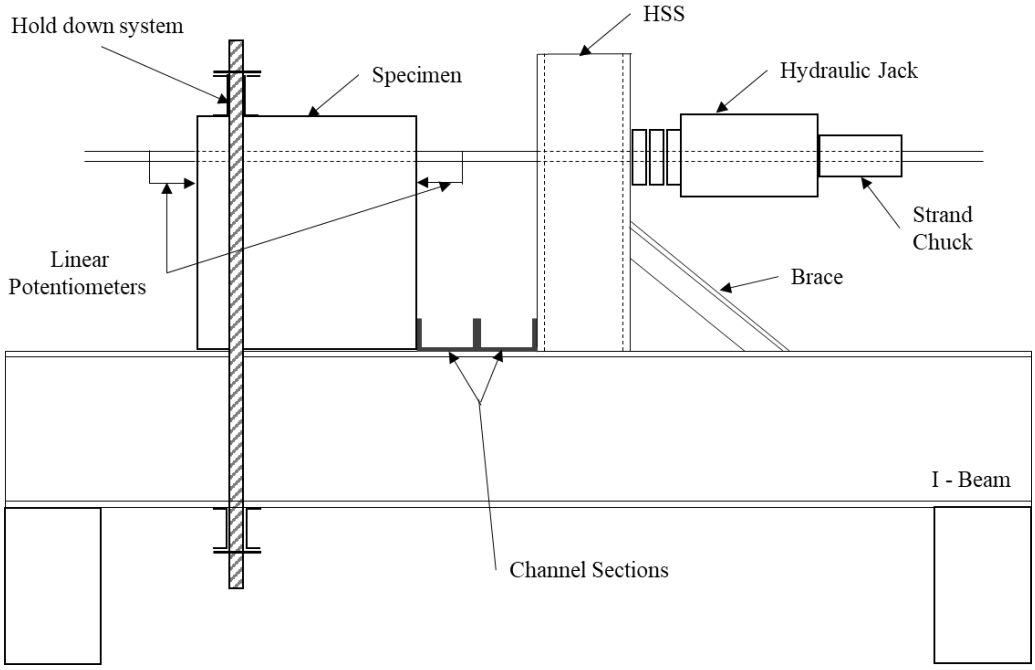

Figure 11. Sketch of the specimen set up on a steel frame in bond test

The slip and the displacement data were collected using linear potentiometers. Two potentiometers were placed at the rear end of the specimen and two were placed at the loading end of the specimen. The linear potentiometers, load cell and the pressure gauge were calibrated and connected to the DAQ system for the data collection. Typically, the bar was pulled with the jack until the concrete cracked and the bond failed, or well past the apparent yielding point of rebar. Photos were taken after completing the tests to document cracking.

Series one and two used a 6” bonded length, which resulted in yielding of the reinforcement prior to concrete cracking and bond failure. To bound the minimum bonded length required to reach yielding, the bonded length was changed to 4” in series 3 and 4.

Test Method Validation

The beam end testing method results followed according to the ASTM A944 are validated with the available literature. This test has previously been conducted on black, smooth epoxy and hot dipped galvanized bars. Slip values of Black bars from Platt and Harries [39] and Smooth epoxy bars from Kayali and Yoemans [45] are compared against the test data from this dissertation to validate the test method. The comparison is shown in the Table 4. As seen in the table, results from the current test program are similar to those from the previous studies.

Table 4. Bond test data validation from literature

Bar type	**Bonded Length (in)**	**Slip (in)**	**Bar stress (psi)**
Black (Platt & Harries)	6.65	0.00035	40320
	6.65	0.00078	51630
Black	6	0.00042	40255
	6	0.00079	51655
Epoxy (kayali 7 Yoemans, 2000)	5.9	0.00098	33180
	5.9	0.00196	44000
Smooth Epoxy	6	0.00073	33665
	6	0.00128	44100

Test Results

The whole test was monitored using a data acquisition system and testing was stopped when a splitting failure occurred in the concrete adjacent to the bonded length (Figure 12) or when it was obvious that the reinforcement was well past yielding.

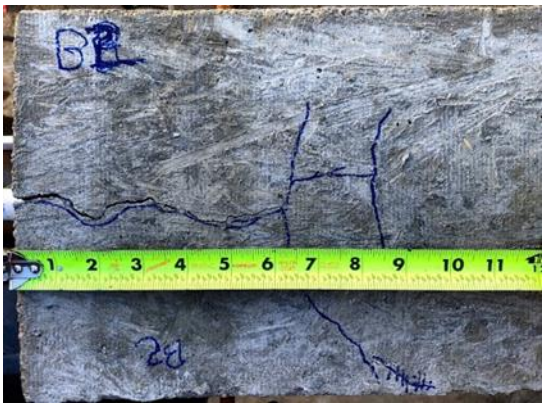

Figure 12. Splitting failure in Black bar specimen in series 2 with bonded length 6 in

Results have been studied considering two aspects. First, the slip measured at the back end was evaluated with respect to the load. Second, the displacement at the front of the bar (which included slip and elongation) was evaluated to determine if the bar yielded.

Series 1 and 2 had a bonded length of 6 in., which was sufficient for all specimens to reach full development. In other words, all bar types were able to support the minimum specified yield stress. The minimum specified yield stress for all bars was 60 ksi, which corresponds to a load of 12 kip. Series 3 and 4 had a bonded length of 4 in. In series 4, the uncoated and smooth-epoxy specimens only reached 11.2 kip and 10.5 kip, respectively.

The data from the two potentiometers from the front end (Figure 10) is plotted for load vs displacement which is shown in Figure 13. The displacement reported in the figure is the average from the two instruments. The plot is from series 1 where the bonded length was 6 in. It can be observed that the displacement was approximately linear elastic at the beginning of the tests and that the bars began yielding at loads higher

that 12 kips. At a given load level the displacement measured at the front of the specimen was always greater than the slip measured at the back. This is because the displacement measurement included elongation of the bar.

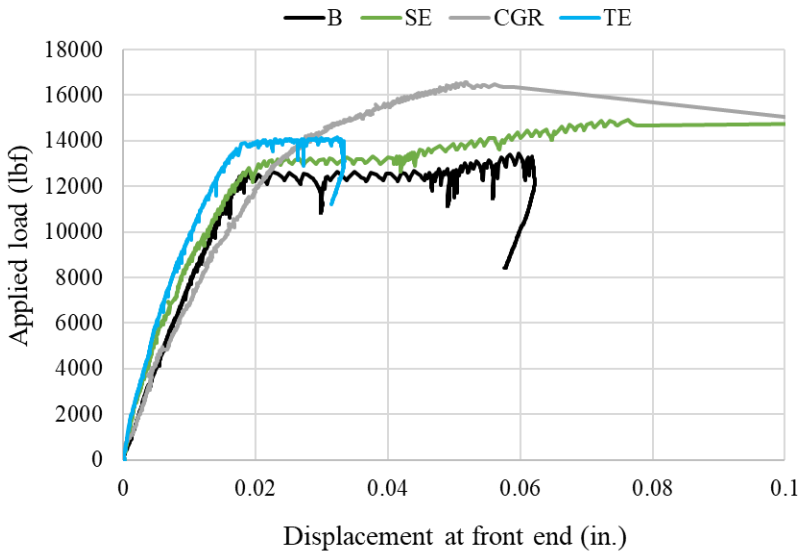

Figure 13. Load vs Displacement for series 1 with bonded length 6 in

The data from the two potentiometers from the back end (Figure 10) is plotted again the applied load for series 1 in Figure 14. The amount of slip was small when the load was initially applied. The slip increased significantly as the load approached the specified yield strength of the bar.

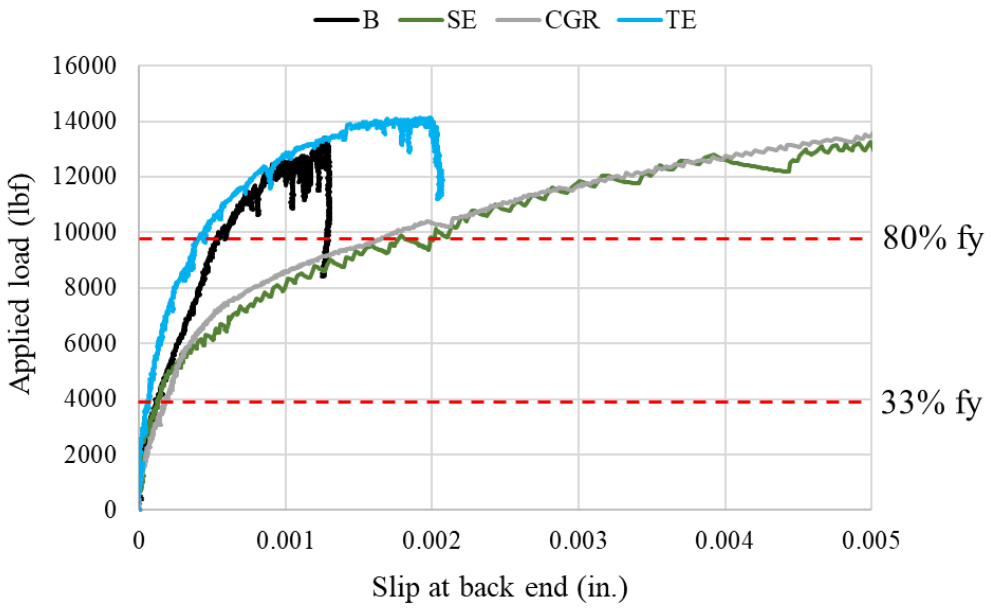

Figure 14. Load vs Slip for series 1 with bonded length 6 in

To compare the slip between specimens with different bar coating types, two benchmark stress levels were selected. The first benchmark was 33% of the yield stress, which corresponds to service-level stresses. The second benchmark was 80% of the yield stress, which was approaching but less than ultimate strength. Comparison index values were calculated for all specimens and are reported in Figure 15. Two trends are noted from the comparison index values. First, textured-epoxy bars had the lowest slip in seven of the eight comparisons. The only exception was the 33% load level in series 4. Second, the smooth-epoxy bars had the greatest slip in five of eight comparisons. These trends indicate that the textured-epoxy bars have superior bond capacity than the smooth-epoxy coated bars. From this result, it is reasoned that textured-epoxy bars should not be treated the same as smooth-epoxy coated bars when calculating development length. Additional

testing is recommended to confirm this observation and to determine the range of roughness properties and concrete strengths for which it is valid.

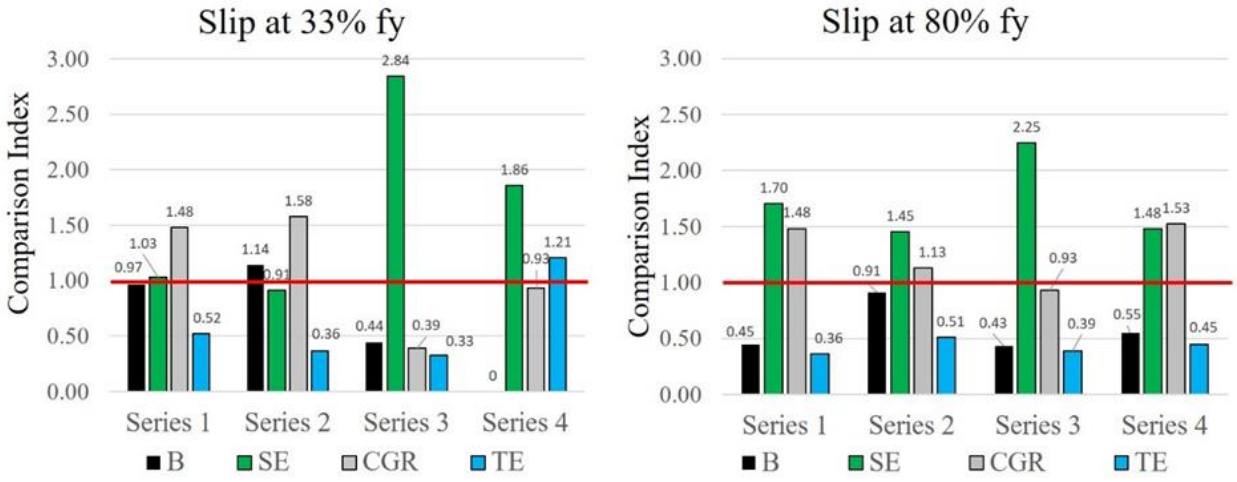

Figure 15. Comparison Index of bar slip at 33% f_y and 80% f_y stress levels. An instrument malfunction prevented measurement of slip in B4 at the 33% fy level.

To get an overall understanding of the slip resistance of each variable comparatively, comparison index data is shown in box and whiskers at both the stress levels. It can be seen from the Figure 16 that the smooth epoxy values are typically greater than 1.0 indicating that the slip incurred in those specimens were more than the average slip value at both the stress levels. Continuously galvanized rebar (CGR) tends to have higher than average slip at the 80% f_y stress level and approximately average slip at the 33% fy stress level. While black bar and textured epoxy bars always had lower than average slip at the 80% fy stress levels. In particular, the range of values for the textured bars was well below the average at the higher stress level, indicating desirable bond performance.

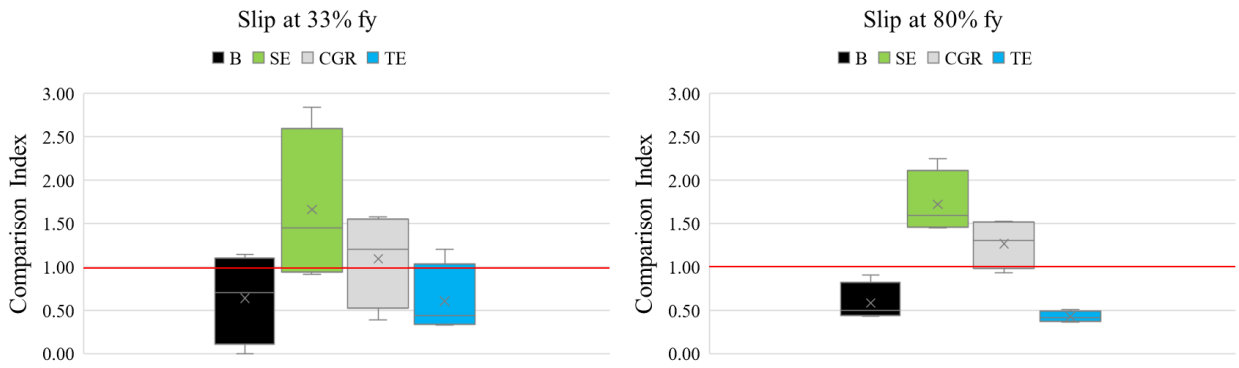

Figure 16. Box and whisker plots of bar slip at 33% f_y and 80% f_y stress levels

Code Comparison

Development length is the length of embedment of a bar in concrete required to develop the specified yield stress in the bar. The ACI 318-19 [51] provisions for tension development length includes various adjustment factors based on the conditions of the bar being developed. One of the conditions considered is the presence of coating on the bar. The introduction of the coating factor in ACI 318 was based on prior literature [53-55]. In a study conducted by Jirsa and Treece [55], 21 beams with lap spliced reinforcement in the constant moment region was tested and the bond strength of epoxy coated bar specimens were compared to that of Black (uncoated bars). The ratio of bond strength of epoxy coated bars to that of uncoated bars was formulated. It was determined from the overall tests that the bond strength of epoxy coated bars was about 65% of the bond strength of uncoated bars in case of a splitting failure. A factor of 1.15 or 1.5 were recommended for design considerations based on cover and spacing of the bars in concrete. In this dissertation, the average ratio of slip values both at 33% fy and 80% fy

stress levels were calculated as most of the specimens were developed to yield prior to the failure. The slip resistance was the parameter of comparison between the specimens. At 33% fy stress level, the average ratio of slip in case of smooth epoxy specimen to that of uncoated specimen was 0.94 and at 80% fy stress level, it was 3.32. While the current program measured different parameters than Jirsa and Treece [55], both programs demonstrated that smooth epoxy coated bars have reduced bond strength relative to black bars.

The coating factor ψ_e is defined as 1.2 or 1.5 for epoxy coated rebar and 1.0 for uncoated rebars or zinc coated rebars (Table 25.4.2.5, ACI 318-19). The same is not defined for textured epoxy coated rebar, but it is assumed as 1.0 to compare against the other three bar coatings. ACI provides two approaches for calculating the required development length. The relevant equations are given below. Regardless of the equation results, the minimum development length required as per ACI 318-19 is 12 inches.

$$l_d = \left(\frac{3}{40} * \frac{f_y}{\lambda\sqrt{f'_c}} * \frac{\psi_t\psi_e\psi_s\psi_g}{\left(\frac{C_b + K_{tr}}{d_b}\right)}\right)d_b$$

Equation 1. Development length equation from 25.4.2.4a (ACI 318-19)

$$l_d = \left(\frac{f_y\psi_t\psi_e\psi_g}{25\lambda\sqrt{f'_c}}\right)d_b$$

Equation 2. Development length equation from 25.4.2.3 (ACI 318-19)

All the factors considered for the calculation are:

$f_y = 60\ ksi$

$\lambda = 1.0$

$\psi_t = 1.0$

$\psi_e = 1.2\ (SE), 1.0\ (B, CGR, TE)$

$\psi_s = 0.8$

$\psi_g = 1.0$

$d_b = 0.5\ in$

$C_b = 2\ in\ (Concrete\ cover\ to\ the\ center\ of\ bar)$

$K_{tr} = 0\ (no\ transverse\ reinforcement)$

$f'_c = 5200\ psi, 6900\ psi, 7200\ psi, 4600\ psi\ (in\ the\ order\ of\ series\ 1\ to\ 4)$

The ACI required development length for each specimen in the study are provided in Figure 17 and Figure 18. These values were calculated based on the tested compressive strength for each given series. The calculated values are higher for the smooth epoxy coated bars because the 1.2 coating factor was applied. For purposes of the calculations, the 1.2 coating factors was not applied to the textured epoxy specimens.

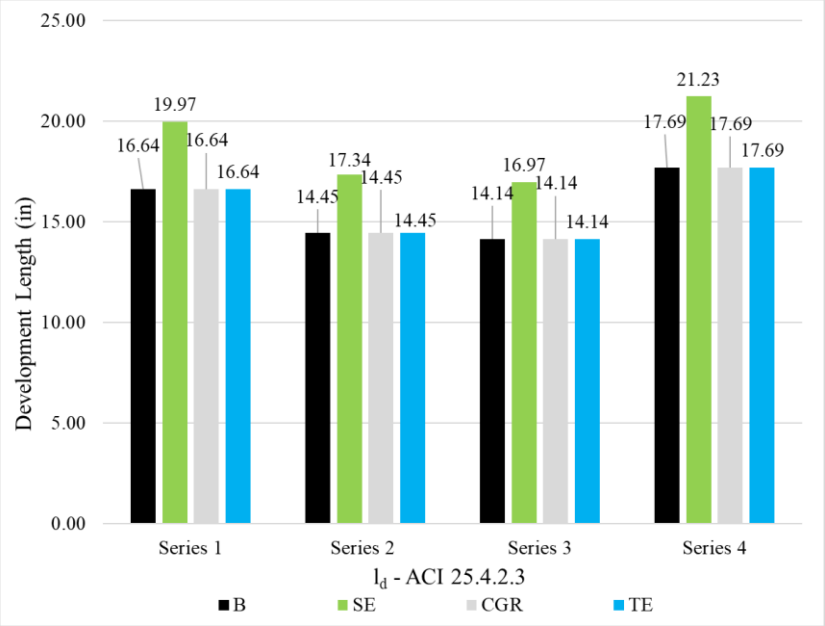

Figure 17. Theoretical development length according to ACI 25.4.2.3

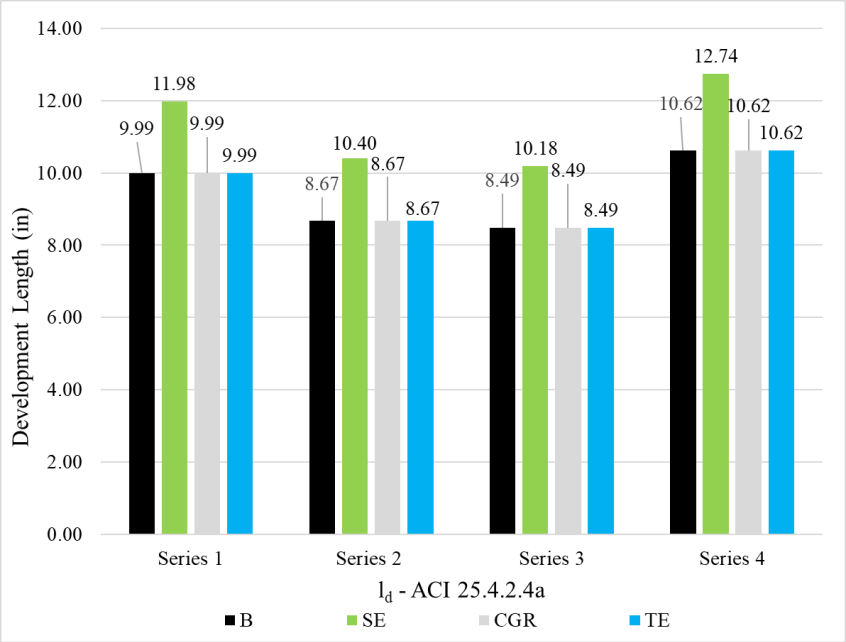

Figure 18. Theoretical development length according to ACI 25.4.2.4a. Note that these values are less than the controlling length, and that in practice the required development length would be 12 in.

The ACI-calculated development length values were conservative relative to the experimental results. All of the bars in the test specimens reached the specified yield stress or higher. Using a coating factor of 1.0 of the textured epoxy coated bars did not impact the conservatism of the ACI results.

Chapter Conclusions

What is the relative strength of concrete-reinforcement bond for alternative coated reinforcements?

Slip resistance is an indicator of steel-concrete bond strength. Stronger bond results in less slip. The experimental results show that the slip resistance offered by the TE and B bars are better than the CGR and SE. The order of slip-resistance performance is TE, B, CGR and SE. This can be attributed to the surface roughness of the bars (Figure 8) and the impact of roughness on frication. The performance of the textured bars was most notable at the 80% yield stress level, with the measured slip being only 36% to 51% of the average slip from all specimens. In contrast the smooth epoxy bars experienced 45% to 125% more slip than the average of all specimens.

How should textured-epoxy coated bars be considered in code-based requirements for development length?

The results suggest that textured epoxy coated bars have significantly different bond behavior than smooth epoxy bars. Given the test results a coating factor of 1.0 is appropriate for textured epoxy bars in the test program. However, the general

applicability of this result will require additional testing. The performance of textured epoxy coated bars having different sizes and surface roughness should be considered.

V. SHRINKAGE TESTS

Overview

This chapter addresses the question: *What is the relative impact of alternative reinforcement coatings on the control of shrinkage cracks?*

The shrinkage phenomenon in concrete members induces tensile stress if the shrinkage is restrained. Cracking will form if the tensile stress exceeds the tensile capacity. If rebar is present, the tensile stress it carries the tensile stress after cracking and prevents the crack from growing. Effectiveness of the rebar in controlling cracking depends on its bond with the surrounding concrete. Hence, restrained shrinkage tests were conducted to study the impact of bar coatings on controlling shrinkage cracks.

Test set-up

Eight series of shrinkage tests were conducted, and one specimen of each coating type was included in each series. The specimen formwork and test set-up are shown in Figure 19 and Figure 20. Mortar was cast around a steel block at the center of the specimen. The steel block was used to restrain shrinkage and create tensile stress in the mortar. A thin steel plate was placed at the center to form a weak plane in the mortar to facilitate the cracking process. The steel plate or “crack initiator” was placed on top of the steel block and the reinforcement bar passed through it. This test setup was adapted from a similar test setup used by Raoufi et al. [56].

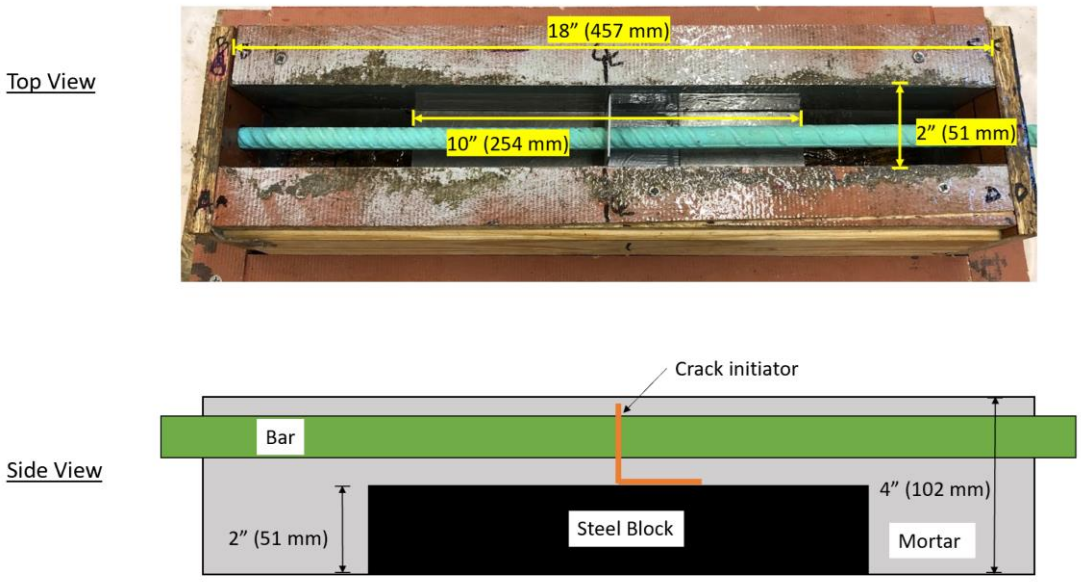

Figure 19. Shrinkage cracking specimen details

The mortar mix was prepared using a pan mixer and flow table test was conducted immediately to evaluate its consistency. A set of six mortar blocks were also cast from each batch for testing compression strength. The mortar blocks were tested 7-days after casting. The mortar mix design is reported in Table 5 and compressive strength for each batch are reported in

Table 6.

Table 5. Mortar mix design used in shrinkage tests

Mortar mix design	
Material	**Design Quantity**
Cement:Sand	1:2.25
W/C ratio	0.42
Sand moisture content	0.14%
Super Plasticizer	2.5g/1000g of cement
Flow table diameter	8.25 in – 9.5 in

Table 6. Average compression strength (7 day) of mortar used in shrinkage tests

Test Batch	**Avg. compression strength (psi)**
Batch 1	5200
Batch 2	4340
Batch 3	5170
Batch 4	5190
Batch 5	4680
Batch 6	5110
Batch 7 (14 days)	5160
Batch 8	5180

The formwork was removed approximately 2 hours after casting. To accelerate evaporation and to enhance the shrinkage and cracking, a table fan was placed to provide constant air movement over the specimens after the formwork removal (Figure 20).

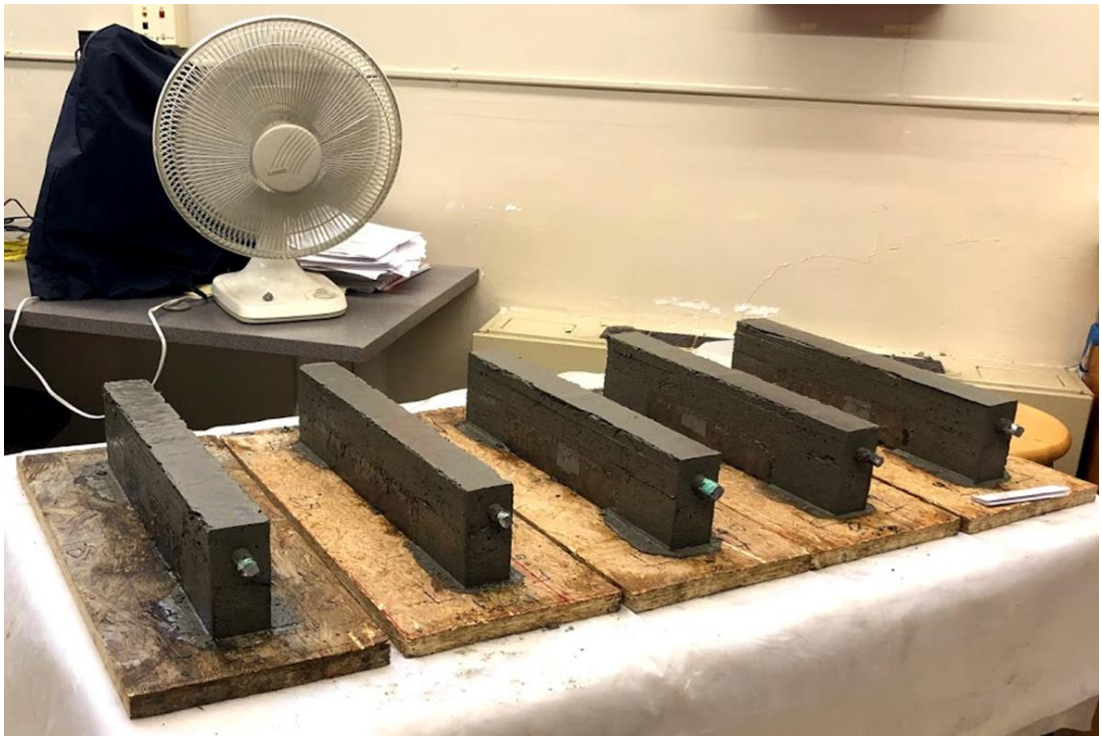

Figure 20. Shrinkage cracking test set up

Cracks were observed in all specimens and crack data were collected 24 hours after casting the mortar. Digital images of the cracks were collected in the presence of crack gauge card beside the crack for scaling, and crack width was also measured at three locations using a handheld microscope. An example crack is shown in Figure 21. Crack widths were measured from the digital images according to the procedure discussed in Chapter VIII. Crack widths were compared between the different bar types to study the effect of bar coating on the size of shrinkage cracking.

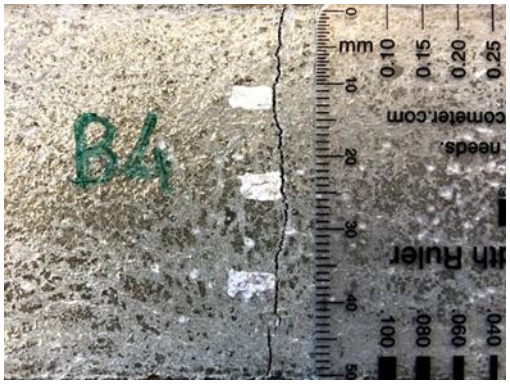

Figure 21. Shrinkage cracking in black bar specimen from series 4

Test Results

The eight series provided sufficient data to conduct statistical comparisons of the shrinkage cracking results. The analysis of variance (ANOVA) approach was used to compare crack widths between series and between coating types. Statistical comparisons in this dissertation are for the ImageJ crack area data.

The ANOVA identified statistically significant differences at both the 90% and 95% significance levels between crack areas in different series. Because the same mix design and procedures were used for each series, the inherent variability between batches is culpable in the ANOVA results. The statistically significant differences observed between batches supports the use of the comparison index to normalize test results between different series.

Statistically significant differences in crack widths for different bar coatings were not observed at the 95%, or even the 90%, confidence levels. The data in Table 7 can be used to see how closely the observed differences were to being statistically significant.

Data in the table are the ANOVA/Tukey-Kramer comparisons between the different coatings. The table values are the "absolute difference" divided by the "critical value," and can be interpreted as how close the difference was to being statistically significant at the 90% level. The highest value in the table is 0.85, which indicates that the measured differences between textured-epoxy (TE) bars and the smooth-epoxy (SE) bars were 85% of the difference needed for statistical significance. This result suggests that textured-epoxy bars have superior crack control to the smooth epoxy bars, although not to the 90% statistically significant level. This result is consistent with the trends observed throughout the test program. Specifically, the data on performance of different bar coatings has scatter, but textured epoxy bars tend to a top performer on average.

Table 7. Tukey-Kramer comparisons between coating types based on average crack width measured through ImageJ. Higher values indicate greater likelihood of difference between bars

	B	**SE**	**TE**	**HDG**	**CGR**
SE	0.21	--	--	--	--
TE	0.64	0.85	--	--	--
HDG	0.42	0.63	0.22	--	--
CGR	0.09	0.12	0.73	0.51	--

Comparison Index results are shown in Figure 22 to provide a graphical means of evaluating and interpreting the shrinkage crack data. The "box" portion of the data indicate the upper and lower quartiles of the data. The "whisker" portion shows outer quartile range of the data points. Outliers are excluded from the figure; they are defined as values higher or lower than the outer quartiles. Data in the figure come from ImageJ and microscope measurements and only three outliers were recorded in these datasets out

of 120 comparison index values. The “x” in the figure indicates the mean value and the horizontal line in the box indicates the median.

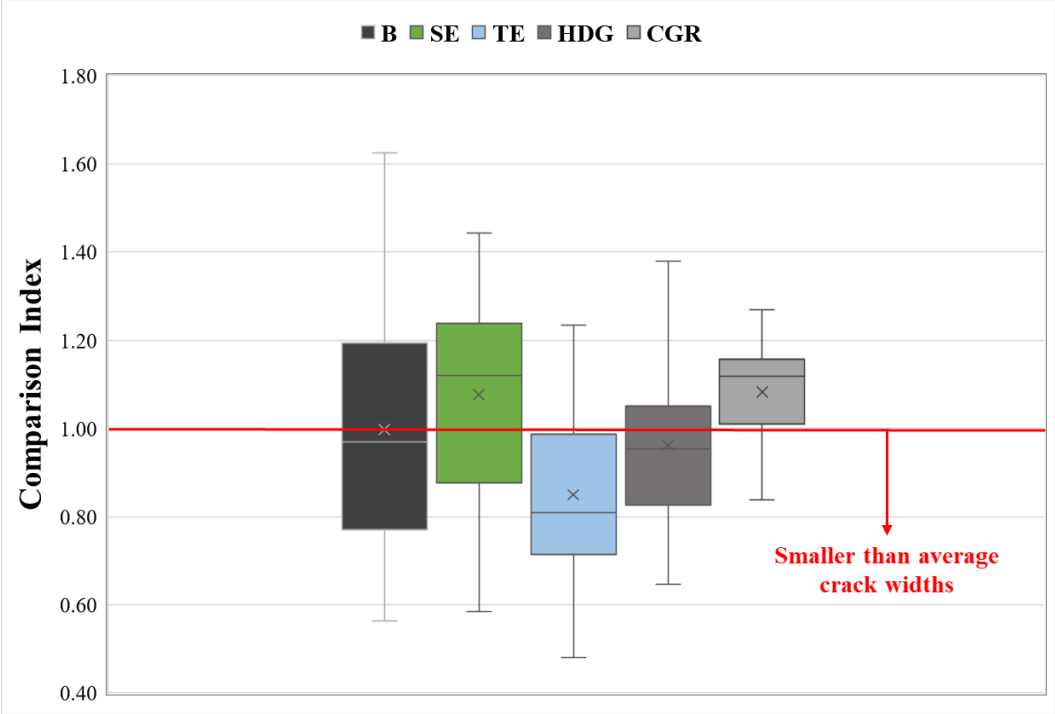

Figure 22. Comparison index of the average crack width from microscope and ImageJ, cracked area from ImageJ

The entire “box” for the textured-epoxy specimens falls below 1.0. This means that that 75% of the crack size measurements for textured-epoxy specimens were lower than the average of other bar types in comparable tests. The average comparison index for textured-epoxy bars was 0.85, indicating 15% better crack control than the average of the other bars. Hot-dipped galvanized specimens had the next best crack control with an average comparison index of 0.95. The black, continuously galvanized, and smooth-epoxy coated bars had average comparison index values of 1.02, 1.08, and 1.08, respectively.

Lessons learned for conducting shrinkage crack control tests

The test method used was developed based on Raoufi et al. [56]. It was modified through multiple iterations to arrive at the present set-up. To assist future researchers wishing to use similar methods, the following lessons learned should be considered.

Formwork removal time: It is best if the formwork is removed in transition from fresh state of mortar to hardening state. The mortar should have established its initial set and be stiff enough to support itself without the forms. Initially, the formwork was removed 8 to 10 hours after casting, however it was found that 4 hours was sufficient.

Mind humidity level: In some early attempts at the test the specimens were left to cure in a humid lab. In hindsight, it is obvious that the tests should be conducted in a dry, conditioned space. The use of a fan is advised provided it can evenly blow over all specimens.

Mind the grade marks: The test was intended to know the resistance offered by the bar against shrinkage. The action of the ribs has to be uniform and effective for all the specimens. But all the rebars have the grade marks at certain locations along its length. Hence, care was taken to cut the bar in such a way that the grade marks were not adject to the crack initiation location.

Considering longer specimens: While the specimens in this test program provided meaningful results, longer specimens are recommended. Longer specimens will have greater shrinkage strain to be "taken up" by the cracks, thus leading to bigger cracks that are easier to measure and compare. One trade-off is that longer specimens required more material and preparation. A benefit of the small specimens used here was that all

specimens and cubes could be cast from a single batch. Material availability and preparation should be weighed against specimen size.

Chapter Conclusions

What is the relative impact of alternative reinforcement coatings on the control of shrinkage cracks?

The best-to-worst average shrinkage crack control performance was TE, HDG, B, and CGR/SE (tied for worst). While the average performance trends in the shrinkage tests are consistent with other studies in this dissertation, there was no statistical difference between performance and the types of bars at the 90% confidence level. It is recommended that future research include longer and more specimens. Also, the strain measurements can be taken to evaluate the contribution of each bar type in resisting stresses due to shrinkage.

VI. PRISM TENSION TESTS

Overview

This chapter addresses the question: *To what extent (if any) does reinforcement coating impact residual crack width in concrete structures after loads have been removed?*

The impact of bar coating on the residual crack width after the unloading from different load levels has been studied. The test specimens were mortar prisms with a rebar cast at the center throughout its length. The specimens and the set-up were based on Platt and Harries [39], where similar tests were performed for titanium bars. While the type of test is similar, the focus on residual crack widths and alternative bar coatings are novel.

Test set-up

The test set-up shown in Figure 23 consisted of the specimen between two reaction blocks, hydraulic jack, anchors, and linear potentiometers. The specimen is 26" long prism with square cross-section of side 3.5" and was cast using an "off the shelf" commercial mortar mix with the #4 rebar embedded at the center along its longitudinal axis. The average 28-day tested compression strength of the mortar mix was 1700 psi. A length of rebar was left free of mortar at both the ends to pass through the end blocks, hydraulic jack, and anchors for loading. The variables in the test included all the bar

coating types (Figure 1). There were three series in total with five specimens in each (Table 1).

The end blocks were connected to the strong floor. The specimen was set within those end blocks. Steel plate spacers and a hydraulic jack were placed through the bar before loading. The whole assembly was anchored using the strand chucks on either end. Two linear potentiometers were attached one on each side of the prism at the first crack location to monitor the crack width variation for the rest of loading. All the potentiometers and the pressure gauge were connected to DAQ system to acquire the continuous data during the test.

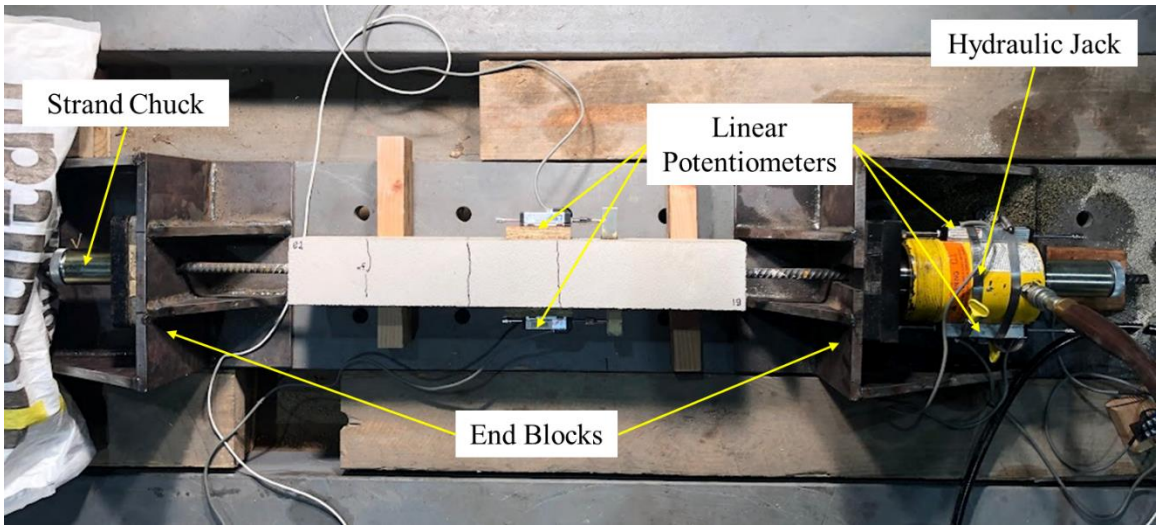

Figure 23. Prism Tension test set-up

In addition to load and displacement data, crack width data was collected at tension loads of 3, 6, 9, and 12 kip. Note that 12 kip creates a load equal to the minimum specified yield stress of the bars. Previous testing of bar samples confirmed that the actually yield stress point was higher than the tested loads.

After collected data at each load level, the load was removed, and crack width data were also collected in unloaded state. Data collection includes data from DAQ system, photos of cracks, and crack width measurements using a handheld microscope. The load stage associated with the formation of each crack was noted.

An example crack photo with labels is shown in Figure 24. Image processing was used to measure average crack with from the photos. Additionally, the crack with was measured with microscope at points that were 0.75 in. from the specimen edges. Microscope measurement points are marked with black lines in Figure 24.

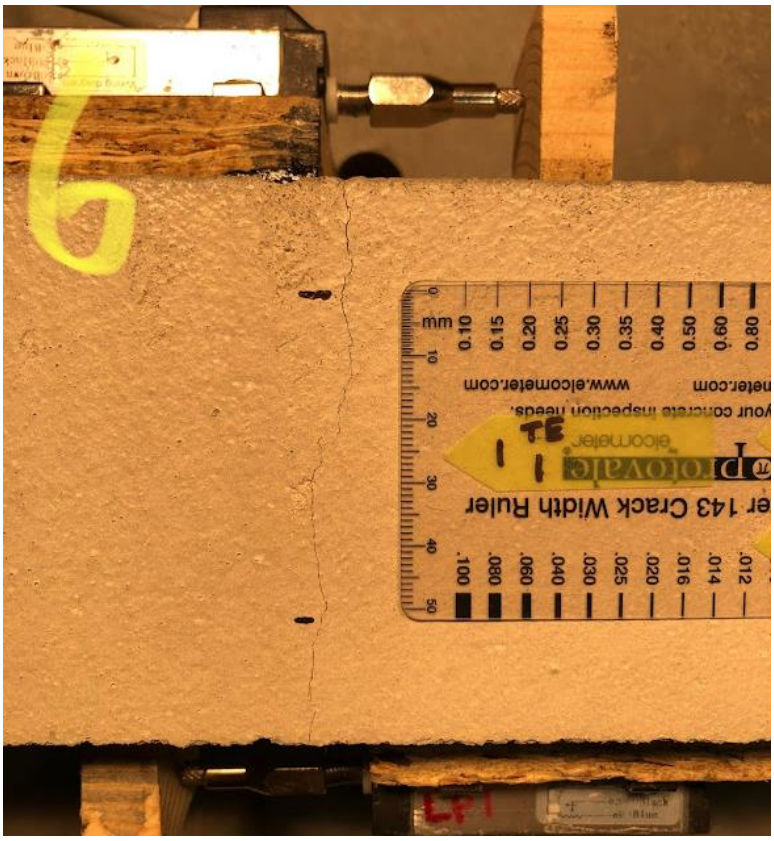

Figure 24. Crack photo of textured epoxy specimen from series 1

Test Results

Consistent with all of the other tests reported in this dissertation, the level of scatter in the data made it a challenge to interpret results and identify trends. No discernable trends were observed from average crack widths determined through image processing; however, trends can be observed in microscope data and in the number of cracks. Microscope measurements for all the specimens in each series which is shown in Figure 25. Measurements reported in the figure are the average widths from the microscope readings while the specimen was under load. At higher loads multiple cracks had formed; in these instances, with largest average crack width is reported in the figure.

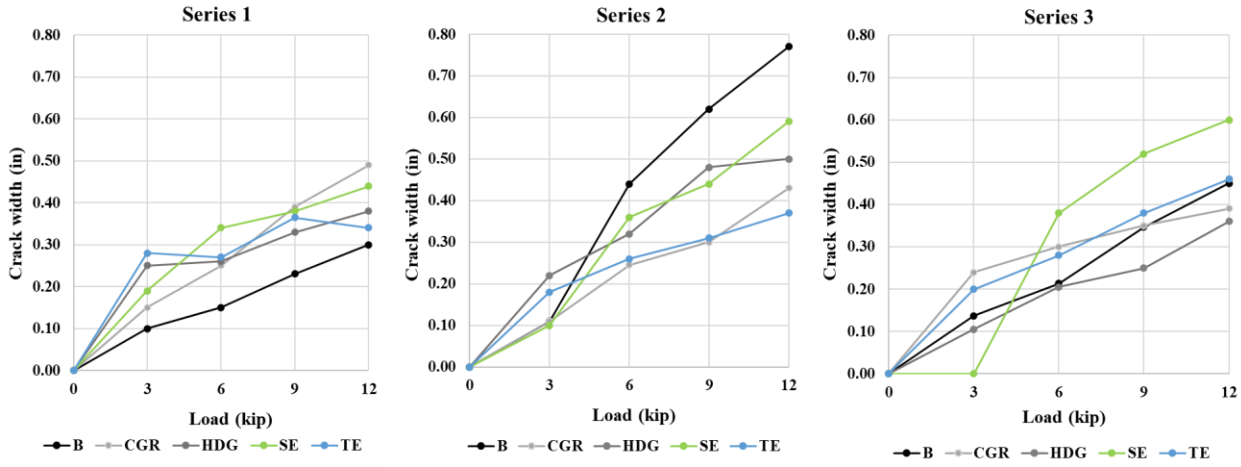

Figure 25. Crack width as a function of load level for each series. Data are from microscope measurements

As expected, the crack sizes grew as the load increased. At the 12-kip load level the smooth epoxy bars had the largest cracks in series 1 second largest cracks in series 2

and 3. This is attributed to the relatively poor bond between the smooth epoxy bars and mortar.

As stated in the research question for this chapter, the impact of bar coating on residual crack is a focus of these tests. The residual crack width data were collected and reported similar to the data from while the specimens were loaded and are shown in Figure 26. The horizontal axis in the plots shows the peak load levels to which the specimens have been loaded previously. The specimens with smooth epoxy bars had the largest residual cracks in series two and three and the second largest cracks in series one. This result is attributed to the relatively weak bond between the smooth epoxy coating and the mortar. Because the bond was weak, the specimen displacement concentrated at few cracks and larger cracks. When load was removed the larger cracks were not able to recover as much as the other specimens.

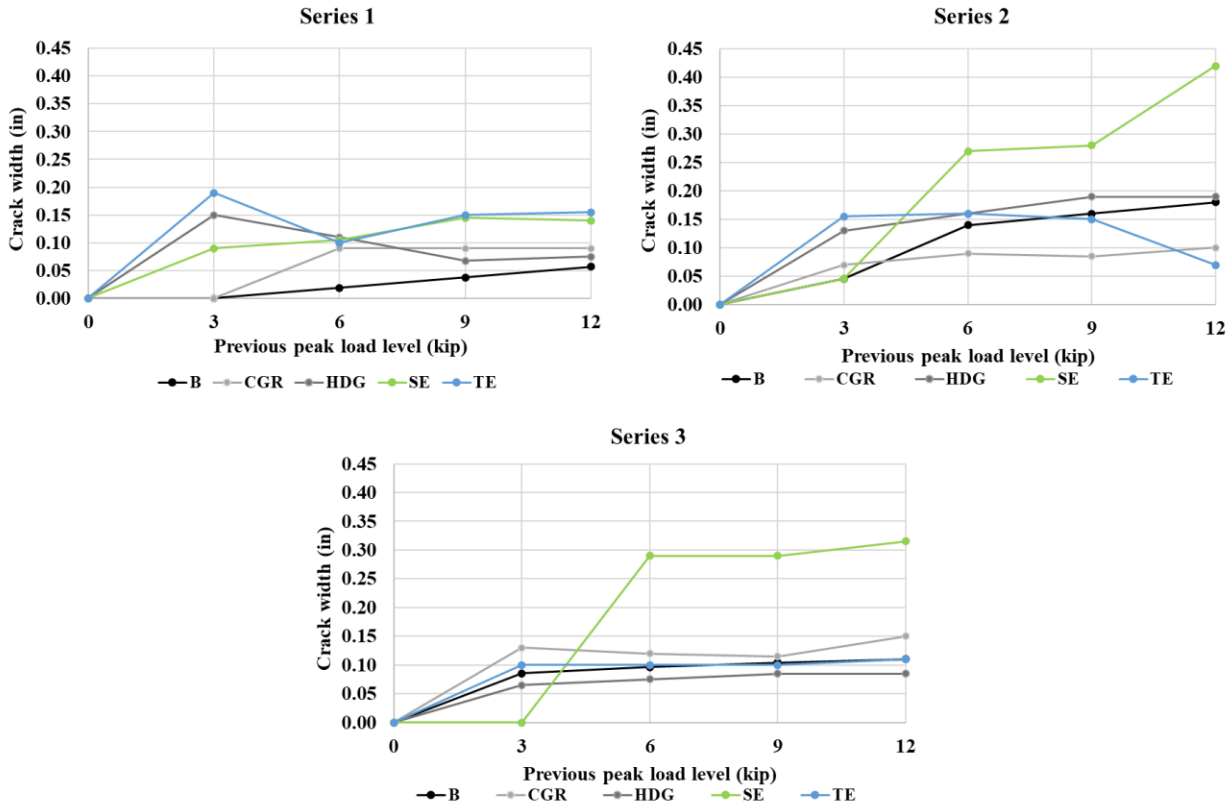

Figure 26. Residual crack as a function of previous load level for each series. Data are from microscope measurements

The crack recovery ratio was calculated for each specimen as the ratio of recovered crack width after the 12 kip load was removed to the maximum crack width at the 12 kip load level. The ratios are presented in Figure 27. While there is scatter in the individual measurements, the average crack recovery ratio suggest that smooth epoxy coatings have a different effect on recovery than the other coatings. On an average, the cracks in the smooth epoxy coated specimens only recovered 50% of their maximum width, whereas the other bars had average recovery between 70% and 80%. A possible explanation is that the weak bond between the mortar and smooth epoxy coating

experienced more damage at peak loading than did the bond in the other specimen types. Because of this damage the crack recovery was less in the smooth epoxy specimens.

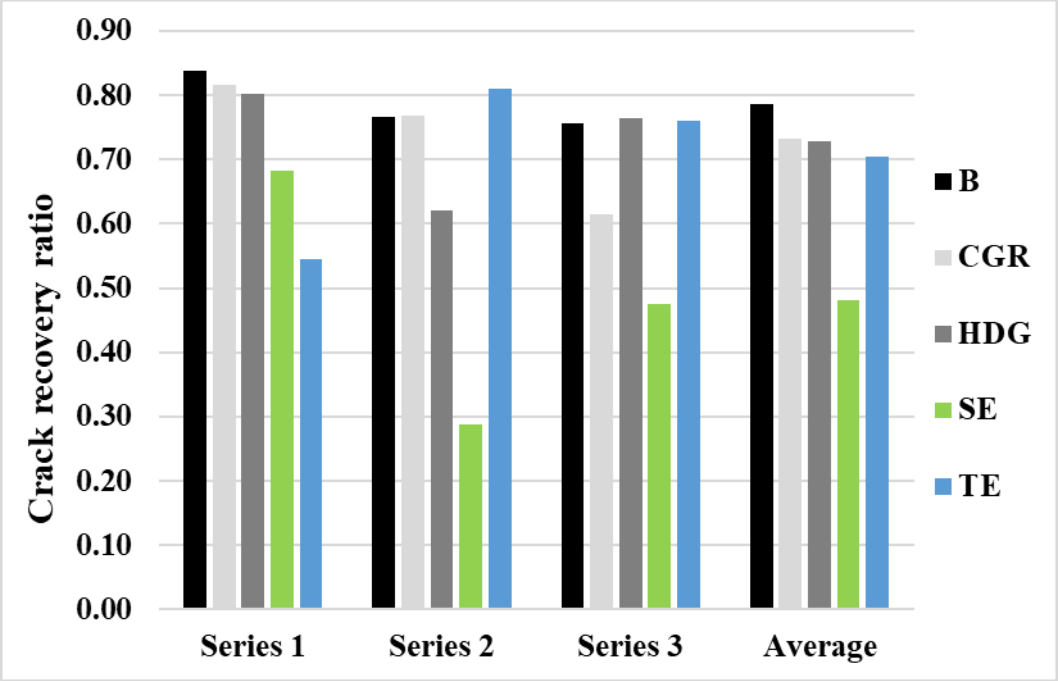

Figure 27. Crack recovery ratio for all specimens

Chapter Conclusions

To what extent (if any) does reinforcement coating impact residual crack width in concrete structures after loads have been removed?

Residual crack widths tended to be larger in specimens with smooth epoxy bars relative to the other bar types. On average the cracks width closed by approximately 50% in smooth epoxy specimens after load was removed. Cracks in specimens with the other bars closed between to 70% to 80% of their loaded width. Hence, it appears that smooth epoxy coating does impact residual crack width. A physical explanation is that the weak

bond between the mortar and smooth epoxy coating received higher levels of damage at peak loading than did the bond in the other specimen types. The damage and weak bond did not allow the bar to “grab” the mortar on either side and close the crack.

VII. ALTERNATIVE COATINGS AND REBAR-CONCRETE BOND MECHANICS

Overview

This chapter addresses the question: *Are theories of rebar-concrete bond mechanics applicable to bars with alternative coatings?*

The structural mechanics of rebar-concrete bond is well understood and is explained in many reinforced concrete textbooks e.g., [40] and [57]. This chapter contributes an investigation of bond mechanics for bars with alternative coatings.

Reinforcement-Concrete Bond Mechanics in Flexural Members

In the case of a reinforced concrete beam under flexure, there will be a variation in reinforcement tension the crack locations compared to the non-cracked part of the beam (Figure 28b). At the crack the tension force in the bar is higher. Bar tension decreases away from the crack as force is transferred to the concrete through the rebar-concrete bond. As discussed in Chapter II, bond forces are transferred through adhesion, friction, and mechanical interlock. As shown in Figure 28c, the bond force is a function of the applied shear force and the internal moment arm of the cross-section (*jd*). In constant moment regions (Figure 28d) the shear force is zero and the net result of the bond forces is also zero; however, the bond force varies within the constant moment region as shown in Figure 28g. This variation has been referred to as the “in-and-out” bond force because it switches directions between cracks [40].

The formation of cracks in RC beams is related to bond forces between the rebar and concrete. At a crack the tension in the bar is at a peak and the tension in the adjacent concrete is zero. Away from the crack the tension in the concrete increases due to the transfer of forces through the bond. Once the tension in the concrete exceeds its tension capacity then a new crack will form. As the beam approaches nominal flexural capacity numerous cracks will have formed, and the bond forces between the bar and concrete are the in-and-out forces shown in Figure 28g. Additional cracks will not form because the bond length and bond force transfer are insufficient to induce cracking-level tension in the concrete. The gradient of bond forces impacts the spacing of cracks. In situations with strong bond transfer, forces can be transferred over a short length (i.e., steep bond force gradient) and hence the cracks are more closely spaced.

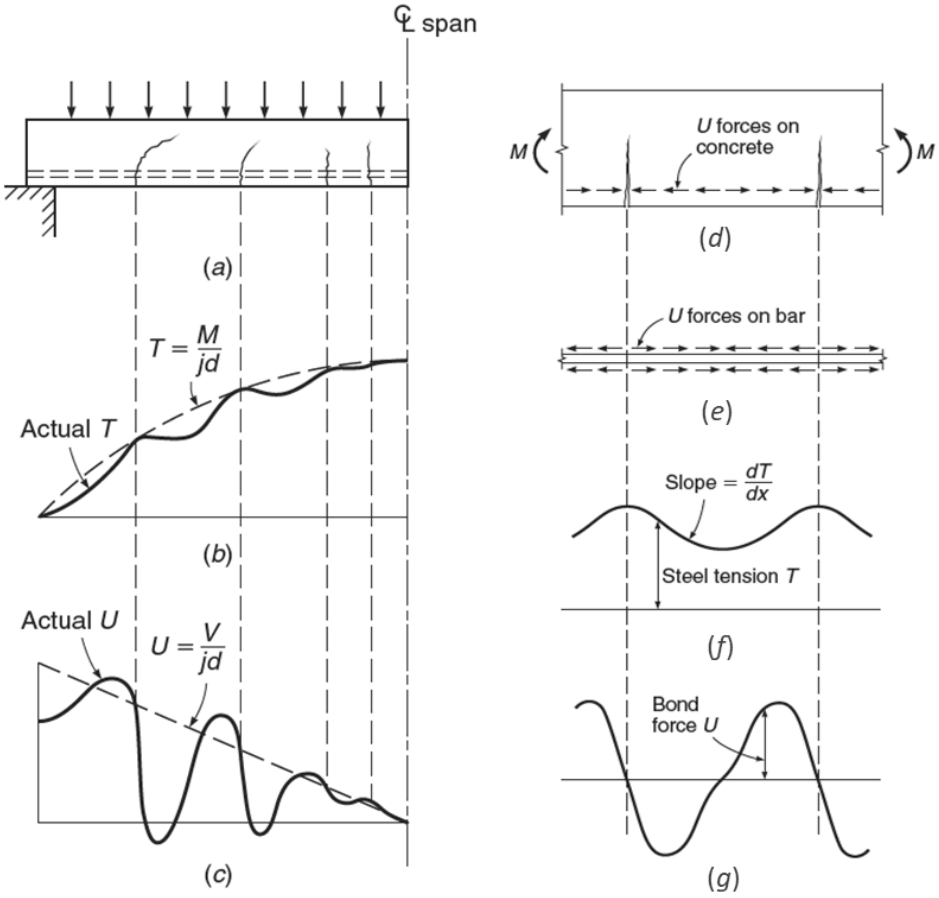

Figure 28. Variation of tensile force and bond force along the span under flexure (figure from [57])

Modelling of reinforcement-concrete bond has advanced over the decades and sophisticated models have been proposed [e.g., 58, 59]. One simple model is to consider the bond force to vary linearly from a peak at the crack to a constant value away from the cracks (Figure 29a). This is referred to as the "linear-function bond model" in this dissertation. It has also been reported that bond is damaged for a short distance adjacent to the crack over which forces are not transferred [59, 49]. A simplified model of this condition is shown in Figure 29b and is refereed as the "stepped-function bond model" for this dissertation.

Both the linear- and stepped-function models are simplifications of bar forces near cracks, and actual bar forces likely share characteristics of both the models. As described by the stepped model, there is no bond near the crack and the peak tension in the bar is constant over the debonded length. As described by the linear model, the bar force decreases over a distance as forces are transferred through bond. This behavior is shown in Figure 29c and has been discussed by Ruiz et al [59]. It has also been graphically reported, although not discussed, in the textbook by Wight and MacGregor [40].

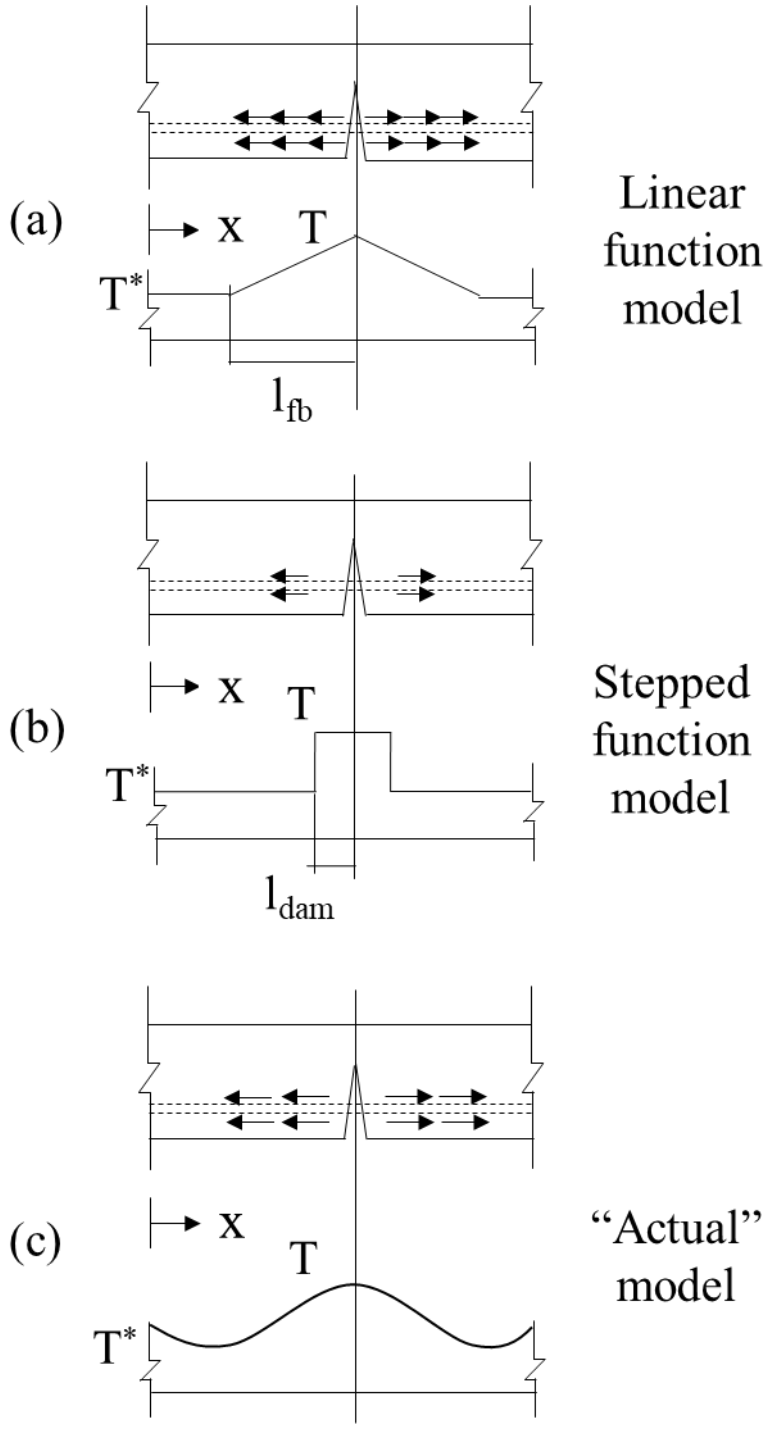

Figure 29. Different models of variation of tensile force in bar

Approach

Experimental data were analyzed to determine if the linear-function model, stepped-function model, or something in between is applicable to bars with alternative coatings. The research approach is shown in Figure 30 and is based on the concept that crack width is related to bond force transfer and crack spacing. Tension causes the bar to elongate at the crack and the length over which the bar elongates is related to bond transfer. The steps of the approach are shown in the circled numbers in the Figure 30 and are discussed below.

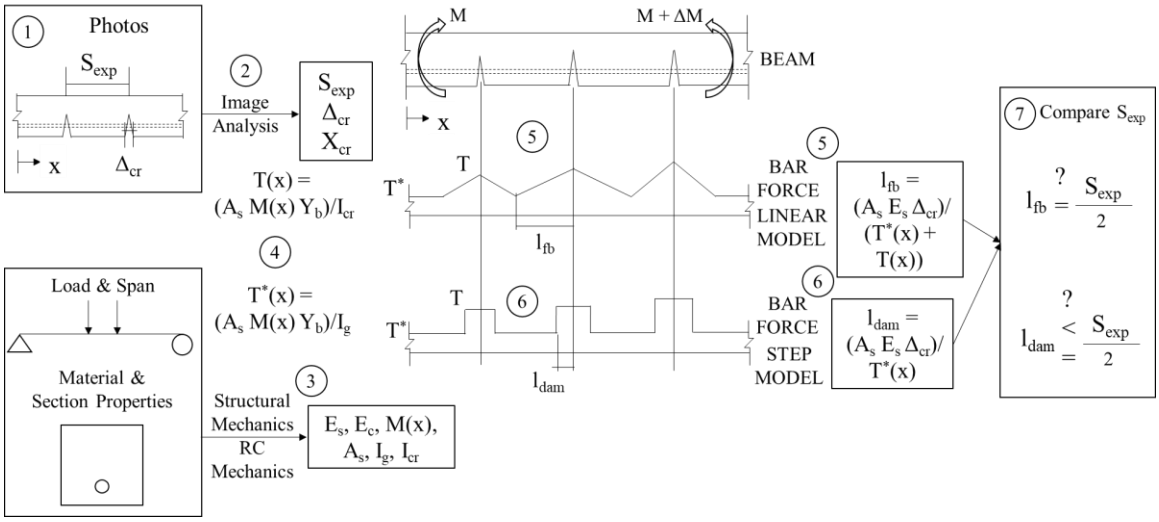

Figure 30. Procedure involved in comparison of bond lengths with the spacing of cracks. Circled numbers in the figures are the steps and are referenced in the text

Step 1. Data were taken from digital images from the experiments conducted by Murphy [2]. A diagram of the beam geometry and cross-section is shown in Figure 31. The total number of beams in the dataset was 12. The bar types included B, CGR, SE, TE, with three beams for each bar type.

Step 2. Analyze digital photos to determine position of the cracks along the length of the beams, crack widths, and spacings of cracks. The crack width was measured at the same depth as the reinforcement. Each beam had four to twelve cracks that reached the level of the reinforcement and were thus included in the analysis. Only one specimen had four cracks, the next lowest count was six. Most had eight to twelve cracks.

Step 3. Calculate the applied moment and section properties. Calculations are based on basic structural mechanics, RC mechanics, reported material properties, and beam geometry as shown in Figure 31.

Step 4. Calculate the tension force in the bar at and away from the cracks. The force was calculated as a function of position along the beam length (Equation 3 &Equation 4).

Step 5. Calculate the flexural bond length (l_{fb}) using the linear-function model. Derivation is shown in the next subsection.

Step 6. Calculate the damage length (l_{dam}) using the stepped-function model. Derivation is shown in the next subsection.

Step 7. Compare the crack spacing measured in the experiments to the calculated values from steps 5 and 6. This comparison is used to determine if the models are suitable to the bar types used in the experiment.

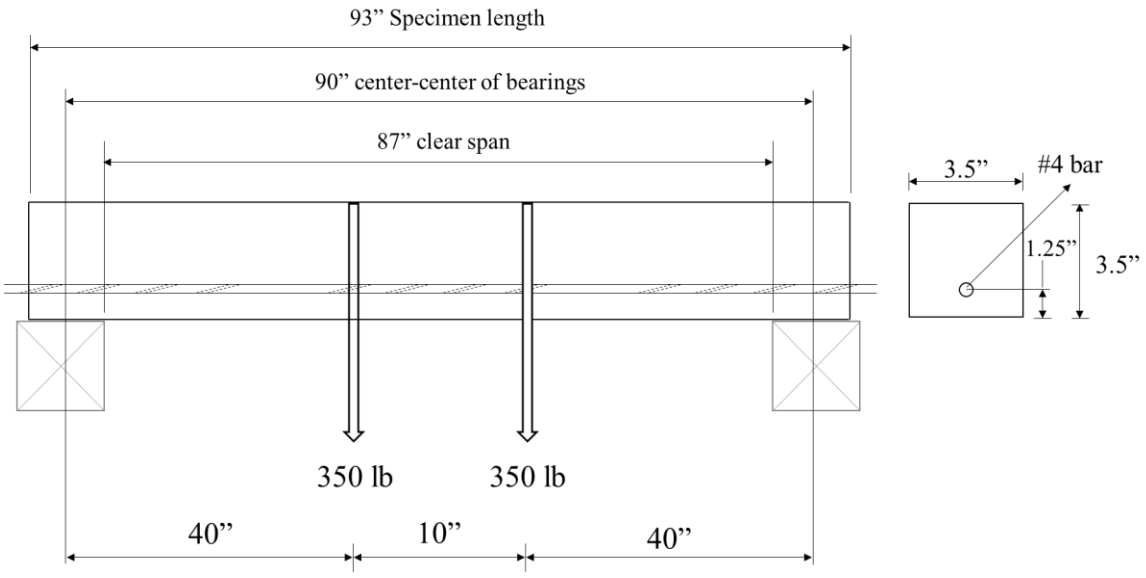

Figure 31. Beam geometry and section details from Murphy tests [2]. The dimensions reported by Murphy [2] and Ross et al. [1] were close but not exactly as shown here. Upon detailed review of specimens, photos, and lab notes, the dimensions shown here are definitive

Bond length derivation

The reinforced concrete member under flexural tension is idealized as an axial member under direct tension. The lengths l_{fb} and l_{dam} from the crack are calculated by setting the bar’s theoretical tensile elongation equal to the experimental crack width, Δ_{exp}. The experimental width in the calculations was the width measured at the depth of the bar. Derivations for l_{fb} and l_{dam} are made based on bar deformation on one side of the crack, or $\Delta_{cr} = \Delta_{exp}/2$. It is assumed that the values of l_{fb} and l_{dam} were equal on both sides of the cracks.

The equation l_{fb} will be derived first. Tension forces at the crack and away from the crack are calculated using Equation 3 and Equation 4 , respectively. The total bar tension in the flexural bond region is given in Equation 5, which models the transition of bar stresses from the peak at the crack to the constant away from cracks.

$$T(x) = \frac{A_s M(x) y_b}{I_{cr}}$$

Equation 3. Bar tension at crack locations

$$T^*(x) = \frac{A_s M(x) y_b}{I_g}$$

Equation 4. Bar tension in the uncracked sections of the beam

$$T_{total}(x) = T^* + \frac{2(T - T^*)x}{l_{fb}}$$

Equation 5. Total tension in the bar along the flexural bond length

The measured crack size is set equal to the bar elongation, which requires that the varying tension in the member (Figure 29a**Error! Reference source not found.**) is integrated over the unknown bond length from Equation 6. Rearranging Equation 6 provides an equation for the flexural bond length in Equation 7.

$$\Delta_{cr} = \frac{2}{A_s E_s} \int_0^{l_{fb}} T_{total}(x)\, dx$$

$$\Delta_{cr} = \frac{2}{A_s E_s} \int_0^{l_{fb}} (T^* + \frac{(T - T^*)x}{l_{fb}}) dx$$

$$\Delta_{cr} = \frac{l_{fb}(T + T^*)}{A_s E_s}$$

Equation 6. Crack width due to the applied Tension

$$l_{fb} = \frac{\Delta_{cr} * A_s * E_s}{(T + T^*)}$$

Equation 7. Flexural bond length from linear variation of tensile force model

The derivation of l_{dam} is directly calculated assuming that all the measure crack deformation is equal to the bar elongation that occurs over the damaged length (Figure 29b). The resulting equation for damaged length is shown in Equation 8.

$$l_{dam} = \frac{\Delta_{cr} * A_s * E_s}{T}$$

Equation 8. Length of damage from the crack using a stepped function model

Results and Discussion

The calculated bond length and the damage length for each bar type from the models were compared with half the average spacing ($S_{exp}/2$) of the cracks. Comparisons are shown in Figure 32 and Figure 33, wherein the given values are the average spacing or the average calculated parameter in the associated beam and series. In linear-function bond model, the spacing of the cracks is theoretically equal to two times the flexural bond length (Figure 29a). In the stepped function bond model, the spacing of the cracks theoretically should be greater than twice the damaged length (Figure 29b). Hence, the spacing parameter ($S_{exp}/2$) should be close to l_{fb} and should be greater than

l_{dam}. If the spacing parameter falls between l_{fb} and l_{dam}, then experimental bond transfer is bracketed by the assumptions of the linear- and stepped-function models (i.e., Figure 29c).

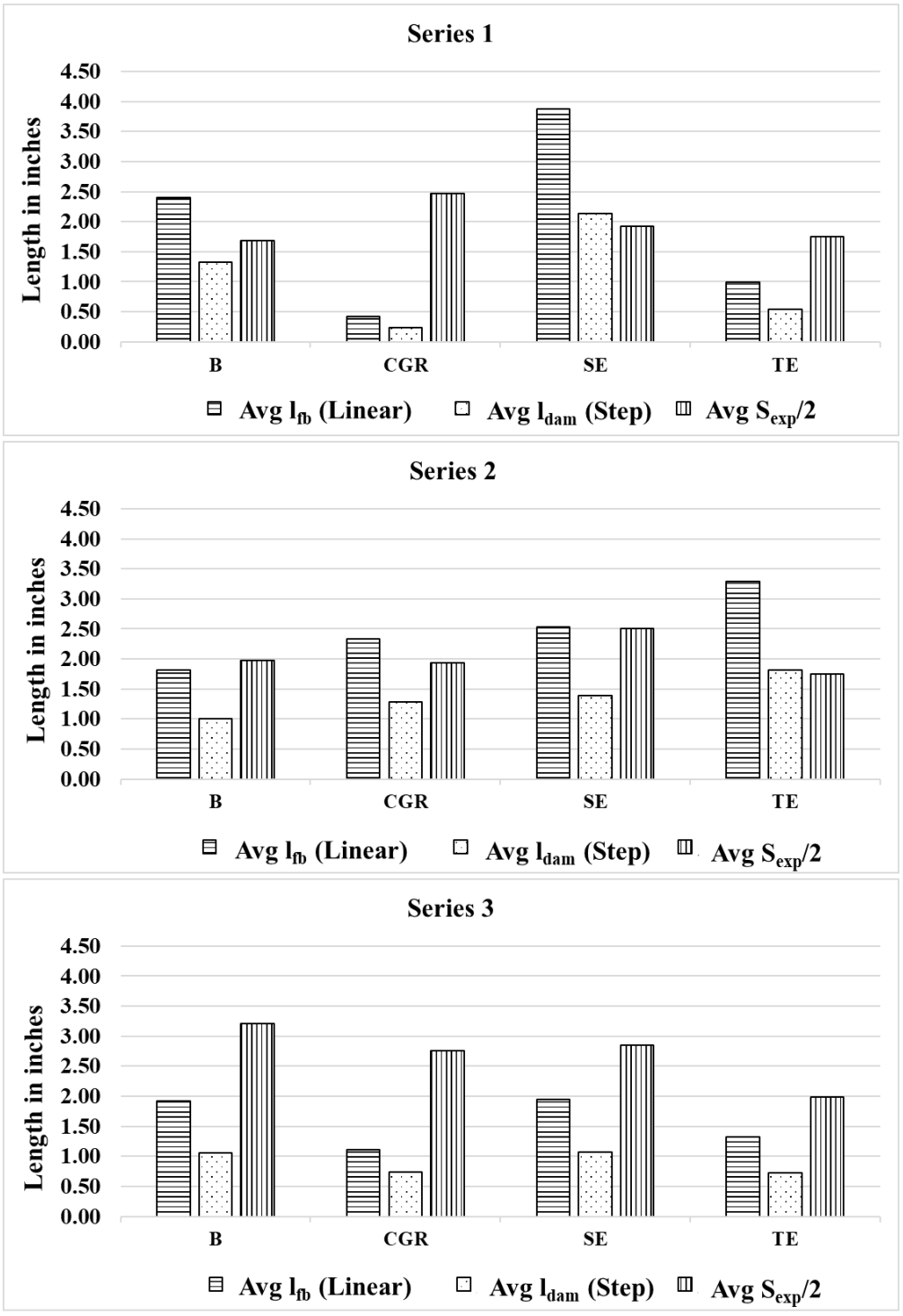

Figure 32. Comparison of flexural bond length and damaged length with crack spacing parameter in each series

It can be seen that the experimental and theoretical comparisons from any given series and bar type are variable relative to the calculated comparison values. This result is due to the randomness of the cracking phenomena in concrete. For this reason, it is not viable to make conclusions based on a single beam or series.

The CGR specimen for series 1 deserves specific attention. This specimen had many cracks that did not extend up to the level of the reinforcement. Because they did not engage the bar, these cracks were omitted from the analysis. This accounts for the large spacing of cracks in the specimen. In other specimens it was rare to have a crack that did not extend to the reinforcement level. Based on the situation of the CGR specimen in series 1, it was considered an outlier and was excluded from further analyses.

Figure 33 combines the results from all series and reports them as averages. Evaluating the results as averages across multiple cracks and specimens clears some of the scatter and allows for observation of trends. For the B, SE, and TE specimens the average crack spacing parameter was between the flexural bond length and the damaged length. Thus, on average, the behavior of these bar types was bracketed the linear- and stepped-function models. It is inferred that a small portion of the bar is debonded near the crack and that the bond forces are transferred gradually at locations beyond the debonding.

CGR from series 1 was not included in Figure 33. Even with this removal, the average results from the CGR specimens are not aligned with the bond models. This may be due small sample size and to the random nature of concrete cracking and bar-concrete bond. It may also be due to a difference in bond mechanics behavior for CGR bars.

However, based on the available data, no conclusions are made about the bond models and CGR coating.

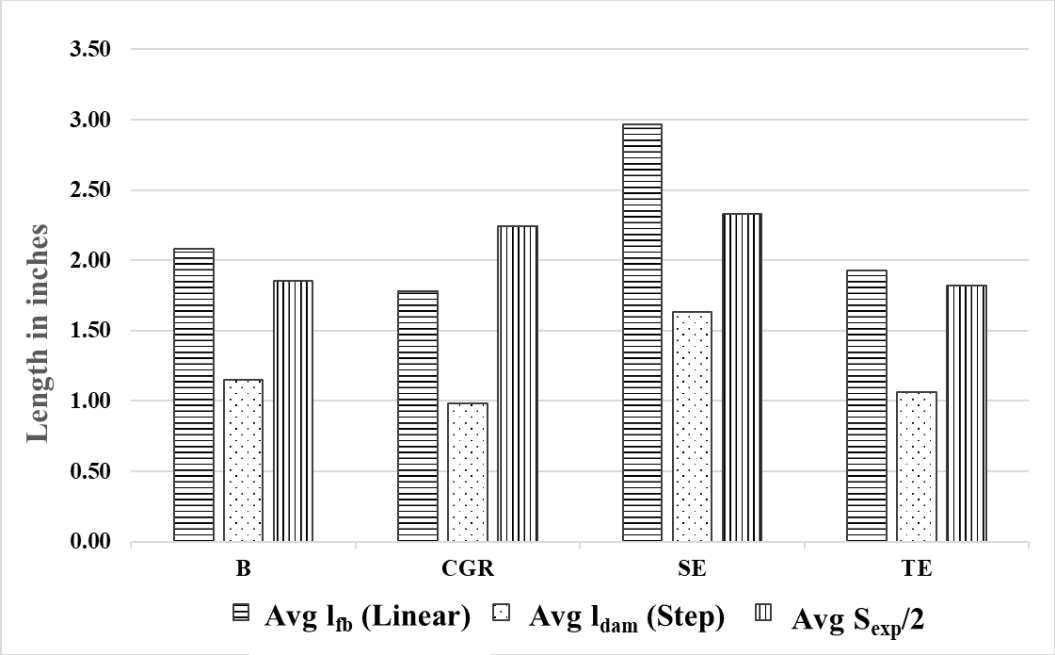

Figure 33. Comparison of bond and damage length with crack spacing parameter in all the series combined

Chapter Conclusions

Are theories of rebar-concrete bond mechanics applicable to bars with alternative coatings?

Two theories (models) were considered. First was a linear-function bond model based on gradual force transfer over a length adjacent to a crack. Second was a stepped-function model based on a debonded length adjacent to the crack and immediate force transfer after the debonded length. Considering the results presented, the bond transfer

behavior is bracketed by the models for the smooth, textured, and uncoated bars. Due to randomness in the data and limited data points, the results are inconclusive for the continuously galvanized rebar.

VIII. FIELD STUDY PAPER

This chapter is based on manuscript under final review in the ASCE Practice Periodical of Structural Design and Construction.

The research was performed by the dissertation author with assistance from Dr. Taylor Sorensen. The work was overseen by Dr. Brandon Ross and Dr. Amir Poursaee.

Abstract

Cracking in concrete structures is a ubiquitous problem and affects the serviceability of such structures. In many cases, it is imperative to properly measure and monitor the crack size to identify locations for repair and rehabilitation. This paper describes two field studies that used digital image processing to measure the width of cracks in concrete structures. The first field study compared crack measurements from digital image processing, a handheld microscope, and a crack gauge card. In the second field study, digital image processing was used to measure end region cracks in precast pretensioned concrete girders. Guidance is provided for engineers who wish to use digital image processing in field studies. Conditions, where digital image processing may lead to errors, are identified, and limitations of the methods are discussed. In general, the studies demonstrate that image processing methods can efficiently and measure the size of cracks in concrete structures in field settings, and that image-based measurements are comparable to microscope measurements.

Introduction

Cracks in concrete structures can affect their durability and load carrying capacity. Hence collecting information about crack width is important for inspection and diagnosis of damage in such structures. Traditionally, the crack width measurements are carried out using a crack comparator (i.e., gauge card) or handheld microscope (Figure 34). These devices have discrete scales, and the operator must choose which line on a crack comparator or which demarcation on a microscope best represents the crack width. Microscope measurements also have the disadvantage of being time consuming. Furthermore, crack width varies along the length of the crack, which requires several measurements. Digital image processing offers an alternative means of evaluating cracks that is objective, more precise, and more efficient compared to the conventional methods.

Figure 34. Crack gauge card and the handheld microscope

Digital image processing is a well-established methodology that has previously been used to measure cracking in concrete (e.g., [60-64]). In contrast to the prior studies that established and advanced the science of image processing, the current paper aims to

provide practical guidance for engineers who wish to use image processing to measure concrete cracks in field studies. This paper describes a comparative field study wherein measurements taken through digital image processing were compared to measurements taken by a crack gauge card and a handheld microscope. A second field study investigated cracks at the ends of 8 precast pretensioned concrete girders. The girder study evaluated the effect (if any) of different rebar types on end region cracking. A phone camera with a resolution of 12 megapixels was used to capture digital images of the cracks, and the open-source software ImageJ [65] was used to analyze the images and measure the crack widths.

The main objectives of this paper are to:

1. Provide practical guidance for using digital image processing to measure concrete crack widths in field settings.
2. Compare gauge cards, microscopes, and image processing methods for measuring concrete crack widths in field settings.
3. Demonstrate the use of image processing measurements in a field study of cracking in precast-pretensioned concrete girders.

Background

Image Processing. Digital image processing methods were developed in the 1960s for satellite imagery and medical imaging ([66] and [67]). However, due to the high cost, digital image processing was not widely applied to other disciplines and industries until the 1990s, when low-cost personal computers and digital cameras became

widely available [68]. Since then, digital image processing techniques have been adapted to many applications and disciplines, including civil engineering. For example, image processing has been used to detect moving vehicles [69], evaluate surface cracks in pavements [60], assess fire-damaged mortar [70], measure strain distribution during testing of geosynthetic materials [71], and to classify steel bridge coatings [72]. Specific to concrete structures and materials, digital image processing has been used to evaluate shapes of aggregates [73], assess the microstructure of mortars [74], identify air voids and aggregate content in concrete [75], measure chloride diffusion in concrete [76], and determine the distribution of fibers in concrete [77]. Recent advances in digital image processing applications for bridge engineering include 3D image-based diagnostics during bridge repair [78] and in-service measurements of deflections in an off-shore bridge [79].

Image scaling and crack isolation are the two critical components of digital image crack measurements. Scaling is accomplished by placing a reference item of known dimension within the digital image. Processing software simply divides the known length by its associated number of pixels to establish a length-to-pixel scale. Identifying and isolating cracks in an image is accomplished using filters that distinguish between light and dark pixels. Cracks are commonly darker in digital images allowing conversion of the image to a binary field with black pixels at the cracks and white pixels at other locations. The division of the pixels in an image is called binarization which uses thresholding techniques (Singh et al., 2011 [80], Singh et al., 2012 [81] and Firdousi and Parveen, 2014 [82]). The Otsu approach (named for the developer, Otsu (1979)) is

commonly used to create such binary fields for processing. The current paper used the Otsu approach embedded in the ImageJ software.

The recent work by Rahman et al., (2019) [83] used image processing to measure and evaluate concrete cracking, albeit in a laboratory setting. They used 2D digital images to analyze cracks in axially loaded reinforced concrete specimens. The specimens consisted of concrete prisms with a concentrically placed rebar extending from both ends. A tensile force was applied to the rebar to induce cracking in the concrete. Images of the tensile cracks were collected at various load levels. Crack width measurements from image processing were compared to manually collected data from microscope measurements. The results were comparable, and it was concluded that the image processing approach was viable for measuring concrete cracks. The current paper extends the work by Rahman et al. [83] by demonstrating the practice of digital image processing to measure concrete crack widths in field studies.

A semi-automatic process of measuring concrete cracks was proposed (Barkavi and Natarajan, 2019) [84] using an algorithm in MATLAB. Image processing was used to obtain both the crack length and width and it was verified with the results of past literary works. In the current paper, a similar outline of the process has been adopted but with ImageJ software.

End Region Cracks in Precast-Pretensioned Girders. A brief discussion on end region cracking is given here to provide context for the precast girder field study. End region cracks have been a subject for research ever since the widespread use of precast-pretensioned girders began in the 1960s (Gergley and Sozen, 1963 [85]; Marshall

and Mattock, 1962 [86]; Gamble, 2014 [87]). The topic is of continued interest to transportation agencies that have funded multiple research studies on end region cracking in recent years (e.g. [21-23]). Some precast industry professionals have reported that end region cracks form in more than 80% of girders [88].

End region cracks form as prestressing forces originating in the bottom flange are distributed to the rest of the cross section (Figure 35). Distributing the prestressing force from strand to the girder end creates tensile stresses that lead to cracks in the web and flange (Figure 36). Cracks in the end region can compromise durability and can negatively impact shear strength when compounded with other issues [89].

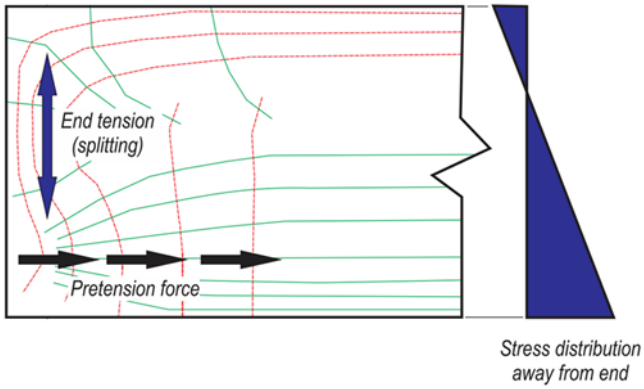

Figure 35. End region cracks form due to tensile stresses (green trajectory lines), which form as the pretension force is distributed from the bottom flange to the rest of the cross section [25]

Figure 36. End region cracks in one of the girders from the field study. Lines are marked adjacent to each crack in the photo for emphasis.

Measuring and monitoring end region cracks can be time consuming. A previous field study used a handheld microscope to measure and track end region cracks in multiple girders [27]. Widths were measured along each crack, and changes in the crack lengths and widths were monitored over four months. The measurements were time consuming and only resulted in point measurements at discrete locations. The current paper was motivated by providing a more efficient and data-rich method for measuring and monitoring cracks.

Crack Width Measurements Using Digital Images and ImageJ

Cracking in the field studies of this paper was documented with several photographs, each of which included a crack width gauge card for a size reference (Figure 37). Image processing of cracks in the photographs was performed using ImageJ, an open-source image analysis software [65]. Its several features, such as ease of use, recordable macro language, and extensible plugin architecture, make ImageJ a popular platform used by researchers who are non-programmers, amateur programmers, and professional developers alike. Image processing can quickly determine crack dimensions such as width and length based on a digital photograph. The essence of analyzing images of cracks is calculating the area of a crack in pixels, converting pixel area to physical area, and then estimating an average crack width by dividing that area by the length of the crack. The procedure below outlines the process used to analyze a single crack in an image.

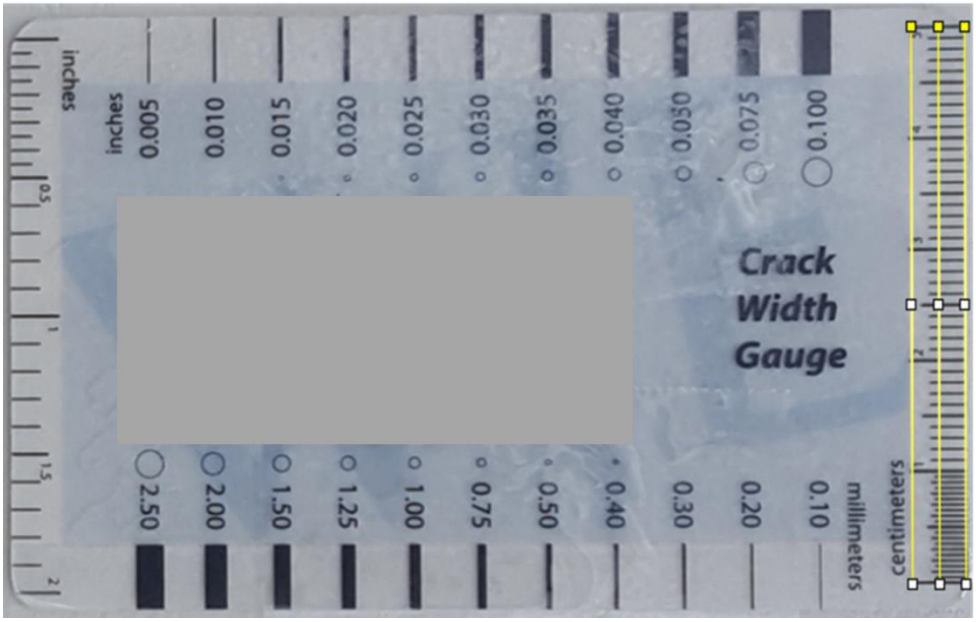

Figure 37. The three measurement locations (vertical lines drawn at the right edge of the image) on crack gauge card to set scale for image processing

For a given crack, a clean and clear image was first selected and opened in the ImageJ software. It was then necessary to set the scale for reference using an object of known length. A crack gauge card was used for this purpose in the current study (Figure 37). Three reference lengths were placed on the 50-mm scale on the gauge card. Each reference length returned an associated number of pixels. The average number of pixels from the three lengths was used to determine the scale. For example, if the average measurement across the 50-mm length was 256.3 pixels, then the scale was approximately 5.126 pixels/mm for the image. This scaling was saved for future reference. A separate scaling was taken for each digital image.

With scaling in place, the crack segment could then be selected. It was preferred to analyze the entire crack as a whole (Figure 38), but as the image processing approach relied on the contrast between the crack and the surrounding concrete girder, it was sometimes necessary to divide the cracks into smaller image segments for analysis. This occurred when the image included shading due to light variations, texturing, or varying colors in the concrete material across girder's length. In cases when the cracks were emphasized using a marker (e.g., Figure 36), the image was cropped to remove the marking. Once the crack portion was selected, a duplicate image was created where the image type was converted to an 8-bit image to reduce the number of hues present and increase the distinction and disparity between crack and the background color (Figure 39a). The image threshold was then adjusted to create a purely black and white image to display only the crack (Figure 39b).

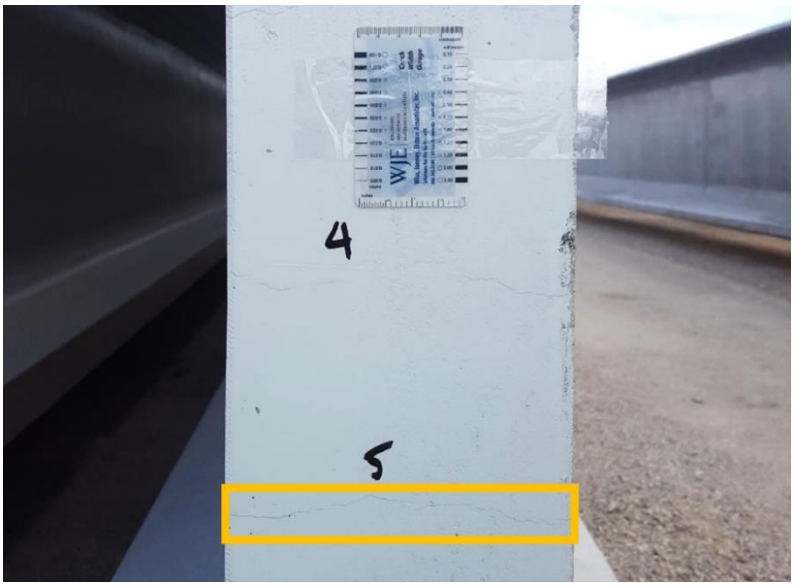

Figure 38. Cracks and gauge card on girder end. The boxed area contained a crack and was cropped out of the photo for image processing. Cracks are difficult to see in this photo but were obvious after zooming in on the digital image

Figure 39. Crack segment analysis: a) duplicate of crack segment selection, and b) isolated crack after 8-bit conversion and threshold adjustment of a crack segment

Theoretically, only the crack's pixels would be displayed after the threshold was set. For this reason, the contrast of the image is key to defining the crack area in an image. The noise present in the image can be reduced using the threshold type selected in the threshold tool. ImageJ offers various threshold types to choose from, including Intermodes, Minimum, and Otsu. Once the 8-bit image is created and the threshold option

is selected, the threshold should be adjusted. It means that the pixels above or below a particular threshold value should be identified. ImageJ allows defining both low and high threshold values so that only pixels falling within a specified range are found. This improves the crack identification, particularly when it is not very clear in the image. However, the threshold should be chosen carefully to reduce the noise in the image.

Shadows or other dark areas within an image present can be obstacles to obtaining an accurate measure of a crack area that cannot be circumvented by only modifying the threshold. This issue is demonstrated in Figure 40. In the girder case study, black permanent marker or paint was used to label cracks and girder numbers. Changing the threshold affected which parts of the crack were retained as black pixels, however. Figure 40 shows how the threshold tool was insufficient to remove girder paint, permanent marker, and background as black pixels. When dark could not be cropped out of a crack image, it was necessary to manually remove them by "painting over them" with white pixels, thereby defining them as areas that are not part of the crack. Various pre- and post-processing methods are available using commercially available software to paint over dark areas. ImageJ includes a paintbrush tool plugin to easily achieve this purpose, which was the option used in this study. Figure 41 shows the final image used to analyze the crack from Figure 40 after removing the respective dark portions of the photo by using the ImageJ paintbrush tool. If possible, markings near the crack on the concrete surface should be avoided when selecting portions of the crack to reduce the amount of manual editing required.

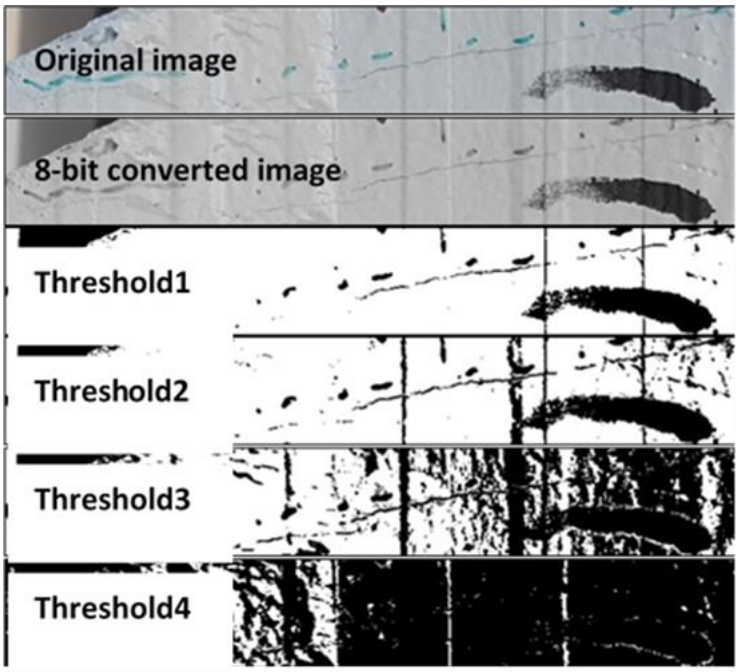

Figure 40. Effect of using different threshold selection on isolating a crack in an image

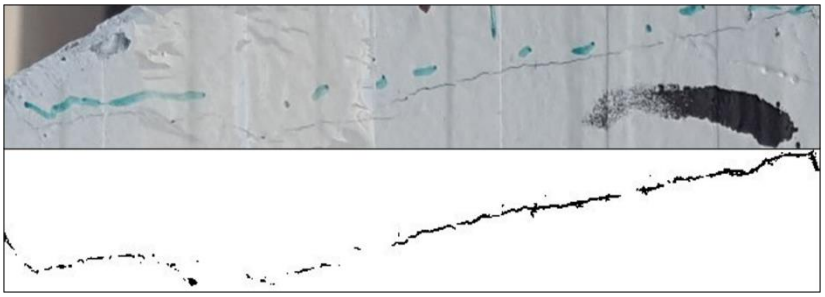

Figure 41. Original and final image after removing dark portions of the image due to marker, paint, and background

Although the visual image in Figure 41 may seem to indicate that the crack is continuous, the processed image displays discontinuities in the crack. These are due to variations in light and color, such that even with modifications of the threshold, the crack cannot be distinguished from the concrete. This means there will be an inherent amount

of uncertainty introduced based on several variables, resulting in either an overestimate or underestimate of crack width. In the case of Figure 41, the discontinuities could potentially reduce the crack area, leading to a potentially underestimated width. Even upon closer visual inspection of the crack image shown in Figure 41, however, there are portions of the crack that are still not easily discernable without the context of adjacent crack segments. As the crack area in question is of such small length and width, the assumption is that these small discontinuities are insignificant and of themselves will not have great influence on the end results. In addition, there are other occasional pixels that are not part of the crack but that are included in the image; to eliminate all stray pixels would be time-intensive and unnecessary. These variable effects tend to balance out, for which reason use of the average crack width is of paramount importance in this study. The first case study presented in this paper indirectly addresses this issue by comparing average width measurements from image processing with minimum and maximum measurements from other methods. Once the threshold was set, and the image was modified to only include the crack, the image was saved, and a "particle analysis" was performed to determine the remaining area. In this automated process, the pixels associated with the crack are counted, and the previously established scaling is used to convert the pixel count to a surface area. To estimate the average crack width, the total crack area was then divided by the length of the crack. The entire process involved in image processing as explained is also summarized and shown in Figure 42 and Figure 43.

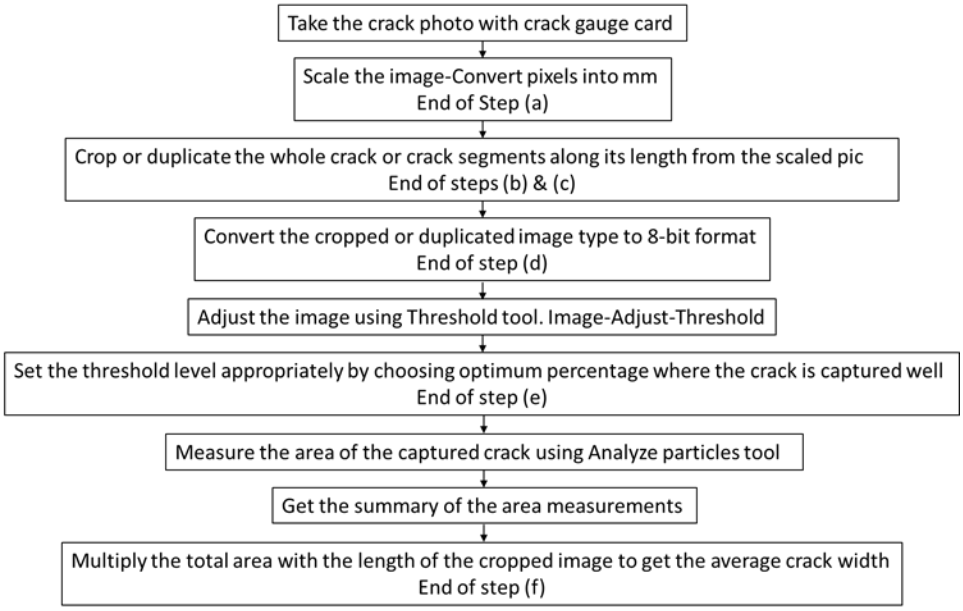

Figure 42. Flowchart depicting the ImageJ procedure in steps (a) through (f)

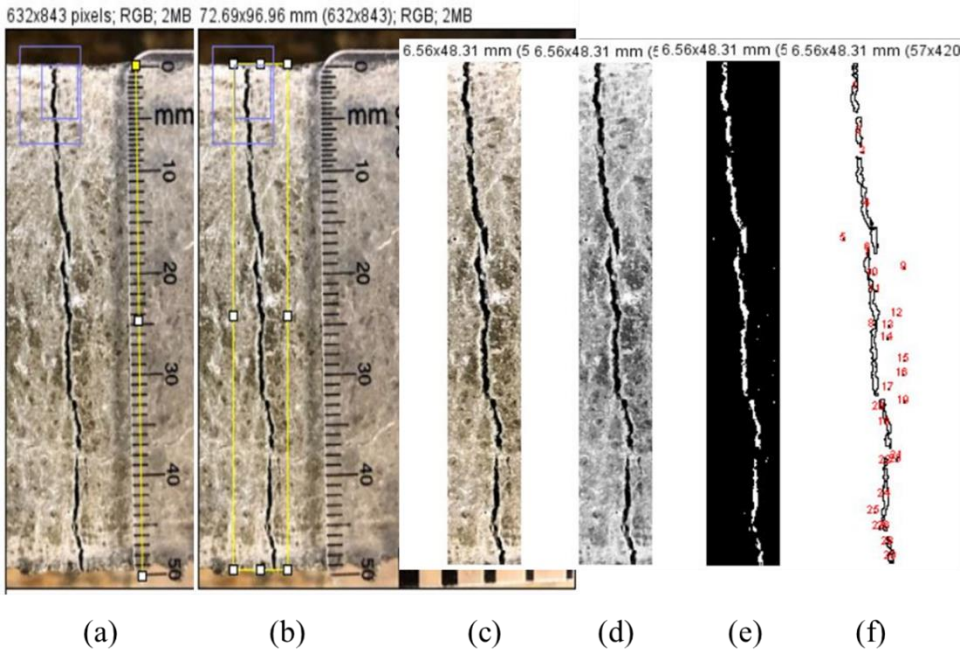

Figure 43. Graphical representation of the ImageJ procedure in steps (a) through (f)

While image processing using ImageJ software has many benefits, there are a few potential challenges in its application to crack measurement. Some surfaces require a trial-and-error process to optimize the threshold using the built-in threshold filters. This requires subtle manual adjustments in order to better differentiate the cracked area. The process to edit a crack photo could also become quite time-consuming and labor-intensive in cases where there is a lot of noise around the crack.

The method presented in this paper measures the average crack length at a given time. In some cases, the standard deviation of crack width could be of interest; unfortunately, the ImageJ software does not readily provide the information necessary to calculate standard deviation. Another topic of interest could be growth of the crack in length of width over time. This was not considered in the current paper, however, the basic approach and software discussed here could be extended to analyze changes in cracks over time.

Field Study One: Comparison of Gauge Card, Microscope, and Image-Based Measurements

A field study was conducted to compare measurements made using a crack gauge card, a handheld microscope, and image processing using the ImageJ software. The study considered concrete cracks in structures on the Clemson University campus. Cracks were selected to have a range of widths from approximately 0.01 mm to 1.5 mm. Crack images were all from smooth concrete surfaces (having less texture than a "broom" finish).

The microscope and gauge cards were used to take measurements at discrete locations. In contrast, the image processing approach measured the average width across the length of a crack. To facilitate comparison between the different methods, minimum and maximum widths from the gauge card and microscope were compared to the average widths from image processing. It is reasoned that the average measures made using image processing should fall within the range of discrete values from the other methods.

Minimum and maximum widths from the gauge card and microscope were taken by visually scanning the crack and measuring locations that appeared the widest and narrowest. Because the image analysis used an average width of the entire crack whereas the microscope only measured 3 discrete points, the results showed some variation. The study showed, however, that the crack widths from image analysis are in the range of the measurements taken with the microscope.

lists crack width measurements from each of the three different methods. For presentation purposes, all numbers in the table are rounded to two decimal points. The precision of the measurements varied depending on the instrument used and the size of a crack. The crack gauge card has a precision of 0.10 mm, whereas it is 0.02 mm in the case of microscope and 0.001 mm in the case of ImageJ.

Table 8. Maximum and minimum crack width measurements according to different methods

Crack ID	Gauge card (mm)		Microscope (mm)		Image analysis (mm)
	Minimum	Maximum	Minimum	Maximum	Average
Crack 1	0.30	0.40	0.40	0.50	0.48
Crack 2	0.40	1.00	0.90	1.20	0.97
Crack 3	0.35	0.40	0.40	0.80	0.69
Crack 4	0.20	0.60	0.20	0.60	0.29
Crack 5	0.10	0.10	0.10	0.20	0.18
Crack 6	0.15	0.25	0.10	0.40	0.34

Normalized crack width measurements are compared in Figure 44. Values were normalized by dividing each crack by its respective average crack width from the digital image analyses. For example, the maximum microscope reading for crack 1 was 0.50 mm, and the average image analysis measurement was 0.48 mm; hence the normalized value for measurement is 1.04 (0.50 mm/0.48 mm). Normalized measurements greater than 1.0 are wider, and normalized measurements less than 1.0 are narrower than the image analysis measurement.

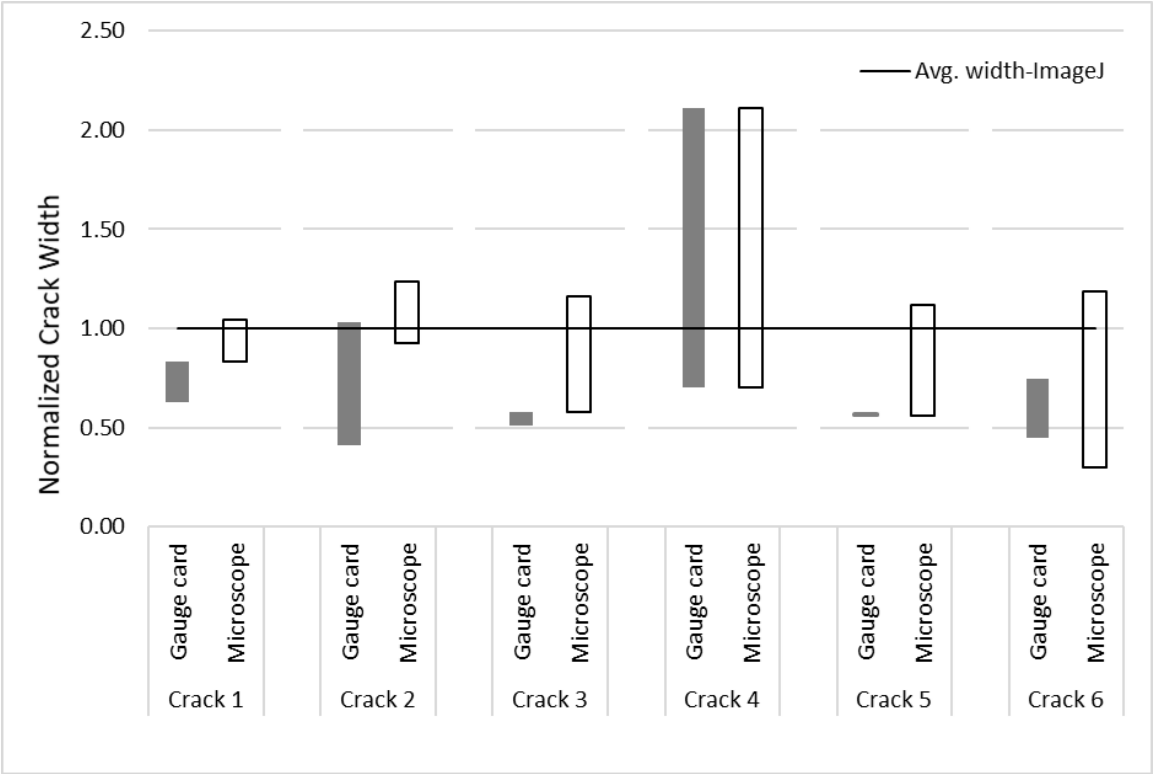

Figure 44. Comparison Index for the crack data from the study

Measurements using the microscope and ImageJ were in agreement as the average crack widths from ImageJ were within the range of widths measured using the microscope for each crack (Figure 44). In contrast, the measurements made using the crack gauge card did not align well with either the microscope or ImageJ results. The discrepancy, however, was only observed in cracks 1, 3, 5, and 6. These cracks had the smallest widths in the study (

). In the case of cracks 2 and 4, cracks had larger width and the range of measurements from the gauge card was better aligned with the other methods. These observations are attributed to a few different possible causes. For smaller crack sizes, the demarcations on the gauge card did not allow for precise measurements. Crack 5 was so small (between 0.01mm and 0.02mm) that the gauge crack could not provide any distinction between the minimum and maximum crack widths. As seen in Figure 37, the gauge card in the study had only eleven different options for determining the crack width. Another reason for the observed discrepancies is that there is some subjectivity in using a crack gauge card, especially for smaller cracks. The observer who conducted the study tended to undermeasure the crack width when using the gauge card relative to the other two methods. Gauge cards are quick and useful but are more subjective, leading to greater potential for error when measuring small cracks.

Some of the images were collected of cracks receiving direct light and other receiving indirect light. The filtering process in the software was able to adjust for both conditions, and no trends were observed in the comparisons based on the lighting. Average width measurements from image processing compared favorably with the range of microscope measurements for direct and indirect lighting conditions.

During the comparison field study, a few images were taken from textured surfaces and surfaces exposed to light at sharp angles. These images were taken due to the researchers' curiosity and were not part of the formal field study. However, these images warrant a brief discussion as they revealed an important practical consideration

for using image processing in field studies. Textured surfaces with direct light coming from a sharp angle can lead to issues in isolating the crack. Figure 45 shows one such surface and the associated binary image. Shadows within the crack and on the surface make it difficult to isolate the crack area, even by adjusting the filtering threshold. Based on these observations, caution is recommended when using image processing on textured surfaces, particularly when receiving direct light from a sharp angle. It is possible that artificial light could help; however, this was not considered in the study.

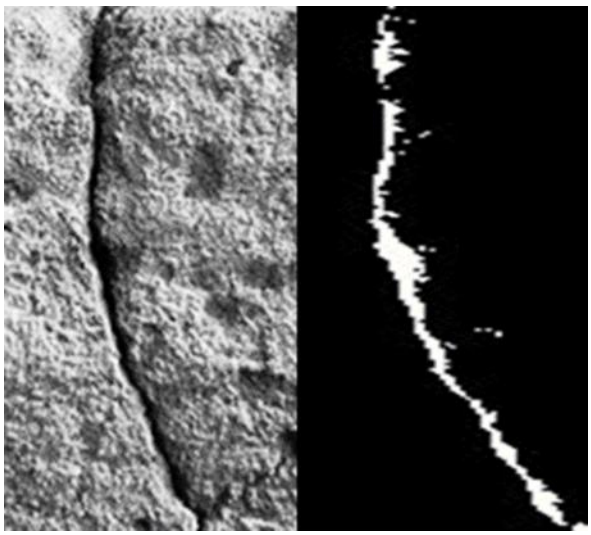

Figure 45. Increase in threshold due to improper lighting

Field Study Two: Image Processing to Evaluate Cracks in Precast-Pretensioned Girders

The effects of several variables on cracking were evaluated at the ends of eight girders, where each end was treated as a different specimen for purposes of the study. Variables included the location of the girder end on the stressing bed (interior or exterior) and type of coating on the confinement reinforcement (hot-dipped galvanized, smooth

epoxy-coated, or textured epoxy-coated). Results are summarized here to demonstrate the image processing measurement method.

Prior to collecting digital images, the ends were visually examined, and cracks were each labeled. Global photos encompassing the entire end of the girders were collected first (Figure 36), followed by local photos of the web and flange areas. Gauge cards were placed in the local photos to allow for subsequent scaling of the digital images (Figure 38).

A predetermined labeling system and careful attention to image review and filing were critical because different individuals handled onsite image collection and offsite image processing. The onsite researcher reviewed the local images immediately to confirm the clarity of the crack and scale. Unclear images were retaken. Additionally, stickers, and labels were placed to identify all photos to manage a large number of similar images.

Crack widths were determined from the images and used for comparison among the study variables. A normalized comparison index was calculated by dividing the crack size for a given specimen by the average crack size of all specimens. Hence, values of the comparison index, greater or lesser than one, indicate that the crack widths were larger or smaller than the average widths, respectively. Figure 46 and Figure 47 show how the crack data were evaluated in the girder field study. Crack data was collected from both the ends of 8 girders (16 end regions) with the number of cracks ranging from 18 to 26 for each girder. As shown in Figure 46, there were no observable differences in crack widths based on the location of the girder end on the stressing bed. The reinforcement

coating, however, did appear to influence cracking, where ends with textured epoxy-coated bars displayed a tendency to have larger than average cracks in the web and smaller than average widths in the flange. Additional details of the girder field study can be found in Ross et al. (2021) [1].

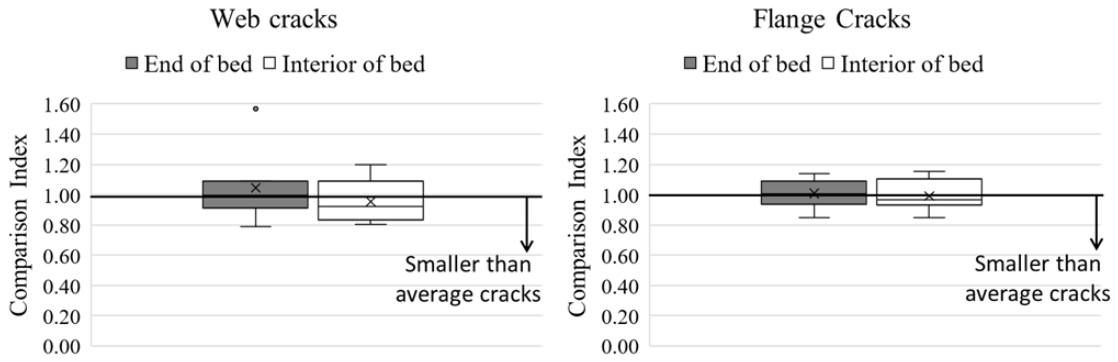

Figure 46. Comparison of web and flange cracks for different positions on stressing bed

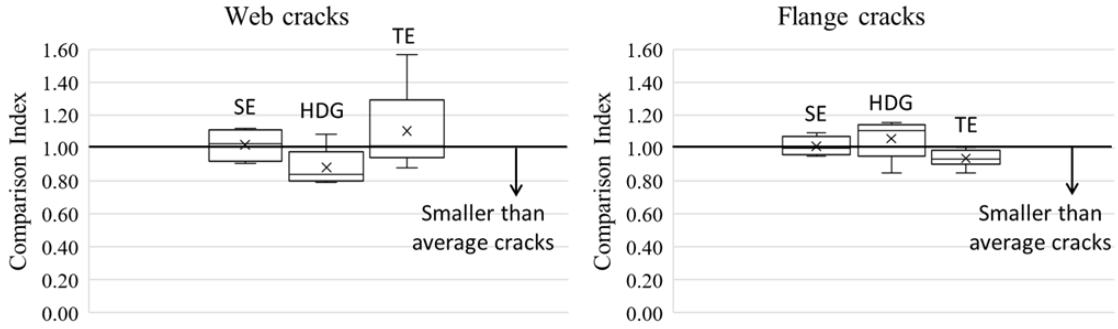

Figure 47. Comparison of web and flange cracks for variable reinforcement coatings: SE is smooth epoxy-coated, HDG is hot-dipped galvanized, and TE is textured epoxy-coated

Conclusion

Digital image processing was used to measure concrete cracks in two field studies. The first study compared image processing measurements with microscope and gauge card measurements. The second study evaluated the effects of different variables on end region cracks in precast concrete bridge girders. Conclusions are presented below according to the paper's three objectives:

Objective 1: Provide practical guidance for using digital image processing to measure concrete crack widths in field settings.

An overview of the steps and techniques was presented for measuring crack widths using digital image processing. Future users of this method should give particular attention to cropping, filtering, and cleaning images to isolate the crack before executing measurements. Lighting and surface texture should be considered where direct lighting from sharp angles on textured surfaces can lead to errors in image processing. Labeling, image quality review, and filing schemes should be established when the field study involves multiple specimens and many similar looking images. Images should include local and overall views of the structure to document both details and context.

Objective 2: Compare gauge cards, microscopes, and ImageJ as tools for measuring concrete crack widths in field settings.

Crack gauge cards are the quickest and easiest method to measure crack widths in the field studies but have notable limitations. They only provide a few possible crack

measurement sizes (eleven were provided on the card used in the study) making them less precise than the other measurement methods. Furthermore, the gauge card measurements were not in agreement with the other modes of measurement when cracks were small (i.e., approximately 0.1mm width). The microscope provided increased precision (0.02mm) relative to gauge card but at the expense of more effort and time. Image processing provided even greater precision (0.001mm) and resulted in average crack width measurements that were within the range of microscope measurements. Image processing also has the benefit of creating files to document conditions and facilitate future comparisons.

Objective 3: Demonstrate the use of image processing measurements in a field study of cracking in precast-pretensioned concrete girders.

Image processing was used to evaluate the effect of stressing bed location and confinement reinforcement coating on the width of end region cracks. No effect was observed for bed location. Girder ends at the outside and inside positions had similar crack sizes. Confinement reinforcement coatings had some effect, with ends reinforced with textured epoxy-coated bars tending to have larger web cracks and smaller flange cracks. The results demonstrate how image processing can be used to analyze and interpret data to address practical questions from field studies.

Data availability statement

Some or all data, models, or code generated or used during the study are available from the corresponding author by request. The available data are crack images, ImageJ data, and spreadsheets.

Acknowledgments

The authors wish to thank Wisconsin Department of Transportation (WisDOT), the United States Department Of Transportation (USDOT) for providing the funding for the research. County Materials corporation of Janesville, WI provided the access for the girder field study. Mr. Matt Mueller and Dr. Todd Davis conducted the site visits and data collection for the girder field study.

This research was associated with a project funded through WisDOT and the USDOT. Neither WisDOT nor the USDOT assume any liability for the contents or the use thereof nor does this presentation reflect official views, policies, standard specifications or regulations of either department.

IX. SUMMARY AND FINAL COMMENTS

This dissertation experimentally studied the impact of rebar coatings on rebar-concrete bond and on controlling concrete cracks. Bars in the experiments included uncoated (black), continuously galvanized, hot dipped galvanized, smooth epoxy and textured epoxy. Test types included bond tests, shrinkage test, and prism tension-tests. Tests from quasi-static flexural tests reported by Murphy [2] were used in an analytical study of bond mechanics.

Specific research questions were introduced and answered in the individual chapters. This chapter discusses an overall of all results. To make overall conclusion of which bar coating type provides the best structural performance, certain parameters from each test were considered. The parameters chosen for the overview were selected from each of the three experiments and provide a holistic measure of performance. The following are the concluding parameters from each type of test:

Bond – Slip at 80% of the specified yield stress level

Shrinkage – Average crack width measured from image analysis

Prism – Crack recovery ratio after unloading from the specified yield stress

One value for each parameter was taken for each specimen in each associated test type. Table 9 shows how many values were taken each type of bar. Except hot dipped galvanized (HDG) bar, all the other bar types were used in all the tests. HDG bars were not tested for their bond strength and hence the difference in the total number of values.

Table 9. Number of values of each bar type for each test type based on the chosen parameters for the overall analysis

Test\Bar type	B	CGR	SE	HDG	TE
Bond	4	4	4	-	4
Shrinkage	8	8	8	8	8
Prism	3	3	3	3	3
Total no. of values	15	15	15	11	15

The “best” and “worst” specimens were determined based on performance in each series and test type. Specimens that were not the best or worst were categorized as “in between”. For a given series, there was only one best and one worst, but multiple in between. The count of each level of performance of each bar type, for the selected parameters were tabulated. The overall performance of each bar type was plotted as a pie chart in terms of the percentage tom times that each bar type achieved the different levels of performance out of the total number of values. Performance pie charts are shown in Figure 48.

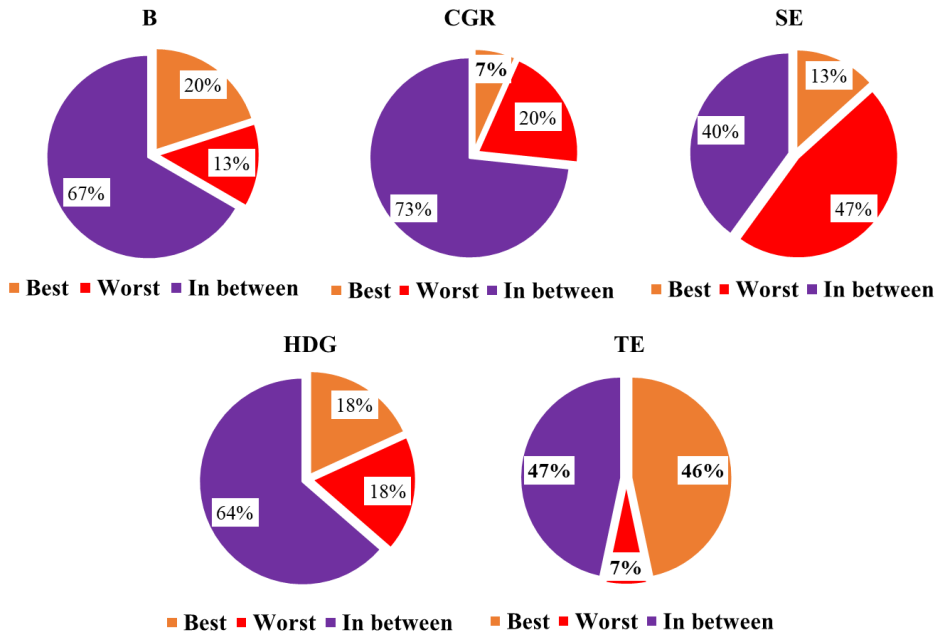

Figure 48. Performance pie charts of all the bar types. Percentages are the number of series in which a given bar type performed the best, worst, on in-between.

The overview analysis shows that the TE bars were the top performer in 47% of the test series. On the other hand, the smooth epoxy bars were the worst performer in 47% of the test series. The other bar coating types showed similar overall performance levels, with in-between being the most common level.

It is concluded the textured epoxy bars had good bond with concrete and were effective at resisting cracks. The observed results are likely generalizable for bars with similar types and levels of texture.

The tests in this dissertation were based on only one bar size, three different concrete/mortar mixes, specific levels of texturing/galvanizing, and were conducted at one institution. It is recommended that future research investigate the impact (if any) on

bond performance from bar size, level of texture, and concrete properties. Testing of columns, frames, and other structural elements may be considered. The primary purpose of many coatings is to mitigate corrosion; the interaction of corrosion performance, structural performance, and physical parameters should also be studied. Concrete cracking and rebar-concrete bond are random phenomena making them challenging to study. Additional tests of more specimens in more labs are necessary to achieve definitive results on the topic of crack control and bond performance of alternate coated reinforcements in concrete.

REFERENCES

1. Ross, B., Poursaee, A., Sreedhara, S., and Mueller, M., 2021. *Textured-epoxy Coated and Galvanized Reinforcement to Reduce Cracking in Concrete Bridge Decks and Components*: Wisconsin Department of Transportation.
2. Murphy, A., “Comparison of Flexural Cracking in Reinforced Concrete Beams with Different Bar Coatings” MS Thesis, Clemson University, 2021.
3. “Concrete Cracking.” https://scholar.google.com/scholar?q=%22concrete+cracking%22&hl=en&as_sdt=0,41&as_ylo=2021&as_yhi=2022&inst=1412731494629219040
4. Transportation, Research Board and National Academies of Sciences, Engineering, and Medicine. 2017. *Control of Concrete Cracking in Bridges*, edited by Henry G. Russell. Washington, DC: The National Academies Press. doi:10.17226/24689.
5. Williamson, G., Weyers, R.E., Brown, M.C., and Sprinkel, M.M., 2007. *Bridge Deck Service Life Prediction and Costs*, edited by Virginia Transportation Research Council, Virginia. Dept. of Transportation.
6. Aboalarab, L., "The Effect of Crack Opening Size and Repair Methods on Corrosion of Steel Reinforcement in Concrete" (2019). *Clemson University Dissertations*. 2397.
7. Foley, C.M., Wan, B., and Komp, J., 2010. *Concrete Cracking in New Bridge Decks and Overlays*: Wisconsin Highway Research Program.

8. Issa, M.A., 1999. "Investigation of Cracking in Concrete Bridge Decks at Early Ages." *Journal of Bridge Engineering* 4 (2): 116-124. doi:10.1061/(ASCE)1084-0702(1999)4:2(116).
9. Schmitt, T.R., and Darwin, D., "Cracking in Concrete Bridge Decks," SM Report No. 39, University of Kansas Center for Research, Inc., Lawrence, KS, April 1995, 164 pp.
10. Krauss, P.D., and Rogalla, E.A., 1996. *Transverse cracking in newly constructed bridge decks.* NCHRP Rep. No. 380. Washington, DC: Transportation Research Board, National Research Council.
11. Lindquist, W.D., Darwin, D., Browning, J.P., and Miller, G.G., "Effect of Cracking on Chloride Content in Concrete Bridge Decks," ACI Materials Journal, Vol. 103, No. 6, November-December 2006, pp. 467-473.
12. Darwin, D., Khajehdehi, R., Alhmood, A., Feng, M., Lafikes, J., Ibrahim, E.K., and O'Reilly, M., "Construction of Crack-Free Bridge Decks: Final Report, " SM Report No. 121, The University of Kansas Center for Research, Inc., Lawrence, KS, December 2016, 160 pp.
13. Hadidi, R., and Saadeghvaziri, M.A., 2005. "Transverse Cracking of Concrete Bridge Decks: State-of-the-Art." *Journal of Bridge Engineering* 10 (5): 503-510. doi:10.1061/(ASCE)1084-0702(2005)10:5(503).
14. Bektaş, B., Albughdadi, A., Freeseman, K., and Bazargani, B., 2020. *Protocols for Concrete Bridge Deck Protections and Treatments*: Wisconsin Department of Transportation.

15. Aboalarab, L., Ross, B.E., and Poursaee, A., 2020. "The Impact of Repair Method on the Chloride-Induced Corrosion of Steel Embedded in Cracked Concrete." *Advances in Civil Engineering Materials; Advances in Civil Engineering Materials* 9 (1): 143-151. doi:10.1520/ACEM20190200.
16. Corrosion Protection Performance of. 2008. *2008-47* Minnesota Department of Transportation. http://digital.library.wisc.edu/1793/54130
17. Frosch, R. J., Gutierrez, S., and Hoffman, J.S., *Control and Repair of Bridge Deck Cracking*. Publication FHWA/IN/JTRP-2010/04. Joint Transportation Research Program, Indiana Department of Transportation and Purdue University, West Lafayette, Indiana, 2010. https://doi.org/10.5703/1288284314267
18. Bales, E.R., Chitrapu, V., and Flint, M.M., 2018. *Bridge Service Life Design*, edited by Virginia Polytechnic Institute and State University. Charles E. Via, Jr. Dept. of Civil and Environmental Engineering. https://rosap.ntl.bts.gov/view/dot/37141.
19. Darwin, D., Browning, J., O'Reilly, M., and Xing, L., "Critical Chloride Corrosion Threshold for Galvanized Reinforcing Bars", SL Report 07-2, University of Kansas Center for Research, Inc., Lawrence, Kansas, December 2007, 36 pgs.
20. Lawler, J.S., Krauss, P.D., Kurth, J., and McDonald, D., 2011. "Condition Survey of Older West Virginia Bridge Decks Constructed with Epoxy-Coated Reinforcing Bars." *Transportation Research Record* 2220 (1): 57-65. doi:10.3141/2220-07. https://doi.org/10.3141/2220-07.

21. Oliva, M.G., and Okumus, P., 2011. *Finite Element Analysis of Deep Wide-Flanged Pre-Stressed Girders to Understand and Control End Cracking*: Wisconsin Department of Transportation.
22. Ross, B.E., Consolazio, G.R., and Hamilton, H.R., 2013. *End Region Detailing of Pretensioned Concrete Bridge Girders*, edited by University of Florida. Dept. of Civil and Coastal Engineering. https://rosap.ntl.bts.gov/view/dot/25872.
23. Ronanki, V.S., Burkhalter, D.I., Aaleti, S., Song, W., and Richardson, J.A., 2017. "Experimental and Analytical Investigation of End Zone Cracking in BT-78 Girders." *Engineering Structures* 151: 503-517. https://doi.org/10.1016/j.engstruct.2017.08.014.
24. National Academies of Sciences, Engineering, and Medicine. 2010. *Evaluation and Repair Procedures for Precast/Prestressed Concrete Girders with Longitudinal Cracking in the Web*. Washington, DC: The National Academies Press. https://doi.org/10.17226/14380
25. Willis, M.D., "POST-TENSIONING TO PREVENT END-REGION CRACKS IN PRETENSIONED CONCRETE GIRDERS" (2014). MS Thesis, *Clemson University*, https://tigerprints.clemson.edu/all_theses/1963
26. Hamilton, H.R., and Consolazio, G.R., 2020. *Hybrid Prestressed Concrete Bridge Girders using Ultra-High Performance Concrete*: Florida Department of Transportation.

27. Ross, B.E., Willis, M.D., Hamilton, H.R., and Consolazio, G.R., 2014. “Comparison of Details for Controlling End-Region Cracks in Precast, Pretensioned Concrete I-Girders.” PCI Journal 59 (2): 96–108.
28. "CRSI: History of Reinforcing Steel." https://crsi.org/index.cfm/basics/history-of-reinforcing-steel.
29. ASTM International. *A615/A615M-20 Standard Specification for Deformed and Plain Carbon-Steel Bars for Concrete Reinforcement*. West Conshohocken, PA; ASTM International, 2020. doi: https://doi.org/10.1520/A0615_A0615M-20
30. ASTM International. *A775/A775M-19 Standard Specification for Epoxy-Coated Steel Reinforcing Bars*. West Conshohocken, PA; ASTM International, 2019. doi: https://doi.org/10.1520/A0775_A0775M-19
31. Andrade, C., Barrett, T., Isgor, O.B., ElBatanouny, M., Hansson, C.M., Holland, R.B., Kahn, L.F., et al. 2016. "List of Contributors." In *Corrosion of Steel in Concrete Structures*, edited by Amir Poursaee, xi. Oxford: Woodhead Publishing. doi:https://doi.org/10.1016/B978-1-78242-381-2.01002-6.
32. Yeomans, S.R., Galvanized steel reinforcement, in Corrosion of Steel in Concrete Structures, Poursaee, A., Editor 2016, Woodhead Publishing. p. 294.
33. ASTM International. *A767/A767M-19 Standard Specification for Zinc-Coated (Galvanized) Steel Bars for Concrete Reinforcement*. West Conshohocken, PA; ASTM International, 2019. doi: https://doi.org/10.1520/A0767_A0767M-19
34. "Hdg Vs. Cgr." 100 Year Strong: Galvanized Rebar Alliance., accessed Jun 8, 2021, https://www.100yearstrong.com/hdg-vs-cgr.

35. Sharma, R., Goodwin, F.E., and Dallin, G.W., 2014. *Continuous Galvanized Rebar for Corrosion Control in RCC Structures*.

36. Choi, O.C., Hadje-Ghaffari, H., Darwin, D., and McCabe, S.L., "Bond of Epoxy-Coated Reinforcement: Bar Parameters," ACI Materials Journal Vol. 88, No. 26, March-April 1991, pp. 207-217.

37. Zhang, Z., Jung, D., and Andrawes, B., 2020. "Evaluation of Surface Roughness and Bond-Slip Behavior of New Textured-epoxy coated Reinforcing Bars." *Construction and Building Materials* 262: 120762. doi:https://doi.org/10.1016/j.conbuildmat.2020.120762.

38. Chang, J.J., Yeih, W., and Tsai, C.L., 2002. "Enhancement of Bond Strength for Epoxy-Coated Rebar using River Sand." *Construction and Building Materials* 16 (8): 465-472. doi:https://doi.org/10.1016/S0950-0618(02)00101-0.

39. Platt, Shawn and Kent A. Harries. 2018. "Geometry, Material Properties and Bond Performance of Prototype Titanium Reinforcing Bars." *Construction and Building Materials* 187: 1253-1266. doi:https://doi-org.libproxy.clemson.edu/10.1016/j.conbuildmat.2018.08.074.

40. Wight, J.K., and MacGregor, J.G., 2011. *Reinforced Concrete: Mechanics and Design.* Harlow: Pearson Education.

41. Darwin, D., and Graham, E.K., "Effect of Deformation Height and Spacing on Bond Strength of Reinforcing Bars," Project 56, SL Report 93-1, The Reinforced Concrete Research Council, January 1993, 71 pp.

42. Hofsoy, A., and Gukild, I., 1969. Bond studies on hot dip galvanized reinforcement in concrete. ACI J 66:174±84.
43. Andrade, C., and Holst, JD., 1995. Coating protection for reinforcement. Comite Euro-International Du Beton. State of the Art Report. London: Thomas Telford Publication; p. 51.
44. Daunt, J.P., 1998. An investigation into the bond strength of undeformed galvanized and black steel reinforcement in concrete as a function of curing time. Research thesis, Australian Defence Force Academy, School of Civil Engineering, University College, University of New South Wales, Canberra, Australia.
45. Kayali, O., and Yeomans, S.R., "Bond of Ribbed Galvanized Reinforcing Steel in Concrete." *Cement and Concrete Composites* 22.6 (2000): 459-67. Web.
46. Kim, K.E., and Andrawes, B., 2018. *Behavior of Epoxy-Coated Textured Reinforcing Bars*: University of Illinois, Urbana-Champaign.
47. Kim, K.E., and Andrawes, B., "Exploratory Study on Bond Behavior of Textured-epoxy coated Reinforcing Bars." *Journal of Materials in Civil Engineering* 31.8 (2019): 04019151. Web.
48. ACI Committee 209. (2005). *ACI 209.1R-05: Report on factors affecting shrinkage and creep of hardened concrete*. American Concrete Institute.
49. Gilbert, R. I. (1992). Shrinkage cracking in fully restrained concrete members. *ACI Structural Journal*, *89*(2), 141–149.

50. Andrawes, B., Perez Claros, E.A. and Zhang, Z., 2022. *Bond Characteristics and Experimental Behavior of Textured Epoxy-coated Rebars Used in Concrete Bridge Decks*. Illinois Center for Transportation/Illinois Department of Transportation.
51. ACI Committee 318. 2019. *Building code requirements for structural concrete (ACI 318-19): an ACI standard; Commentary on building code requirements for structural concrete (ACI 318R-19)*.
52. ASTM International. *A944-10(2015) Standard Test Method for Comparing Bond Strength of Steel Reinforcing Bars to Concrete Using Beam-End Specimens*. West Conshohocken, PA; ASTM International, 2015. doi: https://doi.org/10.1520/A0944-10R15
53. Mathey, R. G., and Clifton, J. R., 1976, "Bond of Coated Reinforcing Bars in Concrete," *Journal of the Structural Division,* ASCE, V. 102, Jan., pp. 215-228.
54. Johnston, D. W., and Zia, P., 1982, "Bond Characteristics of Epoxy-Coated Reinforcing Bars," *Report* No. FHWA/NC/82-002, Department of Civil Engineering, North Carolina State University, Raleigh, NC, Aug.
55. Treece, R. A., and Jirsa, J. O., 1989, "Bond Strength of Epoxy-Coated Reinforcing Bars," ACI Materials Journal, V. 86, No. 2, Mar.-Apr., pp. 167-174.
56. K. Raoufi, M. Pour-Ghaz, A Poursaee, and Weiss, J., *Restrained shrinkage cracking in concrete elements: role of substrate bond on crack development.* ASCE Journal of Materials in Civil Engineering, 2011. **June**: p. 895-902.

57. Nilson, A.H., Darwin, D., and Dolan, C.W., 2010. *Design of Concrete Structures.* McGraw Hill.

58. Den Uijl, J. A., & Bigaj, A. J. (1996). A bond model for ribbed bars based on concrete confinement. *HERON, 41 (3), 1996.*

59. Ruiz, M.F., Muttoni, A., & Gambarova, P.G., (2007). Analytical modeling of the pre- and postyield behavior of bond in reinforced concrete. *Journal of Structural Engineering, 133*(10), 1364-1372. doi:10.1061/(ASCE)0733-9445(2007)133:10(1364)

60. Abdel-Qader, I., Abudayyeh, O., and Kelly, M.E., 2003. "Analysis of edge-detection techniques for crack identification in bridges. Computing in Civil Engineering." **17**(4): p. 255-263.

61. Valença, J., Dias-da-Costa, D., and Júlio, E., 2012. "Characterisation of concrete cracking during laboratorial tests using image processing." Construction and Building Materials 28: 607-615.

62. Liu, Y., Cho, S., Spencer, B. F., and Fan, J., 2014. "Automated assessment of cracks on concrete surfaces using adaptive digital image processing." Smart Structures and Systems, *14*(4), 719-741. https://doi.org/10.12989/sss.2014.14.4.719

63. Liu, Y., Soojin, C., Spencer Jr, B.F., and Fan, J., 2016. "Concrete Crack Assessment using Digital Image Processing and 3D Scene Reconstruction." Journal of Computing in Civil Engineering 30 (1): 04014124.

Doi:10.1061/(ASCE)CP.1943-5487.0000446. https://doi.org/10.1061/(ASCE)CP.1943-5487.0000446.

64. Albareda-Valls, Albert, Alejandra Bustos Herrera, Joan L. Zamora Mestre, and Saeid S. Zaribaf, 2018. "Image Post-Processing Method for Quantification of Cracking in RC Precast Beams under Bending." *Buildings* 8, no. 11: 158. https://doi.org/10.3390/buildings8110158
65. Schneider, C. A., Rasband, W. S., and Eliceiri, K. W., 2012. "NIH Image to ImageJ: 25 years of image analysis." Nature Methods, *9*(7), 671–675. doi:10.1038/nmeth.2089
66. Pitas, I., 2000. "Digital Image Processing Algorithms and Applications." *(1st. ed.)*: John Wiley & Sons, Inc., USA.
67. Gonzalez, R.C., and Woods, R.E., 2004. "Digital Image Processing." *4th Edition* 2018: Pearson, Inc., USA.
68. Shih, F.Y., 2009. "Image processing and mathematical morphology: fundamentals and applications." CRC Press.
69. Koller, D., Daniilidis, K., and Nagel, H.H., 1993. "Model-based object tracking in monocular image sequences of road traffic scenes." International Journal of Computer Vision. **10**(3): p. 257-281.
70. Lin, D.F., Wang, H.Y., and Luo, H.L., 2004. "Assessment of fire-damaged mortar using digital image process. Materials in Civil Engineering." **16**(4): p. 383-386.

71. Aydilek, A.H., Oguz, S.H., and Edil, T.B., 2002. “Digital image analysis to determine pore opening size distribution of nonwoven geotextiles.” Computing in Civil Engineering. **16**(4): p. 280-290.
72. Chen, P., Chang, Y., Chang, L., and Doerschuk, P.C., 2002. “Application of multi-resolution pattern classification to steel bridge coating assessment.” Computing in Civil Engineering. **16**(4): p. 244-251.
73. Garboczi, E.J., 2002. “Three-dimensional mathematical analysis of particle shape using X-ray tomography and spherical harmonics: Application to aggregates used in concrete.” Cement and Concrete Composites. **32**(10): p. 1621-1638.
74. Lanzón, M., Cnudde, V., Kock, T., and Dewanckele, J., 2012. “X-ray microtomography (μ-CT) to evaluate microstructure of mortars containing low density additions.” Cement and Concrete Composites. **34**(9): p. 993-1000.
75. Razmjoo, A., and Poursaee, A., 2013. “Quantitative CT-scan imaging approach in determining the air voids and aggregate content in concrete.” I-manager's Journal on Civil Engineering. **4**(1): p. 12-19.
76. Razmjoo, A., and Poursaee, A., 2016. “Finite element modeling of chloride diffusion in concrete using image processing for characterizing real shape and distribution of different phases.” Advances in Civil Engineering Materials. **5**(1): p. 167-178.
77. Ruan, T., and Poursaee, A., 2019. “Fiber-distribution assessment in steel fiber-reinforced UHPC using conventional imaging, X-ray CT scan, and concrete

electrical conductivity.” ASCE Journal of Materials in Civil Engineering. **31**(8): p. 04019133.

78. Dizaji, M. S., Harris, D. K., Kassner, B., and Hill, J. C., 2021. “Full-field non-destructive image-based diagnostics of a structure using 3D digital image correlation and laser scanner techniques.” Journal of Civil Structural Health Monitoring, 11(5), 1415-1428.
79. Alipour, Mohamad, Washlesky, S.J., and Harris, D.K., 2019. "Field deployment and laboratory evaluation of 2D digital image correlation for deflection sensing in complex environments." Journal of Bridge Engineering 24, no. 4: 04019010.
80. Singh, T.R., Roy, S., Singh, O.I., Sinam, T., and Singh, K.M., 2011. “A New Local Adaptive Thresholding Technique in Binarization.” IJCSI International Journal of Computer Science Issues, Vol. 8, Issue 6, No 2.
81. Singh, O.I., Sinam, T., James, O., and Singh, T.R., 2012. “Local Contrast and Mean based Thresholding Technique in Image Binarization.” International Journal of Computer Applications (0975 – 8887) Volume 51– No.6.
82. Firdousi, R., and Parveen, S., 2014. "Local Thresholding Techniques in Image Binarization." International Journal of Engineering and Computer Science 3 (03).
83. Rahman, Md., Saifullah, I., and Ghosh, 2019. "Detection and Measurements of Cracks in Axially Loaded Tension RC Members by Image Processing Technique." American Journal of Civil Engineering and Architecture, 7: 115-120. Doi:10.12691/ajcea-7-2-5.

84. Barkavi, T., and Natarajan C., 2019. "Processing Digital Image for Measurement of Crack Dimensions in Concrete." Civil Engineering Infrastructures Journal 52 (1): 11-22. doi:10.22059/ceij.2019.246397.1444.

85. Gergely, P., Sozen, M.A., and Siess, C.P., 1963. “The Effect of Reinforcement on Anchorage Zone Cracks in Prestressed Concrete Members.” University of Illinois Structural Research Series No. 271, 170 pp.

86. Marshall, W., and Mattock, A., 1962. "Control of Horizontal Cracking in the Ends of Pretensioned Prestressed Concrete Girders." PCI Journal 7. Doi:10.15554/pcij.10011962.56.74.

87. Gamble, W., 2014. Discussion of "Comparison of Details for Controlling End-Region Cracks in Pre-tensioned Concrete I-Girders." *PCI Journal* 59: 134-136.

88. Hasenkamp, C.J., Badie, S.S., Tuan, C.Y., and Tadros, M.K., 2008. "Sources of End Zone Cracking of Pretensioned Concrete Girders." Concrete Bridge Conference, St. Louis, MO.

89. Murray, C.D., Cranor, B.N., Floyd, R.W., and Pei, J.S., 2019. "Experimental Testing of Older AASHTO Type-II Bridge Girders with Corrosion Damage at the Ends." PCI Journal 64, no. 1.

APPENDIX

Data sheets from the prism tests are presented below. Data sheets from the other test programs can be found in the report by Ross et al. [1].

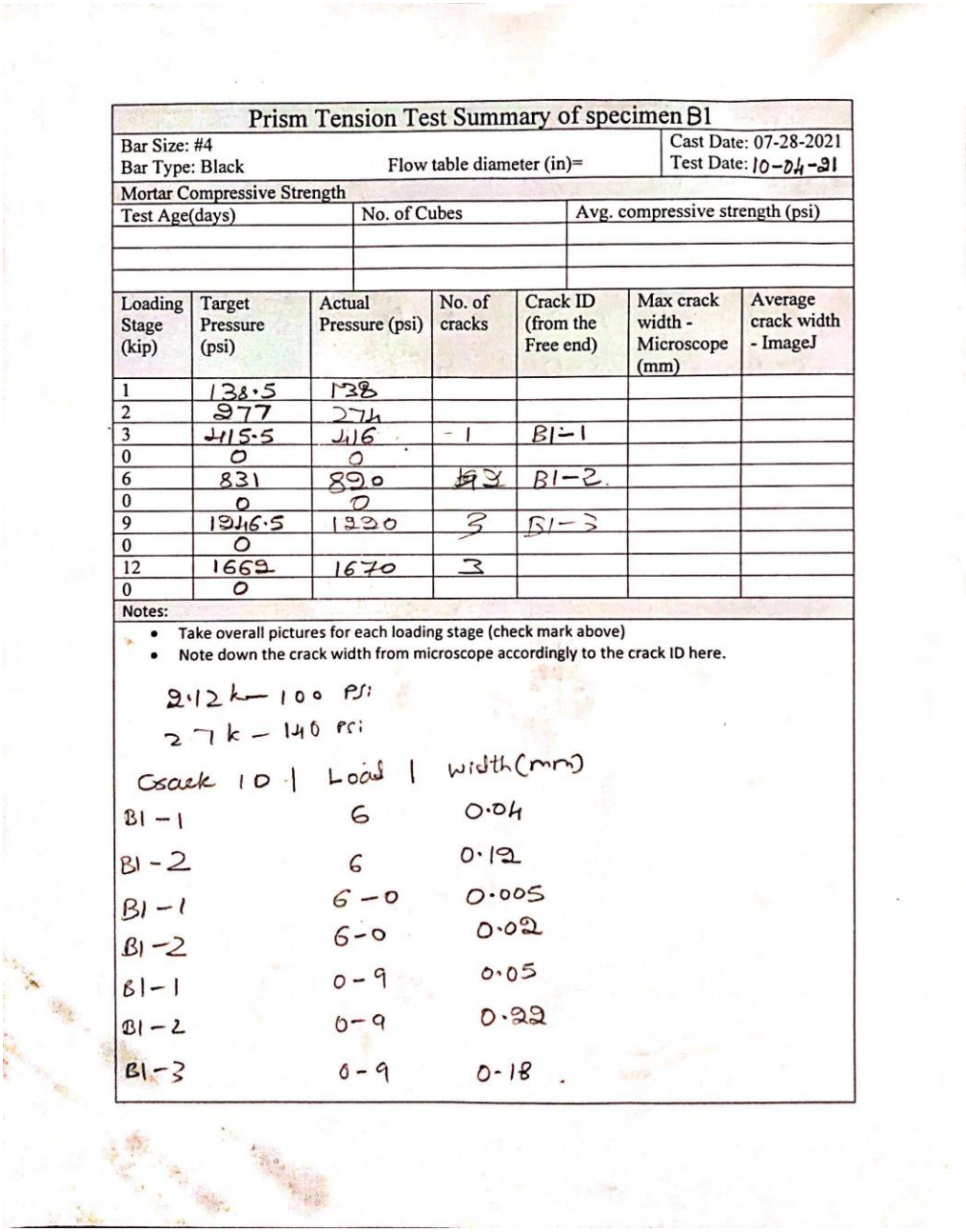

Prism Tension Test Summary of specimen B1

Bar Size: #4
Bar Type: Black
Flow table diameter (in)=
Cast Date: 07-28-2021
Test Date: 10-04-21

Mortar Compressive Strength

Test Age(days)	No. of Cubes	Avg. compressive strength (psi)

Loading Stage (kip)	Target Pressure (psi)	Actual Pressure (psi)	No. of cracks	Crack ID (from the Free end)	Max crack width - Microscope (mm)	Average crack width - ImageJ
1	138.5	138				
2	277	274				
3	415.5	416	1	B1-1		
0	0	0				
6	831	890	2	B1-2		
0	0	0				
9	1246.5	1220	3	B1-3		
0	0					
12	1662	1670	3			
0	0					

Notes:

- Take overall pictures for each loading stage (check mark above)
- Note down the crack width from microscope accordingly to the crack ID here.

2.12 k — 100 psi
27 k — 140 psi

Crack ID	Load	width (mm)
B1-1	6	0.04
B1-2	6	0.12
B1-1	6-0	0.005
B1-2	6-0	0.02
B1-1	0-9	0.05
B1-2	0-9	0.22
B1-3	0-9	0.18

Prism Test – B1.

Crack ID	Load.	Width
B1 – 1	9-0	0.02
B1 – 2	9–0	0.04
B1 – 3	9–0	0.05
B1–1	0–12	0.07
B1 – 2	0–12	0.3
B1–3	0 –12	0.3
B1 – 1	12 – 0	0.02
B1 – 2	12–0	0.06
B1 – 3	12 – 0	0.04

Prism Tension Test Summary of specimen B11

Bar Size: #4
Bar Type: Black
Flow table diameter (in)=
Cast Date: 07-28-2021
Test Date: 12-13-21

Mortar Compressive Strength

Test Age(days)	No. of Cubes	Avg. compressive strength (psi)

Loading Stage (kip)	Target Pressure (psi)	Actual Pressure (psi)	No. of cracks	Crack ID (from the Free end)	Max crack width - Microscope (mm)	Average crack width - ImageJ
1	138.5					
2	277					
3	415.5	423				
0	0					
6	831	840				
0	0					
9	1246.5	1253				
0	0					
12	1662	1680				
0	0					

Notes:

- ✓ Take overall pictures for each loading stage (check mark above)
- ✓ Note down the crack width from microscope accordingly to the crack ID here at 3,0,6,0,12,0 kip load levels.
- ✓✓ Crack photos at 3 kip
- ✓✓ Crack photos at 0 kip
- ✓✓ Crack photos at 6 kip — 1 crack @ 3k
- ✓ Crack photos at 0 kip
- ✓ Crack photos at 9 kip — 1 @ 3.6k
- ✓ Crack photos at 0 kip
- ✓ Crack photos at 12 kip
- ✓ Crack photos at 0 kip

Crack ID	Load (kip)	Crack width-Microscope (mm)
B2-1	3	0.08, 0.12, 0.14
B2-1	3-0	0.04, 0.04, 0.05
B2-1	6	0.18, 0.24, 0.3
B2-2	6	0.44, 0.44, 0.44
B2-1	6-0	0.06, 0.08, 0.08
B2-2	6-0	0.14, 0.14, 0.14
B2-1	9	0.24, 0.32, 0.4
B2-2	9	0.6, 0.6, 0.64
B2-1	9-0	0.06, 0.08, 0.1
B2-2	9-0	0.16, 0.16, 0.16
B2-1	12	0.22, 0.42, 0.5
B2-2	12	0.74, 0.78, 0.8
B2-1	12-0	0.07, 0.09, 0.1
B2-2	12-0	0.18, 0.18, 0.18

Prism Tension Test Summary of specimen II

Bar Size: #4
Bar Type: Black – 3
Flow table diameter (in)=
Cast Date: 07-28-2021
Test Date: 12-15-21

Mortar Compressive Strength

Test Age(days)	No. of Cubes	Avg. compressive strength (psi)

Loading Stage (kip)	Target Pressure (psi)	Actual Pressure (psi)	No. of cracks	Crack ID (from the Free end)	Max crack width - Microscope (mm)	Average crack width - ImageJ
1	138.5					
2	277					
3	415.5	420	1			
0	0					
6	831	845	2			
0	0					
9	1246.5	1260	2			
0	0					
12	1662	1675	2			
0	0					

Notes:

- ✓ Take overall pictures for each loading stage (check mark above)
- ✓ Note down the crack width from microscope accordingly to the crack ID here at 3,0,6,0,12,0 kip load levels.
- ✓ Crack photos at 3 kip
- ✓ Crack photos at 0 kip
- ✓ Crack photos at 6 kip I @ 3k
- ✓ Crack photos at 0 kip
- ✓ Crack photos at 9 kip II @ 3.9k
- ✓ Crack photos at 0 kip III @
- ✓ Crack photos at 12 kip
- ✓ Crack photos at 0 kip

Crack ID	Load (kip)	Crack width-Microscope (mm)
B3-1	3	0.2, 0.1
	3-0	0.12, 0.07
	6	0.28, 0.16
	6	0.28, 0.2
	6-0	0.12, 0.07
	6-0	0.12, 0.1
	9	(0.32), 0.36, 0.24
	9	(0.4), 0.4, 0.3
	9-0	(0.08), 0.13, 0.07
	9-0	(0.12), 0.12, 0.1
	12	(0.43), 0.45, (0.4), 0.30
	12	(0.5), 0.5, (0.46), 0.4
	12-0	(0.1), 0.12, (0.12), 0.07
	12-0	(0.12 0.12 (0.1), 0.1
		3/4" 1" 1 3/4" 2 3/4"

Prism Tension Test Summary of specimen 1-CGR

Bar Size: #4
Bar Type: ~~Black~~ CG1 Flow table diameter (in)=

Cast Date: 07-28-2021
Test Date: 11-09-21

Mortar Compressive Strength

Test Age(days)	No. of Cubes	Avg. compressive strength (psi)

Loading Stage (kip)	Target Pressure (psi)	Actual Pressure (psi)	No. of cracks	Crack ID (from the Free end)	Max crack width - Microscope (mm)	Average crack width - ImageJ
1	138.5	137				
2	277	280	1			
3	415.5	415	2			
0	0	0				
6	831	828	2			
0	0					
9	1246.5	1250	2			
0	0					
12	1662	1675				
0	0					

Attach LPs

Notes:

- ✓ Take overall pictures for each loading stage (check mark above)
- ✓ Note down the crack width from microscope accordingly to the crack ID here at 3,0,6,0,12,0 kip load levels.
- ✓ Crack photos at 3 kip
- ✓ Crack photos at 0 kip
- ✓ Crack photos at 6 kip
- ✓ Crack photos at 0 kip
- ✓ Crack photos at 9 kip
- ✓ Crack photos at 0 kip
- ✓ Crack photos at 12 kip
- ✓ Crack photos at 0 kip

First crack @ 1700 lb, seconds @

Crack ID	Load (kip)	Crack width-Microscope (mm)
CGR-1-3	3	0.18, 0.12
CGR-2-	3	0.16, 0.14
	0	
	0	
1	6	0.28, 0.99
2	6	0.24, 0.9
1	0	0.1, 0.08
2	0	0.08, 0.04
1	9	0.42, 0.36
2	9	0.3, 0.32
1	0	0.1, 0.08
2	0	0.08, 0.06
1	12	0.52, 0.46
2	12	0.4, 0.46
1	0	0.1, 0.08
2	0	0.1, 0.08.

Prism Tension Test Summary of specimen II CGR

Bar Size: #4
Bar Type: Black
Flow table diameter (in)=
Cast Date: 07-28-2021
Test Date: 12-13-21

Mortar Compressive Strength

Test Age(days)	No. of Cubes	Avg. compressive strength (psi)

Loading Stage (kip)	Target Pressure (psi)	Actual Pressure (psi)	No. of cracks	Crack ID (from the Free end)	Max crack width - Microscope (mm)	Average crack width - ImageJ
1	138.5					
2	277					
3	415.5	420				
0	0					
6	831	840				
0	0					
9	1246.5	1260				
0	0					
12	1662	1680				
0	0					

Notes:

- ✓ Take overall pictures for each loading stage (check mark above)
- ✓ Note down the crack width from microscope accordingly to the crack ID here at 3,0,6,0,12,0 kip load levels.
- ✓ Crack photos at 3 kip
- ✓ Crack photos at 0 kip
- ✓ Crack photos at 6 kip
- ✓ Crack photos at 0 kip
- ✓ Crack photos at 9 kip
- ✓ Crack photos at 0 kip
- ✓ Crack photos at 12 kip
- ✓ Crack photos at 0 kip

I @ 2.4k
II @ 4.3k
III during 0-9

Crack ID	Load (kip)	Crack width-Microscope (mm)
CGR2-1	3	0.16, 0.06
CGR2-1	3-0	0.1, 0.04
CGR2-1	6	0.26, 0.1
CGR2-2	6	0.25, 0.24
CGR2-1	6-0	0.14, 0.04
CGR2-2	6-0	0.1, 0.08
CGR2-1	9	0.28, 0.16
CGR2-2	9	0.14, 0.12
CGR2-3	9	0.32, 0.28
CGR2-1	9-0	0.12, 0.05
CGR2-2	9-0	0.08, 0.07
CGR2-3	9-0	0.08, 0.08
CGR2-1	12	0.36, 0.24
CGR2-2	12	0.17, 0.16
CGR2-3	12	0.44, 0.42
CGR2-1	12-0	0.12, 0.05
CGR2-2	12-0	0.06, 0.06
CGR2-3	12-0	0.1, 0.1

Prism Tension Test Summary of specimen III

Bar Size: #4
Bar Type: ~~Black~~ CGR-3 Flow table diameter (in)=

Cast Date: 07-28-2021
Test Date: 12-15-21

Mortar Compressive Strength

Test Age(days)	No. of Cubes	Avg. compressive strength (psi)

Loading Stage (kip)	Target Pressure (psi)	Actual Pressure (psi)	No. of cracks	Crack ID (from the Free end)	Max crack width - Microscope (mm)	Average crack width - ImageJ
1	138.5					
2	277					
3	415.5	425	1			
0	0					
6	831	850	3+1			
0	0					
9	1246.5	1250	4			
0	0					
12	1662	1680	4			
0	0					

Notes:

- ✓ Take overall pictures for each loading stage (check mark above)
- ✓ Note down the crack width from microscope accordingly to the crack ID here at 3,0,6,0,12,0 kip load levels.
- ✓ Crack photos at 3 kip
- ✓ Crack photos at 0 kip
- ✓ Crack photos at 6 kip I 3k
- ✓ Crack photos at 0 kip 3.45k
- ✓ Crack photos at 9 kip
- ✓ Crack photos at 0 kip II, III, IV,
- ✓ Crack photos at 12 kip
- ✓ Crack photos at 0 kip

Crack ID	Load (kip)	Crack width-Microscope (mm)
CGR3-1	3	0.24↓ 0.24↓
	3-0	0.14, 0.12
	6	0.2, 0.2
	6	0.26, 0.16
	6	0.24, 0.2↓
	6	0.3, 0.3↑
	6-0	0.12, 0.12
	6-0	0.1, 0.1
	6-0	0.1, 0.08
	6-0	0.12, 0.1
	9	0.24, 0.26
	9	0.28, 0.14
	9	0.36, 0.34
	9	0.28, 0.28
	9-0	0.11, 0.12
	9-0	0.1, 0.09
	9-0	0.1, 0.1
	9-0	0.08, 0.1
	12	0.34, 0.34
long crack	12	0.4(2), 0.38 (0.3)
	12	0.38, 0.38
	12	0.30, 0.30

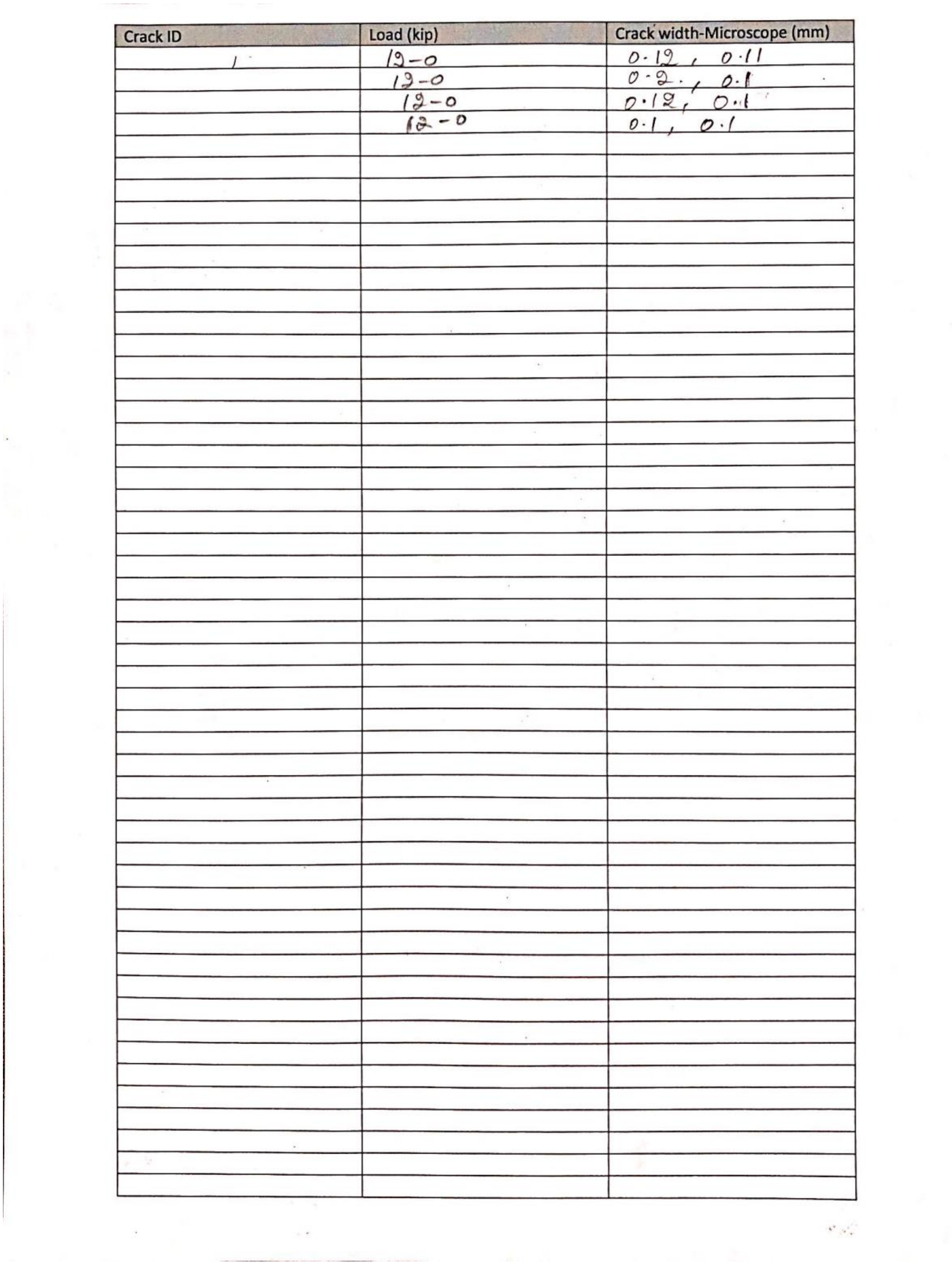

Crack ID	Load (kip)	Crack width-Microscope (mm)
1	12-0	0.12, 0.11
	12-0	0.2, 0.1
	12-0	0.12, 0.1
	12-0	0.1, 0.1

Prism Tension Test Summary of specimen 1—HDG

Bar Size: #4
Bar Type: ~~Black~~ HDG
Flow table diameter (in)=
Cast Date: 07-28-2021
Test Date: 11/10/21

Mortar Compressive Strength

Test Age(days)	No. of Cubes	Avg. compressive strength (psi)

Loading Stage (kip)	Target Pressure (psi)	Actual Pressure (psi)	No. of cracks	Crack ID (from the Free end)	Max crack width - Microscope (mm)	Average crack width - ImageJ
1	138.5	139				
2	277	277				
3	415.5	420				
0	0		2nd			
6	831	5500# 830	4			
0	0					
9	1246.5	1253	4			
0	0					
12	1662	1663	4			
0	0					

Notes:

- ✓ Take overall pictures for each loading stage (check mark above)
- ✓ Note down the crack width from microscope accordingly to the crack ID here at 3,0,6,0,12,0 kip load levels.
- ✓ Crack photos at 3 kip
- ✓ Crack photos at 0 kip
- ✓ Crack photos at 6 kip
- ✓ Crack photos at 0 kip
- ✓ Crack photos at 9 kip
- ✓ Crack photos at 0 kip
- ✓ Crack photos at 12 kip
- ✓ Crack photos at 0 kip

First crack @ 1800 #
Second @ 2400 #
third @ 4500 #
Fourth @ 5500 #

Crack ID	Load (kip)	Crack width-Microscope (mm)
HDG-1	3	0.06, 0.035
HDG-2	3	0.24, 0.26
1	0	0.04, 0.013
2	0	0.14, 0.16
3	6	0.16, 0.32
4	6	0.28, 0.30
1	6	0.14, 0.16
2	6	0.16, 0.12
3	5.5- 0	0.08, 0.14
4	5.5- 0	0.1, 0.12
1	5.5- 0	0.06, 0.06
2	5.5- 0	0.04, 0.04
3	9	0.22, 0.4
4		0.86, 0.4
1		0.22, 0.22
2	9	0.18, 0.24
3	0	0.045, 0.09
4	0	0.05, 0.08
1	0	0.045, 0.04
2	0	0.04, 0.05
3		
4		

Crack ID	Load (kip)	Crack width-Microscope (mm)
HDG-1	12	0.24, 0.44
2		0.32, 0.44
		0.28, 0.26
HDG-4		0.225, 0.3
5	12	0.19, 0.32
1	0	0.05, 0.1
2		0.06, 0.08
3		0.04, 0.04
4		0.025, 0.06
5		0.025, 0.04

Prism Tension Test Summary of specimen II HDG

Bar Size: #4
Bar Type: Black HDG-2 Flow table diameter (in)=

Cast Date: 07-28-2021
Test Date: 12-15-21

Mortar Compressive Strength

Test Age(days)	No. of Cubes	Avg. compressive strength (psi)

Loading Stage (kip)	Target Pressure (psi)	Actual Pressure (psi)	No. of cracks	Crack ID (from the Free end)	Max crack width - Microscope (mm)	Average crack width - ImageJ
1	138.5					
2	277					
3	415.5					
0	0					
6	831					
0	0					
9	1246.5					
0	0					
12	1662					
0	0					

Notes:

- ✓ Take overall pictures for each loading stage (check mark above)
- ✓ Note down the crack width from microscope accordingly to the crack ID here at 3,0,6,0,12,0 kip load levels.
- ✓ Crack photos at 3 kip
- ✓ Crack photos at 0 kip
- ✓ Crack photos at 6 kip I crack @ 1.5k
- ✓ Crack photos at 0 kip
- ✓ Crack photos at 9 kip II Crack@4k
- ✓ Crack photos at 0 kip
- ✓ Crack photos at 12 kip III Crack @ 4.2k
- ✓ Crack photos at 0 kip

observed longitudinal crack in 0-12 started from crack 3

Crack ID	Load (kip)	Crack width-Microscope (mm)
HDG2-1	3	0.28, 0.16
HDG2-2	3-0	0.18, 0.08
2-1	6	0.32, 0.24
2-2	6	0.32, 0.32
2-3	6	0.30, 0.14
	6-0	0.2, 0.12
	6-0	0.14, 0.14
	6-0	0.14, 0.04
	9	0.34, 0.29
	9	0.42, 0.48
	9	0.42, 0.2
	9-0	0.2, 0.11
	9-0	0.22, 0.16
	9-0	0.14, 0.04
	12	0.44, 0.40
	12	0.5, 0.5
	12	0.49, 0.24
	12-0	0.18, 0.12
	12-0	0.22, 0.16
	12-0	0.14, 0.04

Prism Tension Test Summary of specimen 11

Bar Size: #4
Bar Type: ~~Black~~ HDG-3 Flow table diameter (in)=

Cast Date: 07-28-2021
Test Date: 12-16-21

Mortar Compressive Strength

Test Age(days)	No. of Cubes	Avg. compressive strength (psi)

Loading Stage (kip)	Target Pressure (psi)	Actual Pressure (psi)	No. of cracks	Crack ID (from the Free end)	Max crack width - Microscope (mm)	Average crack width - ImageJ
1	138.5					
2	277					
3	415.5	430	1			
0	0					
6	831	845	1+1			
0	0					
9	1246.5	1260	2+1			
0	0					
12	1662	1680	3			
0	0					

Notes:

- ✓ Take overall pictures for each loading stage (check mark above)
- ✓ Note down the crack width from microscope accordingly to the crack ID here at 3,0,6,0,12,0 kip load levels.
- ✓ Crack photos at 3 kip
- ✓ Crack photos at 0 kip
- ✓ Crack photos at 6 kip I @ 2.5k
- ✓ Crack photos at 0 kip
- ✓ Crack photos at 9 kip III 8.1k
- ✓ Crack photos at 0 kip
- ✓ Crack photos at 12 kip
- ✓ Crack photos at 0 kip

Crack ID	Load (kip)	Crack width-Microscope (mm)
HDG 3-1	3	0.17, 0.04
	3-0	0.1, 0.03
	6	0.28, 0.13
	6	0.18, 0.08
	6-0	0.12, 0.03
	6-0	0.06, 0.04
	9	0.34, 0.16
	9	0.21, 0.06
	9	0.26, 0.22
	9-0	0.12, 0.05
	9-0	0.08, 0.02
	9-0	0.06, 0.06
	12	0.24, 0.28
	12	0.28, 0.12
	12	0.20, 0.18
	12-0	0.12, 0.05
	12-0	0.08, 0.02
	12-0	0.05, 0.06

Prism Tension Test Summary of specimen 1 – SE

Bar Size: #4
Bar Type: Black
Flow table diameter (in)=
Cast Date: 07-28-2021
Test Date: 11/9/21

Mortar Compressive Strength

Test Age(days)	No. of Cubes	Avg. compressive strength (psi)

Loading Stage (kip)	Target Pressure (psi)	Actual Pressure (psi)	No. of cracks	Crack ID (from the Free end)	Max crack width - Microscope (mm)	Average crack width - ImageJ
1	138.5	150	0			
2	277	278	0			
3	415.5	416	1			
0	0					
6	831	836	1			
0	0					
9	1246.5	1248	3			
0	0					
12	1662	1670	3			
0	0					

Notes:

- ✓ Take overall pictures for each loading stage (check mark above)
- ✓ Note down the crack width from microscope accordingly to the crack ID here at 3,0,6,0,12,0 kip load levels.
- ✓ Crack photos at 3 kip
- ✓ Crack photos at 0 kip
- ✓ Crack photos at 6 kip
- ✓ Crack photos at 0 kip
- ✓ Crack photos at 9 kip
- ✓ Crack photos at 0 kip
- ✓ Crack photos at 12 kip
- ✓ Crack photos at 0 kip

First crack at 2500 to 3000#. Second & third around 8500#.

Crack ID	Load (kip)	Crack width-Microscope (mm)
1	3	0.2, 0.18
1	0	0.1, 0.08
1	6	0.34, 0.34
1	0	0.11, 0.1
1	9	0.38, 0.38
2	9	0.12, 0.22
3	9	0.3, 0.24
1	0	0.15, 0.14
2	0	0.04, 0.07
3	0	0.08, 0.07
1	12	0.44, 0.44
2	12	0.2, 0.3
3	12	0.42, 0.38
1	0	0.15, 0.13
2	0	0.04, 0.04
3	0	0.08, 0.07

Prism Tension Test Summary of specimen 1

Bar Size: #4
Bar Type: ~~Black~~ SE-2 Flow table diameter (in)=
Cast Date: 07-28-2021
Test Date: 12-15-21

Mortar Compressive Strength

Test Age(days)	No. of Cubes	Avg. compressive strength (psi)

Loading Stage (kip)	Target Pressure (psi)	Actual Pressure (psi)	No. of cracks	Crack ID (from the Free end)	Max crack width - Microscope (mm)	Average crack width - ImageJ
1	138.5					
2	277					
3	415.5					
0	0					
6	831	850				
0	0					
9	1246.5					
0	0					
12	1662					
0	0					

Notes:

- ✓ Take overall pictures for each loading stage (check mark above)
- ✓ Note down the crack width from microscope accordingly to the crack ID here at 3,0,6,0,12,0 kip load levels.
- ✓ Crack photos at 3 kip
- ✓ Crack photos at 0 kip
- ✓ Crack photos at 6 kip I crack @ 2k
- ✓ Crack photos at 0 kip
- ✓ Crack photos at 9 kip II crack @ 5.5k
- ✓ Crack photos at 0 kip III crack @
- ✓ Crack photos at 12 kip
- ✓ Crack photos at 0 kip

Crack ID	Load (kip)	Crack width-Microscope (mm)
SE2-1	3	0.04, 0.15
SE2-1	3-0	0.02, 0.07
	6	0.3, 0.42
	6	0.18, 0.22
	6-0	0.26, 0.28
	6-0	0.1, 0.08
	9	0.38, 0.5
	9	0.3, 0.36
	9-0	0.28, 0.28
	9-0	0.14, 0.1
	12	0.48, 0.7
	12	0.48, 0.56
	12-0	0.4, 0.44
	12-0	0.16, 0.14

Prism Tension Test Summary of specimen 1

Bar Size: #4
Bar Type: ~~Black~~ SE-3 Flow table diameter (in)=

Cast Date: 07-28-2021
Test Date: 12-16-21

Mortar Compressive Strength

Test Age(days)	No. of Cubes	Avg. compressive strength (psi)

Loading Stage (kip)	Target Pressure (psi)	Actual Pressure (psi)	No. of cracks	Crack ID (from the Free end)	Max crack width - Microscope (mm)	Average crack width - ImageJ
1	138.5					
2	277					
3	415.5	421	0			
0	0					
6	831	850	1			
0	0					
9	1246.5	1250	1			
0	0					
12	1662	1680	1+1			
0	0					

Notes:

- ✓ Take overall pictures for each loading stage (check mark above)
- ✓ Note down the crack width from microscope accordingly to the crack ID here at 3,0,6,0,12,0 kip load levels.
- ✓ Crack photos at 3 kip
- ✓ Crack photos at 0 kip
- ✓ Crack photos at 6 kip I @ 3.8k
- ✓ Crack photos at 0 kip
- ✓ Crack photos at 9 kip II @ 10.5k
- ✓ Crack photos at 0 kip
- ✓ Crack photos at 12 kip III @
- ✓ Crack photos at 0 kip

Crack ID	Load (kip)	Crack width-Microscope (mm)
SE3-1	3	—
SE3-1	3-0	—
SE3-1	6	0.24, 0.56
SE3-1	6-0	0.1, 0.48
SE3-1	9	0.34, 0.7
	9-0	0.1, 0.48
	12	0.44, 0.76
	12	0.22, 0.22
	12-0	0.13, 0.5
	12-0	0.05, 0.05

Prism Tension Test Summary of specimen 1 – TE

Bar Size: #4
Bar Type: ~~Black~~ TE
Flow table diameter (in)=
Cast Date: 07-28-2021
Test Date: 11/11/21

Mortar Compressive Strength

Test Age(days)	No. of Cubes	Avg. compressive strength (psi)

Loading Stage (kip)	Target Pressure (psi)	Actual Pressure (psi)	No. of cracks	Crack ID (from the Free end)	Max crack width - Microscope (mm)	Average crack width - ImageJ
1	138.5					
2	277					
3	415.5	416	3			
0	0					
6	831	830	5			
0	0					
9	1246.5	1258	5			
0	0					
12	1662					
0	0					

Notes:

- ✓ Take overall pictures for each loading stage (check mark above)
- ✓ Note down the crack width from microscope accordingly to the crack ID here at 3,0,6,0,12,0 kip load levels.
- ✓ Crack photos at 3 kip
- ✓ Crack photos at 0 kip
- ✓ Crack photos at 6 kip
- ✓ Crack photos at 0 kip
- ✓ Crack photos at 9 kip
- ✓ Crack photos at 0 kip
- ✓ Crack photos at 12 kip
- ✓ Crack photos at 0 kip

I @ 900#
II @ 1150#
III @ 2958#
IV @ 3700#
V @ 5560

Crack ID	Load (kip)	Crack width-Microscope (mm)
1	3	0.28, 0.98
2	3	0.24, 0.24
3	3	0.155, 0.19
1	0	0.19, 0.19
2	0	0.16, 0.15
3	0	0.095, 0.08
1	6	0.33, 0.2
2	6	0.05, 0.06
3	6	0.26, 0.24
4	6	0.24, 0.24
5	6	0.14, 0.14
1	0	0.1, 0.09
2	0	0.06, 0.06
3	0	0.1, 0.1
4	0	0.1, 0.08
5	0	0.04, 0.04
1	9	0.34, 0.24
2	9	0.12, 0.14
3	9	0.15, 0.15
4	9	0.38, 0.35
5	9	0.26, 0.25

Crack ID	Load (kip)	Crack width-Microscope (mm)
1	0	0.22, 0.08
2	0	0.04, 0.045
3	0	0.07, 0.07
4	0	0.11, 0.09
5	0	0.05, 0.05
1	12	0.36, 0.34
2	12	0.18, 0.2
3	12	0.16, 0.12
4	12	0.34, 0.32
5	12	0.34, 0.34
1	0	0.23, 0.08, 0.08
2	0	0.05, 0.06
3	0	0.06, 0.06
4	0	0.08, 0.06
5	0	0.06, 0.05

Prism Tension Test Summary of specimen 1

Bar Size: #4
Bar Type: ~~Black~~ TE-2 Flow table diameter (in)=

Cast Date: 07-28-2021
Test Date: 12-15-21

Mortar Compressive Strength

Test Age(days)	No. of Cubes	Avg. compressive strength (psi)

Loading Stage (kip)	Target Pressure (psi)	Actual Pressure (psi)	No. of cracks	Crack ID (from the Free end)	Max crack width - Microscope (mm)	Average crack width - ImageJ
1	138.5					
2	277					
3	415.5		(0-3.6k)			
0	0					
6	831					
0	0					
9	1246.5					
0	0					
12	1662					
0	0					

Notes:

- ✓ Take overall pictures for each loading stage (check mark above)
- ✓ Note down the crack width from microscope accordingly to the crack ID here at 3,0,6,0,12,0 kip load levels.
- ✓ Crack photos at 3 kip
- ✓ Crack photos at 0 kip
- ✓ Crack photos at 6 kip
- ✓ Crack photos at 0 kip
- ✓ Crack photos at 9 kip
- ✓ Crack photos at 0 kip
- ✓ Crack photos at 12 kip
- ✓ Crack photos at 0 kip

975 lb
1k

Crack ID	Load (kip)	Crack width-Microscope (mm)
TE2-1	3	0.06, 0.3
TE2-1	3-0	0.05, 0.26
	6	0.22, 0.3
	6	0.14, 0.12
	6-0	0.1, 0.22
	6-0	0.1, 0.06
	9	0.30, 0.32,
	9	0.16, 0.18
	9-0	0.1, 0.2
	9-0	0.08, 0.06
	12	0.38, 0.36
	12	0.2, 0.3
	12-0	0.12, 0.2
	12-0	0.08, 0.06
	12-0	

Prism Tension Test Summary of specimen 1

Bar Size: #4
Bar Type: ~~Black~~ TE-3 Flow table diameter (in)=

Cast Date: 07-28-2021
Test Date: 12-15-21

Mortar Compressive Strength

Test Age(days)	No. of Cubes	Avg. compressive strength (psi)

Loading Stage (kip)	Target Pressure (psi)	Actual Pressure (psi)	No. of cracks	Crack ID (from the Free end)	Max crack width - Microscope (mm)	Average crack width - ImageJ
1	138.5					
2	277					
3	415.5	425	1			
0	0					
6	831	860	2			
0	0					
9	1246.5	1250	2			
0	0					
12	1662					
0	0					

Notes:

- ✓ Take overall pictures for each loading stage (check mark above)
- ✓ Note down the crack width from microscope accordingly to the crack ID here at 3,0,6,0,12,0 kip load levels.
- ✓ Crack photos at 3 kip
- ✓ Crack photos at 0 kip
- ✓ Crack photos at 6 kip I @ 2.2k
- ✓ Crack photos at 0 kip II @ 3.5k
- ✓ Crack photos at 9 kip
- ✓ Crack photos at 0 kip III @
- ✓ Crack photos at 12 kip
- ✓ Crack photos at 0 kip

Crack ID	Load (kip)	Crack width-Microscope (mm)
TE3-1	3	0.2, 0.2
	3-0	0.1, 0.1
	6	0.26, 0.3
	6	0.2, 0.18
	6-0	0.1, 0.1
	6-0	0.1, 0.06
	9	0.36, 0.4
	9	0.28, 0.22
	9-0	0.1, 0.1
	9-0	0.08, 0.07
	12	0.44, 0.48
	12	0.4, 0.34
	12-0	0.11, 0.11
	12-0	0.11, 0.1